Numerical study of droplet coalescence and droplet shedding on surfaces with various wettabilities

Mehran Mohammadi Farhangi

A Thesis

in

the Department

of

Mechanical and Industrial Engineering

Presented in Partial Fulfillment of the Requirements
for the Degree of Master of Applied Science (Mechanical Engineering) at
Concordia University
Montreal, Quebec, Canada

2012

CONCORDIA UNIVERSITY
School of Graduate Studies

This is to certify that the thesis prepared

By: Mehran Mohammadi Farhangi

Entitled: "Numerical study of droplet coalescence and droplet shedding on surfaces with various wettabilities" and submitted in partial fulfillment of the requirements for the degree of

Master of Applied Science (Mechanical Engineering)

complies with the regulations of the University and meets the accepted standards with respect to originality and quality.

Signed by the final examining committee:

_____ Dr. B. Gordon _____ Chair

_____ Dr. M. Paraschiviou _____ Examiner

_____ Dr. S. Li, BCEE_____ Examiner

_____ Dr. A. Dolatabadi _____ Supervisor

Approved by _____
Chair of Department or Graduate Program Director

_____
Dean of Faculty

Date _____

Abstract

NUMERICAL STUDY OF DROPLET COALESCENCE AND DROPLET SHEDDING ON SURFACES WITH VARIOUS WETTABILITIES

MEHRAN MOHAMMADI FARHANGI

In this thesis, the dynamic behavior of droplets including the coalescence of a falling droplet with a sessile droplet on solid, and shedding of a sessile droplet exposed to shearing airflow are studied numerically. A two-phase volume of fluid (VOF) method is used to determine the droplet flow, shape evaluation, and contact line movement. The flows studied are treated as being laminar and computed in the framework of the finite-volume numerical method. To validate the model, the results of simulations for maximum spreading diameter of coalescing droplets are compared with experiment. The effect of different parameters such as droplet diameter, the impact velocity, the distance between the impacting droplets, and surface wettability on maximum spreading length, contact time and restitution coefficient are studied and compared to the experimental results. It has been found that the contact time is independent of the impact velocity in a wide range of velocities; however, it largely depends on droplet diameter. The evolution of surface shape during the coalescence of two droplets on various surfaces is computed numerically and compared with experimental results. The spread length of two coalesced droplets along their original center is also predicted by the model and compared well with the experimental results. Finally, the fundamental parameters determining the incipient motion for a droplet exposed to shearing airflow (runback) are investigated. It was found that wetting parameters such as contact angle and contact angle hysteresis are very influential in determining the minimum required air velocity for drop shedding.

Acknowledgements

I would like to express my best gratitude toward my academic advisor, Dr. Dolatabadi for his constant support and guidance during my master's program. This work is partially supported by Natural Sciences and Engineering Research Council of Canada (NSERC), Bombardier Aerospace, Pratt and Whitney Canada and CRIAQ.

Table of Contents

List of figures

List of tables

Nomenclature

D_0	Drop diameter [m]
D_y	Spreading length [m]
D_s	Sessile spread diameter [m]
D_c	Contact diameter [m]
d	Distance vector [m]
R_0	Drop radius [m]
R_{eff}	Effective Radius of truncated sphere
U_0	Impact velocity [m/s]
$Urel$	Relative velocity [m/s]
U_∞	Upstream velocity [m/s]
U_{drop}	Droplet velocity [m/s]
U_r	Radial velocity [m/s]
U_{cl}	Contact line velocity [m/s]
F_d	Drag force [N]
F_{adh}	Drag force [N]
A_p	Projection area [m^2]
V	Volume [m^3]
k	Curvature of interface [1/m]
k_c	Adjustable coefficient
g	gravitational acceleration [m/s^2]
θ_e	Equilibrium contact angle
θ_s	Static contact angle
θ_d	Dynamic contact angle
θ_R	Receding contact angle
θ_A	Advancing Contact angle
α	Sliding angle
p	Pressure [N/m^2]
t	Time [s]
S_f	Cell-face surface-normal vector [m^2]

G_s	Stable surface free energy [N.m]
SE	Surface energy [N.m]
f	Volume fraction (dimensionless)
We	Weber number (dimensionless)
We_{sl}	Surface Weber number (dimensionless)
Re	Reynolds number (dimensionless)
Re_{eff}	Effective Reynolds number (dimensionless)
Ca	Capillary number (dimensionless)
C_d	Drag coefficient (dimensionless)
τ	Dimensionless time
τ_c	Dimensionless contact time
ε	Restitution coefficient
f_d	Geometric weighting factor
L	Center to center distance [m]
	Greek letters
ρ	Density [kg/m^3]
ρ_l	Liquid density [kg/m^3]
ρ_g	Gas density [kg/m^3]
μ	Dynamic viscosity [kg/(m s)]
μ_l	Liquid dynamic viscosity [kg/(m s)]
μ_g	Gas dynamic viscosity [kg/(m s)]
Φ	General tensorial variable
γ	Surface tension [kg/s2]
λ	Offset ratio
τ	Dimensionless time
ψ	Spreading length (dimensionless)
ψ_{max}	Maximum spreading length (dimensionless)
	Subscript and superscript
l	Liquid

g	Gas
cl	Contact line

1 Introduction

Collision of a droplet with solid and liquid are a key element of wide variety of phenomena which can lead to serious issues on many natural and engineering systems, such as inhibited data transfer for telecommunications systems, corrosion of structures exposed to the elements, absorption of water into porous building material, decreased aerodynamic performance due to ice accumulation on aircrafts and damage to buildings and similar structures caused by increased loading from buildup of snow and ice.

Droplet accumulation is not always a desirable phenomenon, since it is required for spray cooling of hot surfaces such as turbine blades, semiconductor chips, and electronic devices to enable high heat fluxes in these surfaces where even small temperature gradients across the chip or turbine blade may cause component failure. Investigation of droplet coalescence have also importance in a number of industrial processes such as solid-inkjet printing [8-11], rapid prototyping[12], micro-fabrication[13], paint spraying and electronic packaging[14]. These applications require accurate placement of polymer solution or metal droplets on substrates to build images, ink-jet printed liquid line[15] or electrically conductive lines. Neighboring droplets must overlap and coalesce during the impact process to avoid breaks in the pattern being fabricated. There are many other applications in which collision of droplets on solid surfaces is an essential step such as dispersal of seed and microorganisms and pesticide spraying in agriculture, internal combustion engines with direct fuel injection [16], where the fuel is sprayed into engine cylinders in a form of small droplets. The complexity of droplet accumulation requires understanding of surface wettability; droplet impact dynamics; droplet coalescing mechanics; among many others.

The wettability of a liquid droplet is defined as the contact angle between a droplet in thermal equilibrium on a horizontal substrate. The wetting or static contact angle (θs), as illustrated in

Figure 1, is the angle at which the liquid-vapor interface meets the solid-liquid interface. The contact angle is a thermodynamic variable that depends on the interfacial tensions of the surfaces[17]. Young presented an equation, which relates liquid-solid (γ_{ls}), solid-gas (γ_{sg}) and liquid-gas (γ_{lg}) interfacial energies to predict the contact angle of a liquid droplet on a solid surface, as shown in equation (1).

$$\gamma_{sg} = \gamma_{ls} + \gamma_{lg} \cos\theta_s \qquad (1)^{17}$$

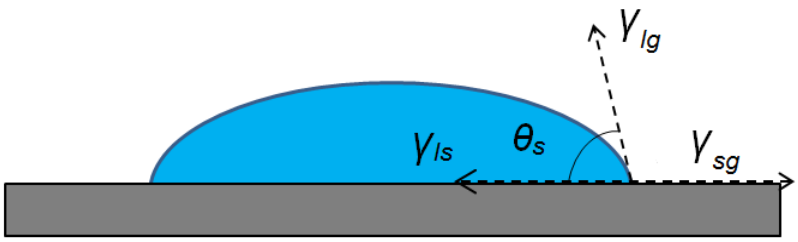

Figure 1: Contact angle of a liquid droplet wetted to a solid surface

Depending on the type of substrate and liquid the droplet may take a variety of shapes as shown in figure 2. The surface is defined wetting (hydrophilic) when contact angle is smaller than 90º , non-wetting (hydrophobic) when the contact angle is greater than 90º and highly non-wetting (superhydrophobic) when the contact angles of a water droplet exceeds 150° and the contact angle hysteresis is less than 10° . The contact angle hysteresis is defined as the difference between the advancing (θ_A) and receding (θ_R) contact angles. Figure 3 illustrates the receding and advancing contact angles of liquid droplet sliding down on tilted plate.

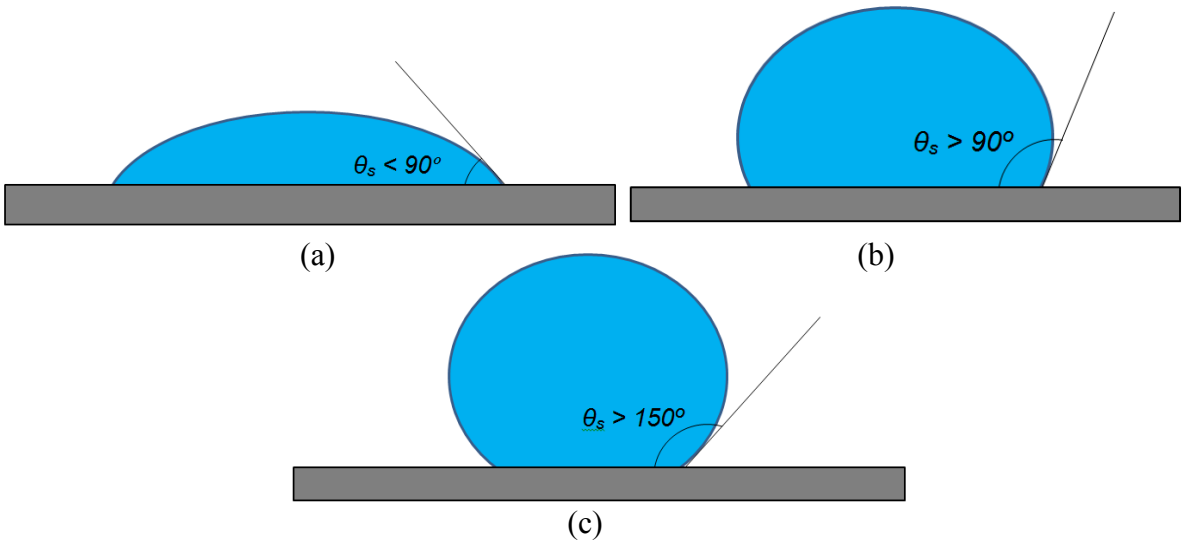

Figure 2: Distinction between (a) hydrophilic, (b) hydrophobic and (c) superhydrophobic surfaces.

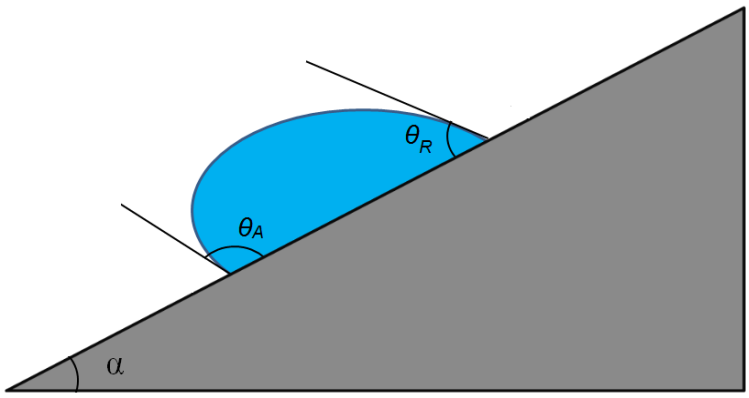

Figure 3. Schematics of advancing and receding contact angles

Liquid droplet behaviour on surfaces can be characterized by two surface properties: mobility and repellency[18-20]. The mobility of a surface is expressed as the advancing contact angle, θ_A, and receding contact angle, θ_R , whereas the static contact angle, θ_s, are associated with repellency. As it is shown in figure 2, the static contact angle which express the liquid repellency, can be used to distinguish between hydrophilic and hydrophobic surfaces. The distinction between hydrophobic and superhydrophobic is attributed to the mobility of the droplet. In a typical wetting experiment using the tilted plate method, a drop is placed onto a surface, which is then inclined until the drop begins to slide (Fig.3). The sliding angle (α) is a measure of the mobility of a drop on the surface. A smaller sliding angle indicates a more mobile droplet. The surfaces with small hysteresis (θ_A - θ_R <10°) are considered more mobile.

As previously mentioned, the main characteristic of a superhydrophobic surface is its low surface energy, which presents itself by a high static contact angle and low hysteresis. In these surfaces, the droplet rests on numerous nanostructures as results of which pocket air entrapped beneath the droplet. Cassie, Baxter and Wenzel studied the principles of superhydrophobic surfaces[1,2].Cassie and Wenzel states refer to whether the droplet is embedded in the roughness of the surface or resting on top of the various peaks on the surface as shown in Fig.4. The Cassie regime is considered to cause superhydrophobic surfaces, which have both high mobility and high water repellency, whereas in Wenzel state droplet suffers from a lack of mobility[18.]

.

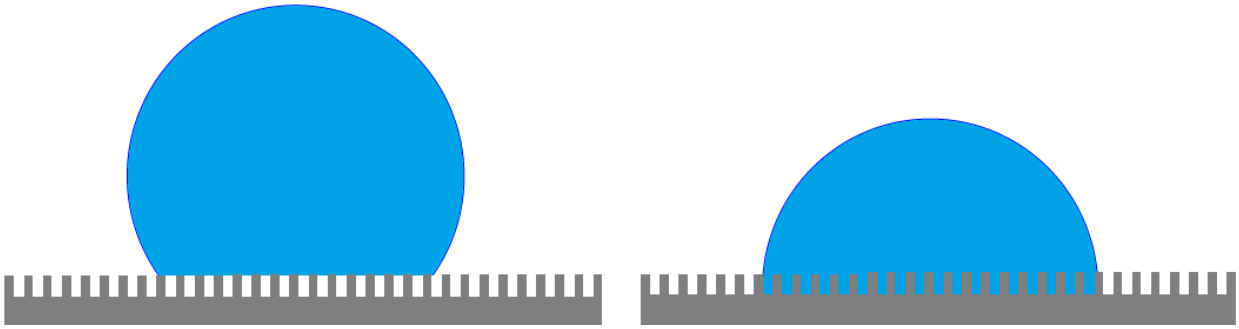

a) Cassie Model b) Wenzel Model

Figure 4: A droplet on a rough surface in (a) Cassie state[1] and (b) Wenzel state[2].

Research has progressed in this field rapidly over recent years, in two major domains, developing superhydrophobic surfaces and characterizing the behavior of droplets on these surfaces[4,21,22]. To take advantage of these phenomena, numerous artificial superhydrophobic surfaces have been manufactured using rough polymer textures[3,23,24], polymer nanocomposites,[25] metal-oxide nanostructures,[26,27] and carbon nanotubes[28,29]. Inspiration for fabrication of superhydrophobic surfaces comes from nature in the form of the lotus leaf and the legs of water spiders, to name a few. As an example, a lotus leaf's surface consists of a dual scale micro/nanostructures and a sheet of hydrophobic resin as shown in Fig. 5[3].

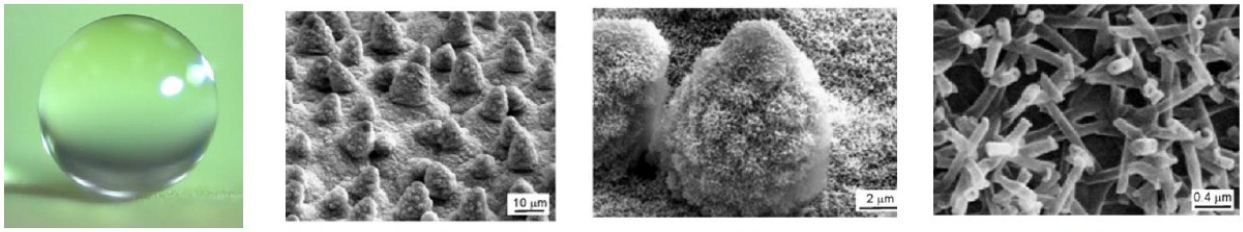

(a) (b) (c) (d)

Figure 5: Hierarchical superhydrophobic structures in nature, (a) A droplet resting on a lotus leaf and (b-d) increasing magnification of surface topography [3].

Because of their practical and industrial relevance a great amount of work has been invested in studying drop impacts experimentally[30-35], theoretically[36-38] and numerically[39-41] in the past decades. It is very tedious to give a detailed overview of the entire available research and achievements made. Therefore only selected investigations are presented that are considered to be the most interesting and relevant in the light of the present work. Mainly computational and few theoretical and experimental studies are reviewed. More comprehensive general reviews are provided by Rein [42]and Yarin[43].

The spreading of a single droplet on a solid surface was studied to understand a fundamental mechanism of the complex problem by Chandra and Avedisian[31]. It has been found experimentally that when a droplet impacts on a solid surface, it may spread, rebound, partially rebound, and splash due to different wetting properties of the surface and various impact velocities. Pasandideh-Fard et al. [36]also investigated numerically and experimentally the effect of contact angle and surface tension on the droplet impact onto a dry stainless steel surface. They used Volume of Fluid (VOF) method, in which the presence of air was neglected, to capture the free-surface flow. In their experiments a single bubble is observed in the droplet at the impact point that could not be resolved in their simulation. Following their work, Mehdi-Nejad et al. [44] simulated the droplet impact of different liquids on a dry solid surface using a modified Volume of Fluid (VOF) method. Their simulations captured air bubbles entrapped at the solid surface beneath the impacting droplet.

Rioboo et al. [4] summarized six different regimes of droplet behaviour for various impact conditions, liquid properties and surface properties. Figure 6 presents the time sequences of the flow regimes after droplet impingement named as deposition, prompt splash, corona splash, receding break-up, partial rebound and complete rebound, respectively. In the deposition regime,

the droplet after impingement stays spread over the surface. The spreading ratio is proportional to the square root of time in the initial phase, while the dependence on the liquid properties becomes noticeable only at later state of the spreading. By increasing the droplet impact velocity, water droplet splashes on surface and some small-sized droplets detaches from the edge of the spreading lamella as results of increases surface roughness. As in the previous case, the lamella stays spread over the substrate. Corona splash regime can happen either by decreasing the surface tension, in which the lamella may detach from the wall and crown is formed, or droplet impact onto a liquid layer. The resulting flow pattern is the corona splash and the formation of the crown is caused by surface roughness. As impinging velocity is increased, after the lamella has reached the maximum spreading ratio, droplet begins to recede driven mainly by the surface tension and the surface wettability. By increasing the contact angle or decreasing the wettability of surface the receding break-up flow regime develops. Further decrease in wettability of surface causes the droplet partially bounces off the substrate, or completely detaches from the surface as in the complete rebound.

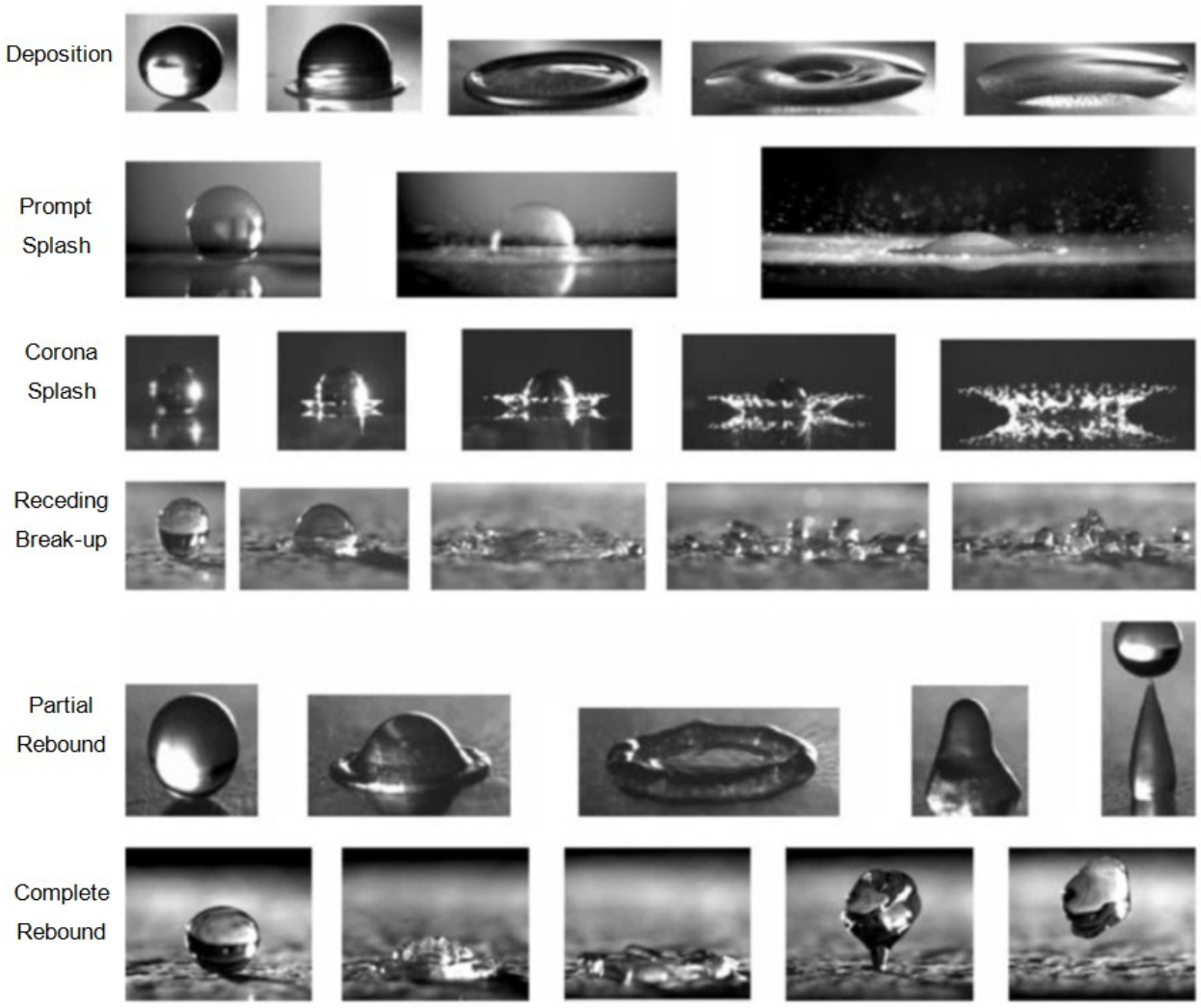

Figure 6: The various regimes of droplet impact[4].

As it is shown in Fig. 6, when a droplet impacts a superhydrophobic surface it may partially rebound or completely rebound from the surface. These self-cleaning aspect of superhydrophobic surfaces has been examined extensively[3]. The restitution coefficient and the contact time are two parameters studied experimentally in the works of Richard et al.[33],Reyssat et al., [45]and Chen et al.[46] Richard et al. [33]found that the contact time of an impinging droplet does not depend on impact velocity. Reyssat et al. [45] examined the deformation and energy losses during the

bouncing of the impinging droplet which results in a lower restitution coefficient. Chen et al. [46]showed that the microstructure of the surface influences the behavior of the restitution coefficient and the contact time with respect to velocity.

1.1 Motivation

As mentioned above, coalescence of droplets on a solid surface is a phenomenon with applications in a number of industrial applications which can benefit from a deeper understanding of droplet dynamics, such as spray coating, ink-jet printing, erosion, water and ice accumulation among many others[9,47-50]. The formation and accretion of ice on aircraft wings, tail, and propulsion system components can lead to serious safety problems such as increase of aerodynamic drag, loss of lift force and loss of the handling quality of the aircraft when in its high-lift configuration. A popular solution is the application of coatings or surface treatments to drastically decrease the wettability of the surfaces for mitigating the formation of ice in the first place by promoting the shedding of the liquid drops. Figure 7 shows the remarkable performance in both icing and de-icing modes of superhydrophobic coatings (SHC)[5]. The coated part of the surface actively repels water and consequently has no ice accumulation, in contrast to the uncoated part of the surface that is not water repellant has accumulated a substantial amount of ice.

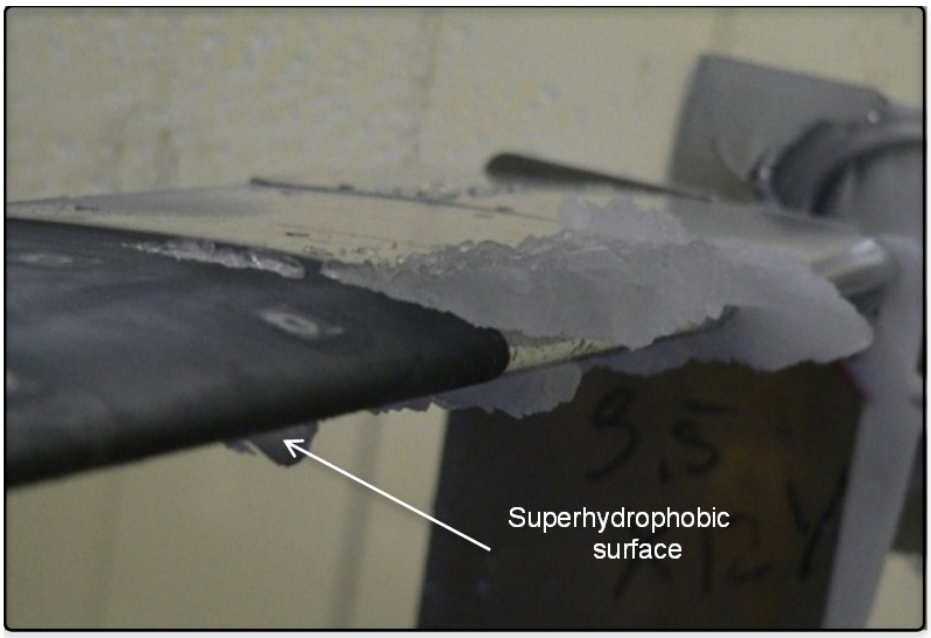

Figure 7: Performance of a superhydrophobic surface compared to hydrophilic surface under icing conditions[5].

Lack of full understanding of droplet coalescence mechanics and droplet shedding motivated us to numerically investigate these phenomena. The purpose of this project is to add emphasis on drop dynamics on the surface and to take advantage of superhydrophobic coatings not only to reduce the adhesion of the ice, but also to mitigate the formation of ice in the first place by promoting the shedding of the liquid drops from the surfaces. Numerical simulations provide a detailed database comprising the dynamics of the drop surface with respect to its position and form, since the temporal behavior of entire velocity and pressure fields are beyond the reach of the existing experimental methods. This study is mainly dedicated towards understanding the onset of droplet accumulation and onset of droplet shedding on surfaces of various wettabilities.

1.2 Droplet Coalescence

After the impingement of a first droplet, the effect of the second droplet would help provide insight into the accumulation of water droplets, as it may affect to film formation or rivulet formation. The coalescence of droplets on a solid surface is a phenomenon can easily be encountered by aircrafts flying into clouds or building during rainstorms, for which an understanding would greatly benefit the aerospace industry. Recently, a great interest has arisen for industrial application of superhydrophobic surfaces (SHS), for their capability to reduced droplet accumulation on surfaces[51,52]. The application of these surfaces would be beneficial in many fields, such as aviation, automobile and infrastructure sectors. Knowing the effectiveness of hydrophobic as opposed to superhydrophobic surfaces would be beneficial when making engineering and design decisions for systems exposed to water accumulation. To date, the work done related to understanding the mechanisms of reduced water accumulation have focused on the impingement of a single droplet,[4,22,34] the condensation of droplets in a humid environment, and the adhesive strength between the droplet and the surface.[53]In addition to the water droplets accumulation, the dynamics of droplet coalescence on a substrate is important for solid-inkjet printing[8-11], rapid prototyping[12], micro-fabrication[13] and electronic packaging[14].

The study of the impact and coalescence of droplets is important to the ink-jet industry since it can strongly influence the quality of printing. These applications require accurate placement of polymer solution or metal droplets on substrates to build images, liquid line or electrically conductive lines. Neighboring droplets must overlap and coalesce during the impact process to avoid breaks in the pattern being fabricated.

Soltman and Subramanian [9] investigated the effects of droplet spacing and temperature on the inkjet printed line morphologies. They developed a simple model to predict the transition

from a uniform line to a scalloped line using the ratio of droplet spacing to landed drop radius. Stringer and Derby[47] presented that the width of printed line depends on the droplet size and the surface energy between droplet and substrate. They found the line width on various substrates with different contact angles and droplet offset using a simple geometric model.

Duineveld[15], Gao and Sonin[54] experimentally investigated the formation and stability of liquid and molten lines printed on solid surface by sweeping a droplet generator. They observed that the line thickness becomes non-uniform due to the formation of a series of liquid bulges connected by ridges of liquid. The final shape of molten wax droplets after they had been deposited along a straight line was investigated experimentally by Li et al.[49] They observed that when two overlapping droplets are deposited on a surface, surface tension might pull the second toward the first, a process recognized as ‘‘drawback’’. The spacing of subsequent droplets is changed by this motion and can cause breaks in the line. Sellier et al.[55]and Kapur et al.[56] experimentally and numerically studied the dynamics of coalescence of two sessile liquid drops. In these experiments, a first stationary drop is placed on a substrate and a second drop is generated to grow next to it by feeding fluid through a small hole in the substrate until the edge of the second droplet contacts the first and coalescence occurs. Their experimental data show the rapid neck growth which is driven by surface tension and is opposed by inertial or viscous forces, occurred at the point of connection between the two drops from above and/or from the side.

The evolution of surface-shape during the coalescence of two mercury drops on a glass surface, driven only by surface tension was examined by Menchaca-Rocha et al.[57]Thoroddsen et al.[58] investigated the coalescence of a pendant droplet with a sessile droplet deposited on a

surface. Their experimental set-up focuses on the initial coalescence motions, by growing a pendent and a sessile drop on vertically aligned metal tubes, until they come into contact.

Theoretical investigation of droplet coalescence has been mostly focused on two-dimensional configurations. The coalescence shapes for two-dimensional inviscid wedges using the self-similar solutions for capillary-driven flows have been calculated by Keller et al.[59] Oguz and Prosperetti[60] studied the coalescence of rain drops. They observed that a finite velocity of approach will increase the probability of bubble entrapment during coalescence. Ristenpart et al.[61] studied the coalescence dynamics of two droplets on a highly wettable substrate and measured the width of a growing meniscus bridge between the two droplets. Andrieu et al. [62] studied experimentally and theoretically the description of the coalescence kinetics of two water drops on a plane solid surface. Their results showed that the drops grow by condensation and eventually touch each other and coalesce.

Duchemin et al. [63] theoretically investigated the surface tension-driven coalescence of two inviscid drops. The impact of multiple drops onto a dry substrate and their interactions were studied experimentally and theoretically by Roisman et al.[32] They showed that their analytical model is valid for inertia-dominated impact, when the Reynolds and Weber numbers are large and when droplets are weakly interacting. Eggers et al. [64] studied the coalescence of two drops surrounded by a viscous fluid for low Reynolds number, $Re \ll 1$. They defined Reynolds number of the surface tension driven flow using the radius of the bridge along the initial contact line as the characteristic length. The early time evolution of the shape of the liquid bridge was shown, and the bridge radius follows a scaling law.

Previous experimental studies have been reported, which visualized the internal flow using dual-field and tomographic PIV systems, to provide precise understanding of the internal

flow in colliding and coalescing drops.[65, 66] In addition to the flow study of inside the droplets, PIV has been used to study the flow of the medium for droplet collisions in liquids. The medium in which a droplet resides is an important parameter in the coalescence process. Both Jungyong Kim et al. [67]and Ortiz-Duenas et al. [68] investigated the effect of the medium during droplet coalescence by studying the coalescence process of a water-gylcerin mixture in a silicon-oil mixture by using dual field PIV and tomographic PIV, respectively. Based on the flow filed measurements inside droplets, both works discuss the presence of a film separating the droplet and present the specific instant and location along the interface where the film is depleted and the droplets begin to merge.

The effect of contact angle hysteresis in the superhydrophobic range on droplet coalescence was studied by Nilsson et al.[69] In order to induce coalescence, the droplet was displaced with a gentle airflow. The degree of mixing and free surface evolution was studied for various impact conditions; they showed that a small hysteresis greatly improves mixing. Recently, coalescence of two droplets on a solid superhydrophobic surface was experimentally and numerically investigated by Farhangi et al.[51] It was shown that due to the impingement of the second droplet, the resulting merged droplet can be completely removed from a superhydrophobic surface. It was also found that increasing the impact velocity, droplet size, and offset ratio reduces restitution coefficient due to the increased deformation of the merged droplets.

In spite of all these studies, rarely a single study has examined a wide range of wettabilities for droplet coalescence. The intention of the present work is to study numerically the coalescence dynamics of water droplets for surfaces of various wettabilities. In addition to

substrates with various wettabilities, the impact velocity, spacing between droplets and droplet size were varied.

1.3 Droplet Shedding

The shedding of sessile drops by airflow is another interesting phenomenon, which frequently occurs in nature and has many industrial applications. After the impact of water droplets on a substrate, droplets can be removed (or shed) from surface, if the adhesive force between the droplet and the surface can be overcome by the external drag forces on the drop. The minimum wind speed to shed a droplet is referred to as the point of incipient motion[7]. The flow of water droplets and rivulets after the point of incipient motion towards the tail of the airfoil is called runback flow which its formation depends based on numerous factors such as droplet size, surface roughness, air speed, and boundary layer thickness[70]. The adhesion of a drop on a surface is controlled by wetting characteristics which includes surface tension, contact angle, and contact line size and shape. The drag forces on the drop are based upon air velocity and drop area and shape (both functions of contact angle), so both adhesion and drag forces are dependent on wetting characteristics.

Liquid droplets adhering to, moving along or detaching from solid surfaces by shear flow are encountered in several natural and engineering systems such as cleaning[71], prevention of ice formation on aircraft and power line components, improving the efficiency of wind turbines[70,72] ,and water management in fuel cells. Considering the many applications, several research activities have been aimed at predicting the critical conditions for drop runback by using a variety of approaches. White and Schmucker[70] performed an advanced aerodynamic analysis for external flow over a system of water on smooth aluminum. They found the critical runback

volume for three different turbulent air velocities. They did not consider wetting and adhesion in great depth in their analysis. Bico et al. [73] investigated the incipient motion of water and glycerin droplets for a range of 3 to 500 μL, on RainX-coated surface. They found that for droplets above 100 μL, the critical air velocity and runback behavior were independent of volume, since the drop deformed into a sausage shape.

The phenomena of deformation, displacement and detachment of droplet by airflow on surfaces are also of interest in enhanced oil recovery [74,75].The ease of oil droplet deformation and displacement determines the efficiency of enhanced oil recovery or the transport of non-aqueous phase liquids in the soil via water or surfactant flooding. Mahe et al. [74]studied experimentally the attachment and detachment of Pristine (a ramified alkane, $C_{19}H_{40}$) and Squalane ($C_{30}H_{62}$) droplets having different contact angles on a glass surface detached from the initial contact point when a critical shear rate achieved. They mainly focused on visual observation of detachment of an inverted oil droplet from a solid substrate by viewing the contact area through a microscope. They observed that the Pristine droplet adhered to the solid substrate having equilibrium contact angle of 175° deforms and leans in the direction of shear. The contact angle of the advancing edge increases, whereas that for the receding edge decreases. Finally the droplet detaches when the receding edge slides and meets the advancing edge at the downstream side of the droplet.

Dussan et al. [76] theoretically analyzed the phenomenon of a droplet removing from a solid surface in the presence of surrounding moving fluid. They developed yield criteria for the critical capillary number, *Ca*, as a function of the advancing and receding contact angles, θ_A and θ_R , for an oil droplet sliding on a plane. The capillary number, *Ca* (= $\mu U/ \gamma$) is the ratio of viscous to surface tension forces, where γ is the oil–water interfacial tension, μ_1 is the viscosity

of shearing fluid and U is the free stream velocity of shearing fluid. The analysis was based on asymptotic theory valid for small contact angle hysteresis ($\theta_A - \theta_R$).

Li and Pozrikidis [77] studied the three-dimensional analogue of droplet detachment from solid surface under the shear flow in the limit of low *Re* using boundary integral method. They computed the shapes of droplets as a function of *Ca* for different geometries of the contact line. It was concluded that the droplet with elliptical contact lines likely to dislodge or breakup before the droplet with circular contact line. Basu et al. [78]developed a mathematical model to predict the critical shear rate for the detachment of partially wetting droplet (θ_e = 120°) and non-wetting droplet (180°) based on visual observation described by Mahe et al. [74] According to Basu et al. [78] , a partially wetting droplet detaches from a substrate when the adhesive and the body forces overcome by the lift force. Dimitrakopoulos and Higdon[79] theoretically studied two dimensional droplets removing from a solid substrate in shear flow. They found the critical shear rate of droplet detachment as a function of shear rate, contact angle hysteresis, Bond number, and viscosity ratio of droplet.

In addition to these applications, recently, a great interest has arisen for fuel cells [80-82]and the concomitant requirements of managing the water. This has led to several papers studying the shedding of droplets placed on a fuel cell gas diffusion membrane with small channel geometries. Zhang et al. [83] present information on the critical airflow for a given drop diameter. Zhu et al. [82] numerically investigated the dynamic behaviour of liquid water entering a polymer electrolyte fuel cell channel through a GDL pore while is exposed to shearing airflow. They used a two-dimensional Volume of Fluid (VOF) method to explicitly track the liquid-gas interface. They found that critical air velocity decreases with increasing droplet size and decreasing pore diameter. Simplified stability analysis based on macroscopic force balances and geometry

approximations for predicting the onset of instability leading to removal of water droplets at gas flow channel interface have been reported in Chen et al.[84] and Kumbur et al. [85] . Chen et al. [84] used a simplified model of adhesion that assumes a circular contact line and a stepwise distribution with the advancing and receding contact angles on the downstream. As an improvement, Kumbur et al.[85] introduce a linear distribution but still assume a circular contact line.

Ding and Spelt[86] numerically investigated the critical conditions for displacement and deformation of three-dimensional droplets at moderate Reynolds numbers. They found that at moderate Reynolds numbers, inertia has a significant influence on the critical Weber number. More recently, they numerically studied the deformation and mobility of a three-dimensional droplet on both hydrophilic and hydrophobic surfaces[87] under the shear flow. In their studies, viscosity and density ratios between the dispersed and continuous phases kept approximately equal to unity. They measured the critical conditions for the onset of entrainment for both pinned and moving droplets at moderate Reynolds numbers for various initial droplet shapes. Their results showed that the initial droplet shape has slight effect on the quasi-steady state of a steadily moving droplet while it has a more significant effect on the onset of motion.

In spite of all above studies on droplet shedding, rarely a single numerical study has examined a wide range of wettabilities for drop shedding (runback) and for a large range of drop volumes. Based on our knowledge, no literature data could be found for drag coefficient and adhesive shear stress of droplets on surfaces with various wettabilities. In this study, the results will be most applicable to aerodynamics icing phenomena. The intention of the present work is a detailed study of the fluid mechanics of drop shedding on surfaces of various wettabilities. Such

a study would give great knowledge on droplet shedding and the flows around the droplet which would be useful to have better understanding of this phenomenon.

1.4 Objectives

The goal of this study is to understand of droplet coalescence and droplet shedding phenomena using numerical simulation. Specifically, this study will explore what occurs when a second droplet impacts an initially sessile droplet resting on surfaces ranging from hydrophilic to hydrophobic and ultimately superhydrophobic. Furthermore, it will investigate the surface wettability on droplet shedding under the shear flow. The task at hand can be categorized into the followings.

- Provide detailed understanding of the effect of surface wettability, droplet speed, droplet size and center to center distance between the droplets on the morphology of coalescing droplets.
- Quantify the coalescence behavior and develop correlations relating the maximum spreading of the merged droplet to the impact parameters.
- Study the effectiveness of water repellency of superhydrophobic surfaces under coalescing conditions.
- Investigate the effect of surface wettability on critical air velocity for droplet shedding by air flow.

1.5 Thesis outline

In chapter 2, the numerical methodology is fully presented. This chapter covers *Volume of Fluid* model, discretization schemes, dynamic contact angle, and the solver employed in this study. At the end of this chapter, the required equipment of the experiments consists of a droplet generator, some synchronization electronics, a high speed camera, lighting and a frame to hold these components together is described.

Chapter 3 presents the results obtained from numerical simulation for both droplet coalescence and droplet shedding. The numerical results are validated against experimental data. In this chapter the results related to the effect of wettability are presented. To begin the discussion, Chapter 3 presents the general merging, spreading and recoiling behavior of droplets merging for the case of a head-on impact. Furthermore, in Chapter 3 the effect of offset for all surfaces are presented. In order to quantify the behavior across all surfaces a regression model is proposed to unify the previously mentioned impact parameters. This model covers both the merging dynamics for hydrophilic to superhydrophobic surfaces with various offsets.

Chapter 4 includes the conclusions of this work followed by useful suggestions for future studies.

2 Methodology

In this Chapter the methodology and formulation that has been employed in this study is briefly described and the details of discretization techniques applied in the framework of the finite-volume numerical method are outlined. The computational domain and applied boundary conditions are described in details. To validate the model, two set of experiments has been chosen to present in this thesis; (a) droplet coalescence [88] and (b) droplet shedding in wind tunnel [7].

There are currently two general approaches to model multi-phase flows; Eulerian and Lagrangian methods. In Lagrangian methods, the grid is moving with the interface velocity. On the contrary, in Eulerian method the grid is fixed, Therefore does not move with the interface. In both approaches the grid may be unstructured or structured. Since the interface between the two phases with different densities is a discontinuity in the computational cells, special resolution is required at the free surface to capture this discontinuity. Eulerian method has shown to be more difficult in resolving the interface between two phases. There are different Eulerian methods available, e.g. Line Segments[89], Height Functions[90], and Marker method[91]. One of the widely used Eulerian methods which have been shown to be very promising is Volume of Fluid (VOF) model[51]. Details of the flow model are described by several investigator [36,92,93]; here only a brief outline is presented.

All numerical simulations were performed using Open source Field Operation And Manipulation (OpenFOAM) C++ libraries, a free-source CFD-toolbox developed by OpenCFD Ltd[94]. It is based on the finite-volume numerical method with the co-located variable arrangement for solving systems of transient transport equations on arbitrary unstructured meshes in three-dimensional space.

2.1 Volume of Fluid (VOF) Method

The computational model governing the fluid flow due to the drop impact and coalescence process are described by the mixture continuity and momentum equations,

$$\vec{\nabla} \cdot \vec{U} = 0 \tag{2}$$

$$\frac{\partial \rho \vec{U}}{\partial t} + \vec{\nabla}.(\rho \vec{U}\vec{U}) = -\vec{\nabla} p^{*} + \vec{\nabla}.(\mu.\nabla \vec{U}) + (\vec{\nabla}\vec{U}).\vec{\nabla}\mu - g.x\vec{\nabla}\rho + F_b \tag{3}$$

where $\vec{U}$ is the velocity vector, t is time, x is the coordinate vector, $p^*=p - \rho g.x$ is the modified pressure, γ is the surface tension, k is the curvature of the interface, F_b are body forces per unit mass, and f is the volume fraction which is used to compute the weighted average mixture density and viscosity based on the distribution of the liquid volume fraction,

$$\begin{aligned} \rho &= f\rho_l + (1-f)\rho_g \\ \mu &= f\mu_l + (1-f)\mu_g \end{aligned}, \tag{4}$$

where the subscripts l and g denote the liquid and gaseous phase, respectively. VOF method uses a scalar field, f, whose value is unity in the liquid phase and zero in the gas. When a cell is partially filled with liquid, f will have a value between zero and one.

$$f = \begin{cases} 1 & \text{in liquid} \\ > 0, < 1 & \text{at the liquid-gas interface} \\ 0 & \text{in gas} \end{cases} \tag{5}$$

The values between zero and one represent the interface of two phases, schematically shown in Fig. 8.

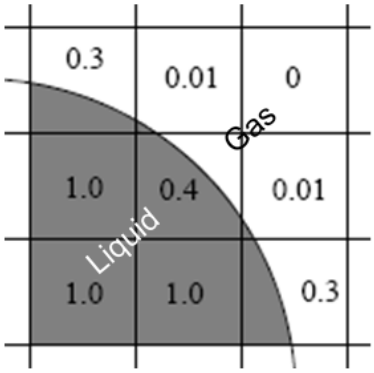

Figure 8: Volume fraction representation in each cell containing both phases.

It is crucial in numerical simulations of free surface flows using the Volume of Fluid (VOF) model to assure boundedness and conservativeness of the phase fraction. In flows with high density ratios, small errors in volume fraction may lead to significant errors in calculations of physical properties. Therefore, accurate calculation of the phase fraction distribution is vital for a proper evaluation of surface curvature, which is required for the determination of surface tension force and the corresponding pressure gradient across the free surface. It should be mentioned that the accuracy of interface reconstruction depends on mesh resolution which renders VOF methods grid dependent. The discontinuity in *f,* is propagating through the computational domain according to the following,

$$\frac{\partial f}{\partial t} + (\vec{V} \cdot \vec{\nabla}) f = 0 \tag{6}$$

The governing equations are discretized using finite volume scheme for general unstructured polyhedral cells. Following the method outlined by Rusche,[95] the volume fraction equation is formulated with a bounded compression scheme, which facilitates a sharp interface between phases. This is achieved by introducing an extra artificial compressive term into the volume fraction equation,

$$\frac{\partial f}{\partial t} + (\vec{U} \cdot \vec{\nabla}) f + \vec{\nabla}.(\vec{U}_r f(1-f)) = 0 \tag{7}$$

where, $\vec{U}_r$ is the vector of relative velocity normal to the interface which is used to compress the interface,

$$\vec{U}_r = k_c n \max \frac{\left| n.\vec{U} \right|}{\left| S \right|^2} \tag{8}$$

Where, k_c is an adjustable coefficient used to adjust the amount of compression. *S,* is the surface area vector. We used k_c = 1.5 which was also shown by Rusche[95] to provide sharp interface between phases. The interface unit normal *n* is computed by taking the gradient of a smoothed (via elliptic relaxation) volume fraction f^* at the cell faces

$$n = \frac{\nabla f_f^*}{\left| \nabla f_f^* \right| + \delta} \tag{9}$$

It is noted that due to the function of *f(1-f)*, the artificial compressive term is only active near the interface. Therefore it does not affect the solution outside this region. The main benefit of such formulation is in the possibility of capturing the interface region much more sharply in comparison to the classical VOF approach[92]. Numerical diffusion, unavoidably presented through the discretization of convective terms, can be controlled and minimized through the discretization of the compression term, thus allowing sharp interface resolution.

The continuum surface force (CSF) method[92] is used to model surface tension as a body force (F_b) that acts only on interfacial cells.

$$F_b = \gamma k \nabla f \tag{10}$$

Where, *k*, is the mean curvature of the free surface, calculated by

$$k = -\nabla.\left(\frac{\nabla f}{|\nabla f|}\right) \tag{9}$$

2.1.1 Numerical setup and discretization

All computations were carried out using the numerical code OpenFOAM, utilizing a cell-center-based finite volume method on a fixed unstructured numerical grid. The overall solution strategy is based on the Pressure Implicit with Splitting of Operators (PISO) algorithm[96]; however, it departs from its typical implementation since the implicit solution of the momentum equations is not utilized. After the time step is adjusted to meet the specified maximum courant number, the volume fraction equation is solved, then the resulting field is smoothed and the unit normal vector and interface curvature is calculated based on that. Finally, the Pressure Implicit with Splitting of Operators (PISO) algorithm is used to calculate the pressure and velocity.

The solution domain is subdivided into a number of cells with computational points placed at cell centroids. Each two cells share one cell face. This face surface normal victor is defined as depicted in Fig 9.

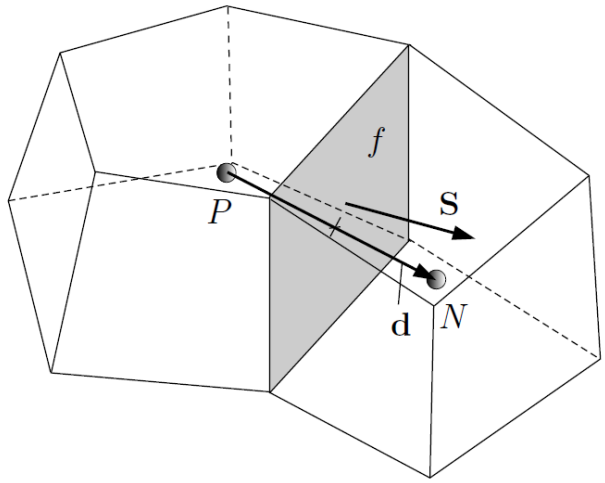

Figure 9: Discretization of solution domain, from OpenCFD Ltd.[6]

The equations are discretized following the finite volume technique. Time derivative terms are discretized using an implicit Euler scheme. The terms comprising spatial derivatives, as diffusion and convective terms, are converted into integrals over surfaces bounding each cell using Gauss' theorem. The source and transient terms are discretized using the midpoint rule and integrated over cell volumes. The integration is performed by summing values at cell faces, calculated by interpolation. For the evaluation of gradients a linear face interpolation is used.

In discretization of the convective terms a cell-face interpolation based on high resolution differencing scheme is used with a limiter evaluated based on the ratios between volume flux gradients obtained at the adjacent cell-faces and cell centers[97]. The expression for the interpolated cell face value ϕ_f of a variable ϕ, which is calculated at computational points P and N in Fig. 9, reduces to the following expression

$$\phi_f = \xi(\phi_p - \phi_N) + \phi_N \tag{10}$$

where ξ is is calculated using weighting factor ψ from the limited scheme

$$\xi = \psi f_d + (1-\psi)\prod(U_f.S_f) \tag{11}$$

Where $f_d = \overline{fN} / \overline{PN}$, and the operator $\prod(U_f.S_f)$ is a switch which accounts for the flow direction defined as

$$\prod(V_f.S_f) = \begin{cases} 1 & \text{for } \mathrm{U}_f.S_f > 0 \\ 0 & \text{for } \mathrm{U_f}.S_f < 0 \end{cases} \tag{12}$$

At the beginning of each (time) iteration, the time step is adjusted based on the Courant number such that it is sufficiently small in order to ensure stability of the numerical solution procedure. It is worth mentioning that using Courant number is necessary for solving the nonlinear systems of equation, which is the case in this study.

The new time step is firstly obtained from the expression

$$\Delta t = \min\left\{\min\left[\min\left\{\frac{Co_{\max}}{Co_0}\Delta t_0, \left(1+\lambda_1\frac{Co_{\max}}{Co_0}\right)\Delta t_0\right\}, \lambda_2\Delta t_0\right], \Delta t_{\max}\right\} \tag{13}$$

where the Courant number is calculated from

$$Co = \frac{\left|U_f.S_f\right|}{d.S_f}\Delta t \tag{14}$$

where d is a vector between calculation points of control volumes sharing the face, i.e., $d = \overline{PN}$ and Δt is time step. The local Courant number Co_0 is determined using values for U_f and Δt from previous time step. To avoid time step oscillations that may lead to instability, the increase of the time step is damped using factors λ_1 and λ_2. Depending on the specific case studied, the size of the time step may vary during the calculation. It was found by experience that the limiting value for the Courant number should not exceed $Co_{max} \approx 0.2$, which is the value used in this study.

2.2 Initial and boundary conditions

At the initial time, the distribution of volume fraction is prescribed throughout the domain, defining the position and the shape of the interface at the beginning of the calculation. The initial droplet velocity is set equal to the droplet impact velocity from the validating experiments. As it shown in Fig. 9 the top and the sides boundaries are open with prescribed total pressure consisting of static and dynamic pressure, thus allowing the static pressure to be adjusted according to the calculated velocity field. At the walls a zero gradient is set for the modified pressure and the no slip condition is applied for velocity.

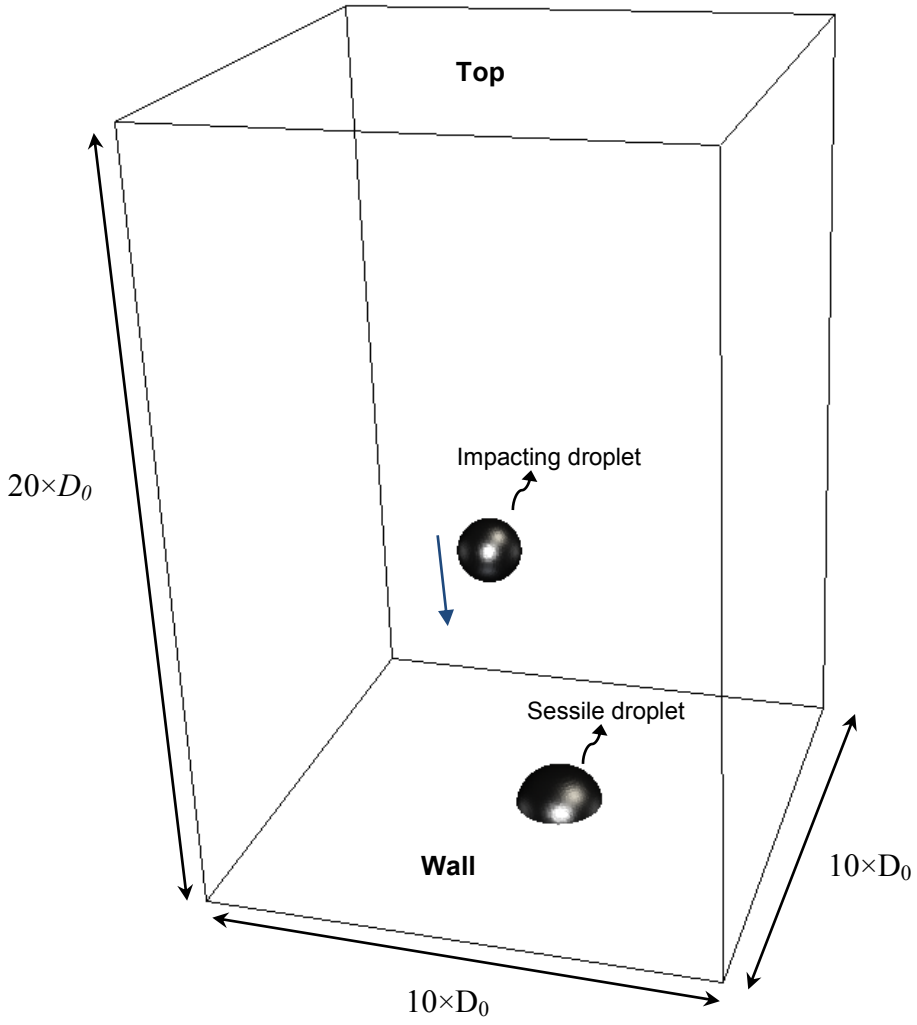

Figure 10: Initial case configuration.

The wettability effects at the substrate are taken into account by using the dynamic contact angle which is assumed to be a function of the contact line velocity. There are several empirical formulae expressing the dependence of the dynamic contact angle on the contact line velocity.[98,99, 100] Most of them are in the form of the Hoffman–Tanner–Voinov law, or in a more

general form derived by Cox.[99] The predicted values of the dynamic contact angle are very similar for all of these models. In this study, the correlation of Kistler[101] is used to calculate the dynamic contact angle for each time step.

$$\theta_d = f_H(ca + f_H^{-1}(\theta_e)) \tag{15}$$

where f_H^{-1} is the inverse function of the "Hoffman's" empirical function which is given in the following form.

$$f_H = \arccos\left\{1 - 2\tanh\left[5.16\left[\frac{x}{1+1.31x^{0.99}}\right]^{0.706}\right]\right\} \tag{16}$$

The Capillary number is defined as

$$Ca = \frac{\mu U_{cl}}{\gamma} \tag{17}$$

where μ is the dynamic viscosity, γ the surface tension and U_{cl} the contact line velocity which is roughly approximated by using the velocity at the interface in the first computational point above the wall, i.e. the velocity component normal to the contact line and tangential to the wall.

Most surfaces are not ideally smooth and are subject to the effect of contact angle hysteresis. In order to consider this effect in the numerical model, the equilibrium contact angle θ_e in Eq. (16) is replaced by either the advancing contact angle, θ_A, or the receding contact angle θ_R depending on the direction of the velocity vector at the contact line.

All simulation is performed on a three dimensional unstructured mesh using a recently developed adaptive local mesh refinement technique[102], which enhances the accuracy at the interface region and achieves low computational cost compared to the case of a uniform mesh with the same resolution. A base mesh is used and the cells at the region of the interface are subdivided according to the levels of local mesh refinement, while the interface lies always in the

densest mesh region since the mesh is reconstructed at every time steps. The cell size used in this study is set based on a mesh refinement study in which the grid size is progressively decreased until no significant changes are observed in the simulation results. The mesh resolution is characterized by the number of cells per the droplet diameter. From the mesh refinement study, the optimum mesh size was found to be 25 cells per drop diameter and 2 levels of local grid refinement at the interface region. This resulted in a resolution of 50μm at the interface region. Therefore, this mesh size was used for all simulations throughout this article. Figure 11 shows the comparison of an unrefined mesh with adaptive local refined mesh.

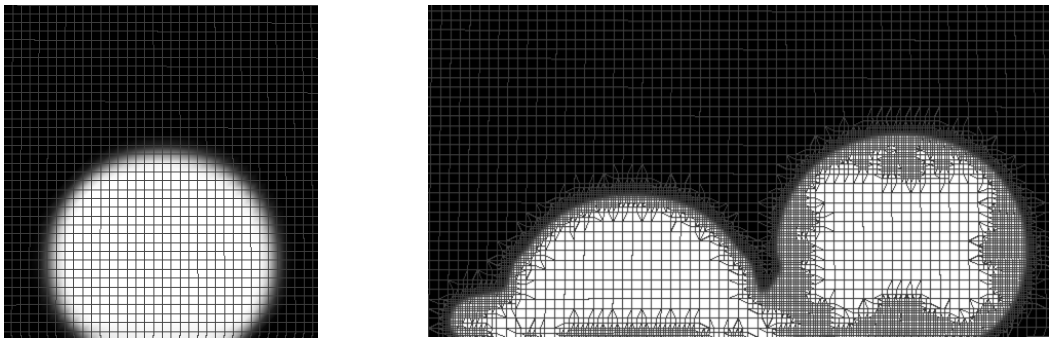

(a) **(b)**

Figure 11: Computational domain for a) unrefined and, b) adaptive local refined mesh[51].

2.3 Experimental Validation

In order to validate the numerical method and ascertain the quantitative data, numerical results are compared to two different experiments performed in the Multiphase Flow Laboratory at Concordia University[88] and the University of Alberta[7]. In the following section, a brief overview of the experimental facilities is explained.

2.3.1 Experimental Setup for Droplet Coalescence

The first experiment used to validate the numerical results was performed at Concordia University by Graham[88]. Hardware used for performing experimentation includes a positioning system, imaging equipment, substrate and droplet generator which are mounted on an optical bench and breadboard. The sessile droplet is aligned using a screw drive micro positioning stage. Figure 12 schematically depicts the setup.

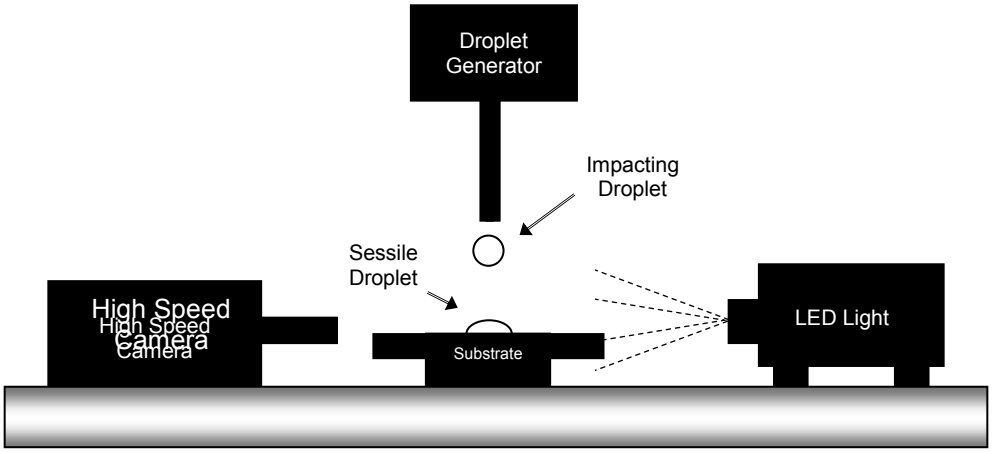

Figure 12: Schematic of the experimental setup[51].

Droplets are formed at the tip of a syringe and detach once sufficiently large. Their sizes are controlled based on the gauge of the needle and their impact velocity comes from gravity. Flow through the droplet generating system is driven by a pressurized water tank at a pressure below 10*psi* and controlled by a solenoid valve which is synchronized to the high speed camera. Substrates used include polished aluminum, Teflon, Fluoropel coated aluminum, Teflon sanded with 320 grit sandpaper and WX2100 sprayed on aluminum. The static and dynamic contact angles measured on the above mentioned substrates are shown in Table I.

Table I. Surface properties.

Material	Static	Advancing	Receding
Aluminum	73° ± 3°	90° ± 5°	50° ± 5°
Teflon	93° ± 3°	108° ± 5	71° ± 5°
Fluoropel	108° ± 3°	121° ± 5°	86° ± 5°
Teflon320	135° ± 3°	151° ± 5°	108° ± 5°
WX2100	154° ± 3°	162° ± 5°	148° ± 5°

2.3.2 Experimental Setup for Droplet Shedding

In order to validate the numerical results for droplet shedding under the shear flow, the experimental results performed in the 215.9 mm× 469.9 mm test section of a low-speed wind tunnel at the University of Alberta are used[7]. Side-view schematic of the wind tunnel with detailed imaging of the streamlined body used for drop-shedding tests by shear flow is shown in Fig. 13.

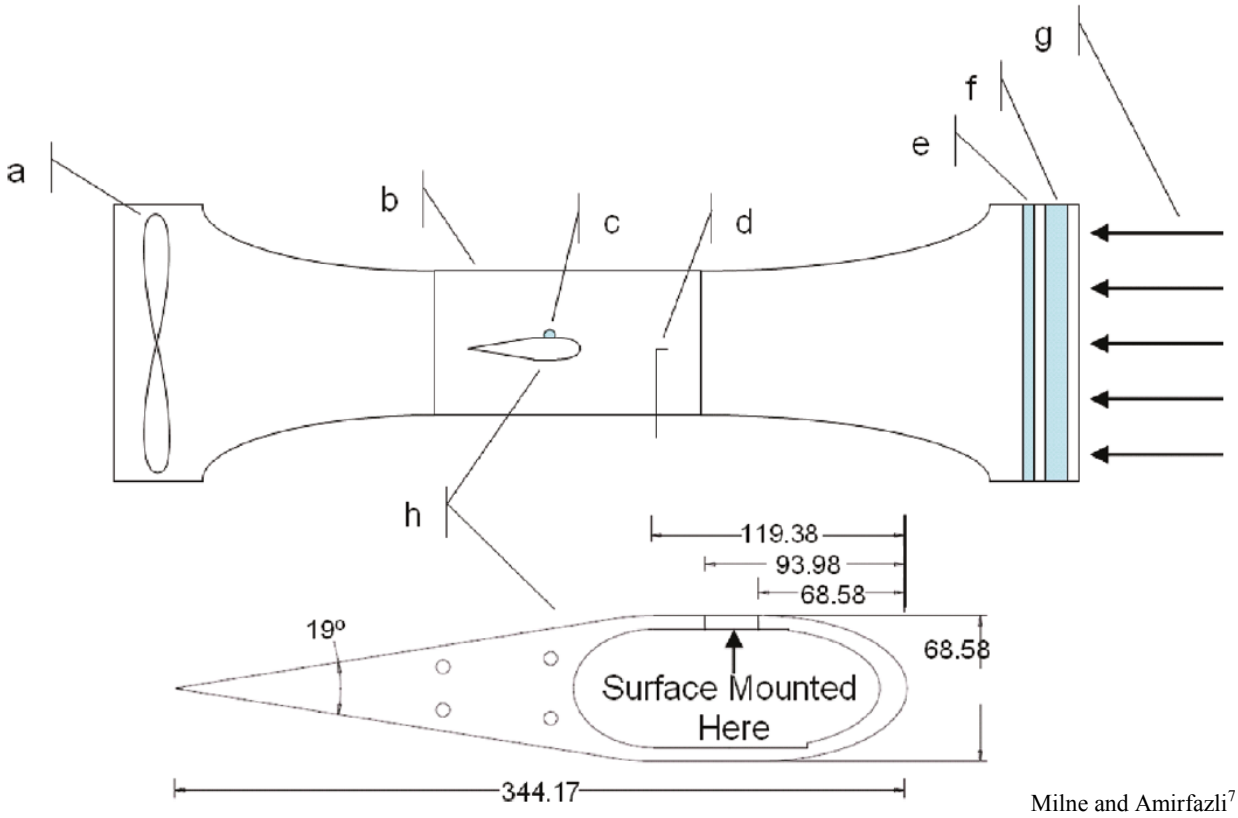

Figure 13:Side-view schematic of the wind tunnel with detailed imaging of the streamlined body used for drop-shedding tests by shear flow: (a) fan; (b) working section (469.9 mm (h) _ 927.1 mm (l) _ 215.9 mm (d)); (c) drop on the surface mounted in the streamlined body, h; (d) pitot tube; (e) screen; (f) flow straighteners; (g) airflow; and (h) streamlined body and detailed image of the same. All linear dimensions are in millimeters. The cutout through the center of the body allows access for inserting and removing the surface sample and adjusting it to maintain the flush top surface. The camera view is into the page, and the light is mounted behind the tunnel pointing out of the page[7].

To analyze the fluid flow behavior inside the wind tunnel and its effect on droplet movements, part of the wind tunnel test which includes the stream lined body with front section in the shape of semi-ellipse (major axis 68.58mm, minor axis 34.29mm) is considered. The dimensions of the test section are 470 mm × 235 mm. Figure 14 depicts a schematic of the computational domain and the corresponding mesh. The inset picture shows the location of droplet which is 10 cm downstream the leading edge. The whole geometry is meshed using

Gambit 2.3, a meshing tool from Ansys Inc[103]. The geometry consists of two different meshing zones. The mesh is very fine around the streamline body and also the region where droplet is placed. The coarser mesh is used in the region more than 4 times of droplet diameter away from streamline body which consists only of gas phase. A base mesh of 2 million cells is used and the cells at the region of the interface are subdivided according to the levels of local mesh refinement, while the interface lies always in the densest mesh region since the mesh is reconstructed at every time steps. This can facilitate capturing a sharp interface between the two phases.

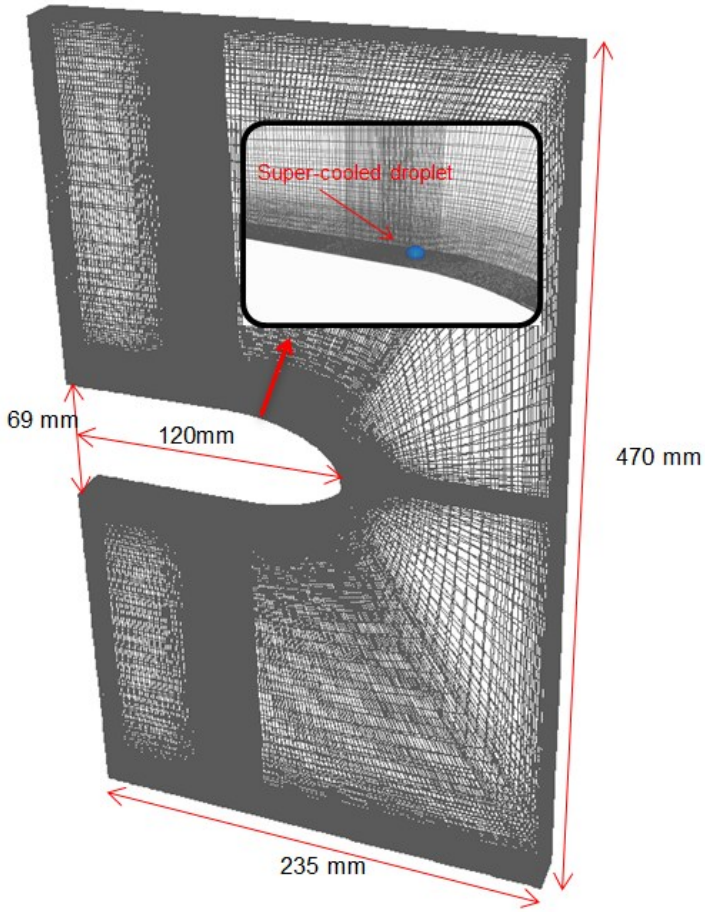

Figure 14: Computation domain and mesh for droplet shedding inside wind tunnel section

The static and dynamic contact angles of substrates used for modeling the droplet shedding by air flow are shown in Table II.

Table II. Maximum and minimum contact angles for droplet shedding.

Water-SHS					
	Average θ_{max}	StDev	Average θ_{min}	StDev	$\Delta\theta$
Air flow	161.4°	0.8	129.8°	8.9	31.6°
Water-Teflon					
	Average θ_{max}	StDev	Average θ_{min}	StDev	$\Delta\theta$
Air flow	124.3°	0.7	108.2°	3.4	16.1°
Water-PMMA					
	Average θ_{max}	StDev	Average θ_{min}	StDev	$\Delta\theta$
Air flow	76.3°	3.3	53.1°	3.8	23.2°

3 Results and discussions

This chapter presents the simulation results for two interesting phenomenon including droplet coalescence and droplet shedding which has many application in industry, especially in the aerospace industry. The results for droplet coalescence are based on the author's two published manuscripts in *Langmuir*[51] and *Physics of Fluid*[104].

3.1 Droplet Coalescence

As a first step, the numerical results were validated by comparing the free surface and spread diameter with the experimental results for different droplet sizes, impact velocities and center to center distances between two droplets. Simulations were carried out by varying the separation between the sessile and the impacting droplet from the axisymmetric drop on drop to sufficiently large offsets to allow the impinging droplet to spread on the dry surface prior to merging.

The main parameters for the collision of isothermal droplets include the droplet diameter, D_0, the impact velocity, U_0, the contact angle of droplet with the substrate, θ_s, the contact angle hysteresis, the droplet kinetic viscosity, μ, the droplet density, ρ, the surface tension, γ, the gravitational acceleration, g, and offset distance L. To quantify the overlap between droplets (see Figure 15), an offset ratio is defined as

$$\lambda = \frac{L}{D_0} \tag{18}$$

where D_0 is the droplet diameter. An offset distance of zero results in a head-on collision.

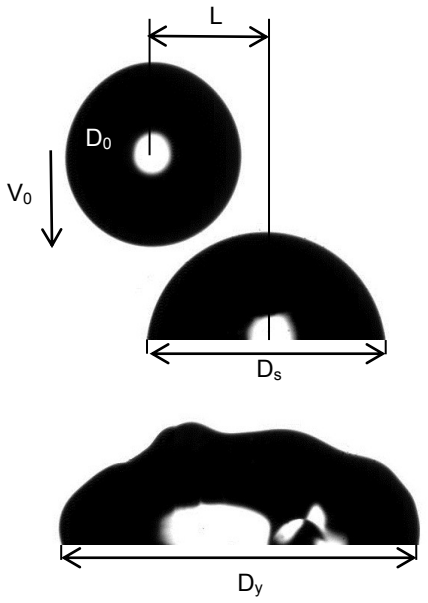

Figure 15: Definition of the main dimensions characterizing the droplet coalescence[104].

To measure deviations from ideal behaviour a non-dimensional spreading length similar to the work done by Li et al.[48] is defined in equation 19. Should the droplet detach from the surface, the spreading length is defined as zero.

$$\psi = \frac{D_Y}{D_0 + L} \tag{19}$$

The spreading times are non-dimensionalized as,

$$\tau = t\frac{U_0}{D_0} \tag{20}$$

In addition, the investigation of the coalescence phenomenon requires examination of the most significant dimensionless numbers, such as the Reynolds number (*Re*), and the Weber number (*We*), defined as,

$$We = \frac{\rho_l U_0^2 D_0}{\gamma}, \quad Re = \frac{\rho_l U_0 D_0}{\mu_l} \ . \tag{21}$$

where subscript *l* represents liquid. The results of various simulations along with experiments are presented in three sections to investigate coalescence mechanisms of droplets on hydrophilic, hydrophobic and superhydrophobic surfaces. Extensive model validations based on comparisons with experimental measurements have been performed; they will be mentioned throughout the sections to follow.

As previously mentioned five types of surfaces with different dynamic contact angles are studied. Polished aluminum is the only hydrophilic surface studied. It was selected as a baseline case against which the other surfaces were compared since it is a common building material, especially in the aerospace industry. The three hydrophobic surfaces were selected because they can inexpensively be produced and applied to aluminum in order to investigate the whole range of wetting behavior (from hydrophilic to superhydrophobic) of droplet coalescence.

3.1.1 Hydrophilic Surface

Simulations are conducted to observe the coalescence of two droplets on polished aluminum surface. Coalescence dynamics can be observed from time resolved images. The air-water interface was tracked for each image and allowed the time evolution of droplet position and velocity.

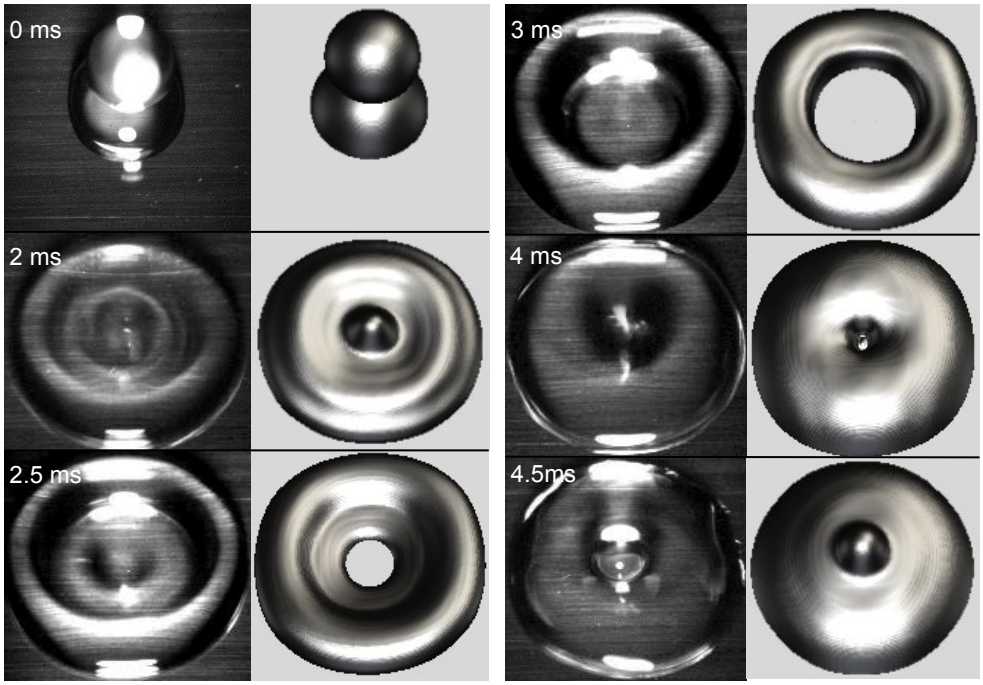

Figure 16: Time evolution of head-on impact and coalescence of two water droplets (*We*= 22, *Re* =2020, $\lambda = 0$) on a polished aluminum surface (θ_s=73º). The experimental images (left side) compared with the simulated results (right side)[104].

Figure 16 shows the time evolution images of a head-on impact and coalescence of the falling droplet with the sessile droplet on a polished aluminum surface. The diameter of each droplet is 2.55 mm, and the impact velocity is 0.757 m/s, resulting *Re*= 2020 and *We* = 22. As shown in Figure 16 after the second droplet impacts and merges with the sessile droplet, the fluid spread out horizontally forming a flattened toroidal disk shape at around 3ms. After the maximum spreading is achieved, surface tension force pulls the two edges back. The motion is radially inward, at around 4 *ms* after the impact, the merged droplet recoils. A very close qualitative agreement is observed between the calculated images and photographs.

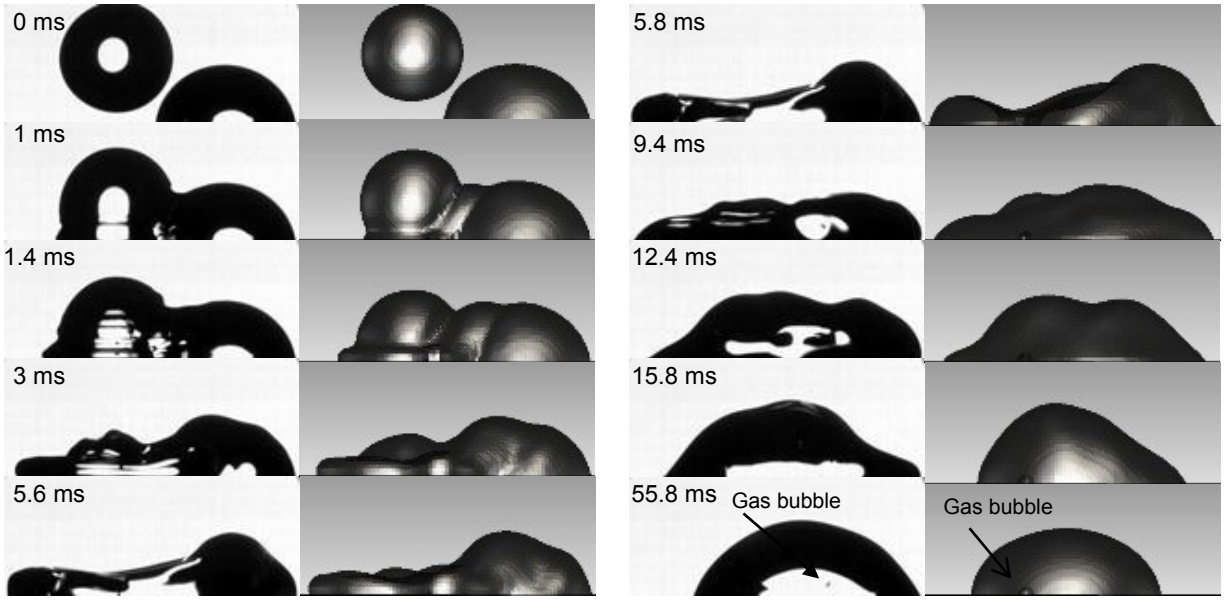

Figure 17: Coalescence of two water droplets (*We*=20.48, *Re* =1949, λ =0.97) on a polished aluminum surface (θ_s=73º). The experimental images (left side) compared to simulated images (right side)[104].

The effect of offset was studied, both experimentally and numerically, by varying the distance between droplets from the axisymmetric drop-on-drop case up to the point of merging while spreading. Figure 17 shows the side view of a collision with a moderate spacing of 0.97. The diameter of each droplet is 2.55 mm, with *Re*= 1949 and *We* =20.48. In the figure, the shape evolution of the two droplets during the coalescence phenomena from simulation is shown together with the images of the experimentally observed drop shapes. As seen from Figure 17, the impinging droplet lands partially on the sessile droplet and partially on the substrate at around 1ms. After merging with the sessile droplet, the inertia of the second droplet causes the merged droplet to deform and spread. A cavity at the center of the second droplet is formed and the merged droplet takes a toroidal shape in the spreading stage at around 5.8 ms. After reaching the maximum spread diameter (at 6ms), surface forces acting on the drop reduce the surface area

of the merged droplet. The left edge retracts faster than the right edge. The impact of the second droplet results in air entrapment in the cavity when the droplet retracts. It can be seen from this figure at 9.4ms, a bubble is formed during coalescence of two droplets. Most of the air is squeezed out when the droplet recoils. However, a small part of the air is trapped since the top of the cavity retracted faster than the bottom.

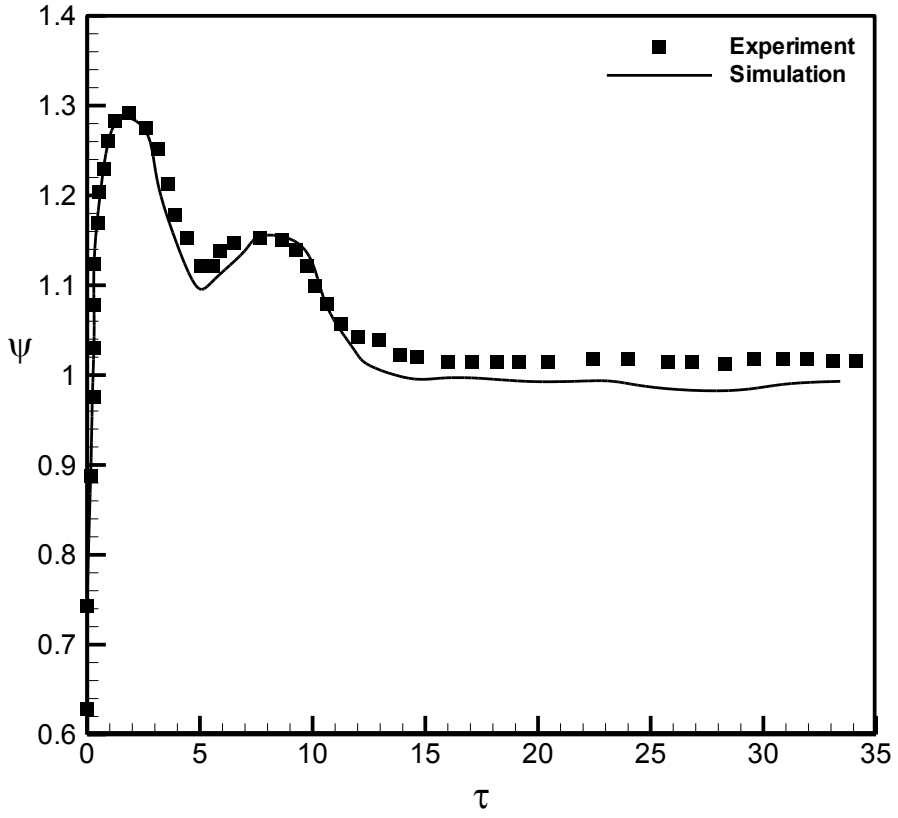

Figure 18: Temporal evolution of dimensionless spreading length for droplet coalescence on a hydrophilic surface (θ_s=73º, *We*=20.48, *Re* =1949, λ = 0.97)[104].

Figure 18 is presented to show the spreading behavior of a merged droplet by plotting the dimensionless spread length, ψ, versus dimensionless time, τ. Both numerical and experimental results show that after the falling droplet impacts and merges with the sessile droplet, the spreading length increases rapidly until it reaches its maximum value, which is about twice the

equilibrium spreading length of the sessile droplet. Once the restoring force of surface tension becomes dominant over the inertia force, the merged droplet starts recoiling. After the first retraction, the two edges continue spreading and recoiling until viscous damping overcomes the droplet oscillation. It can be seen from the experimental results that the left edge retracts from the maximum spreading point, while the right edge neither spreads nor retracts. However, the numerical results show that surface tension pulls the two edges back. The deviation of the numerical predictions from the experimental results for the equilibrium spreading length and the final placement of the merged droplet can be attributed to the droplet pinning due to surface inhomogeneity.

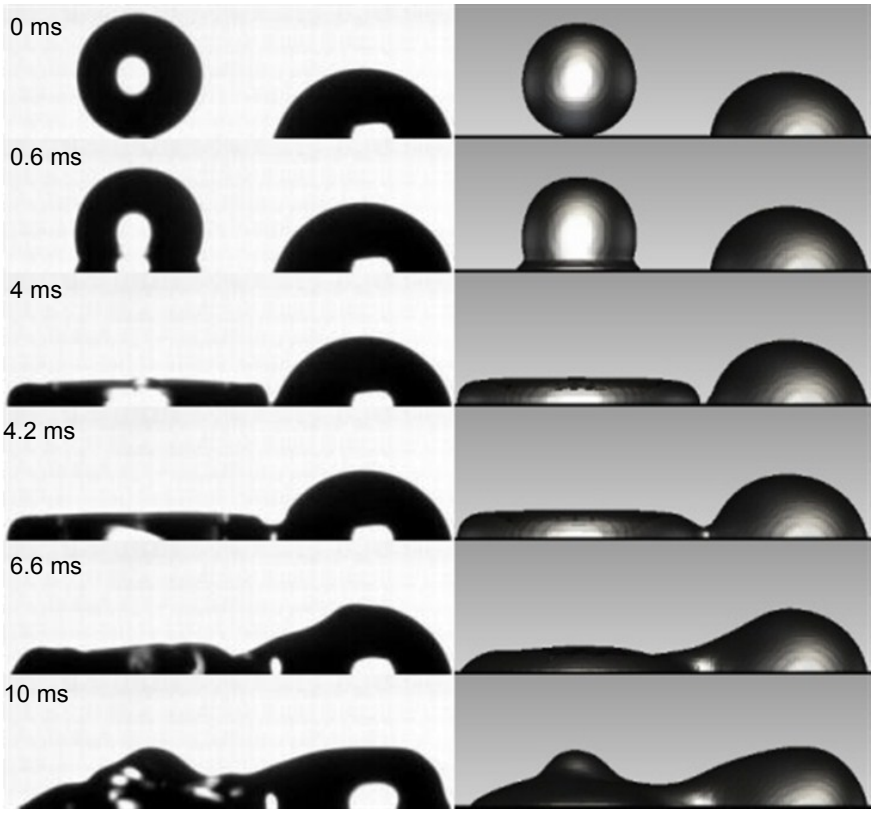

Figure 19: Coalescence of two water droplets (*We*=20.48, *Re* =1949, λ = 1.85) on a polished aluminum surface (θ_s=73º). The experimental images (left side) compared to the simulated results (right side)[104].

Once the droplet offset is greater than the radius of the sessile droplet plus the radius of the falling droplet ($L > D_0/2+D_s/2$), the falling droplet lands entirely on the substrate and therefore impacts and spreads before the coalescence occurs. After landing, the falling droplet spreads and then merges with the sessile droplet. Figure 19 shows the time evolution of two water droplets impacting on the polished aluminum substrate for a time period of 10ms. The Weber and Reynolds numbers of the droplets are We=20.48 and Re=1949 with an offset ratio of λ=1.85. It can be seen from the figure that as the falling droplet spreads, it quickly pushes into the sessile droplet and swiftly closes the gap between them at around 4ms. The neck height therefore increases very rapidly at the point of connection between the two drops, until its height becomes equal to the height of the disk formed when the impacting droplet is at its maximum extent (at 4.2 ms). It can be assumed that the expansion of the neck is driven by surface tension and is opposed by viscous forces. After that the flattened droplet begins to recover; its height increases, at approximately 10ms, and a distinct neck once again forms, which grows much more slowly. From this point, the procedure is similar to the static coalescence case, since most energy has been dissipated and the merged droplet slowly oscillates.

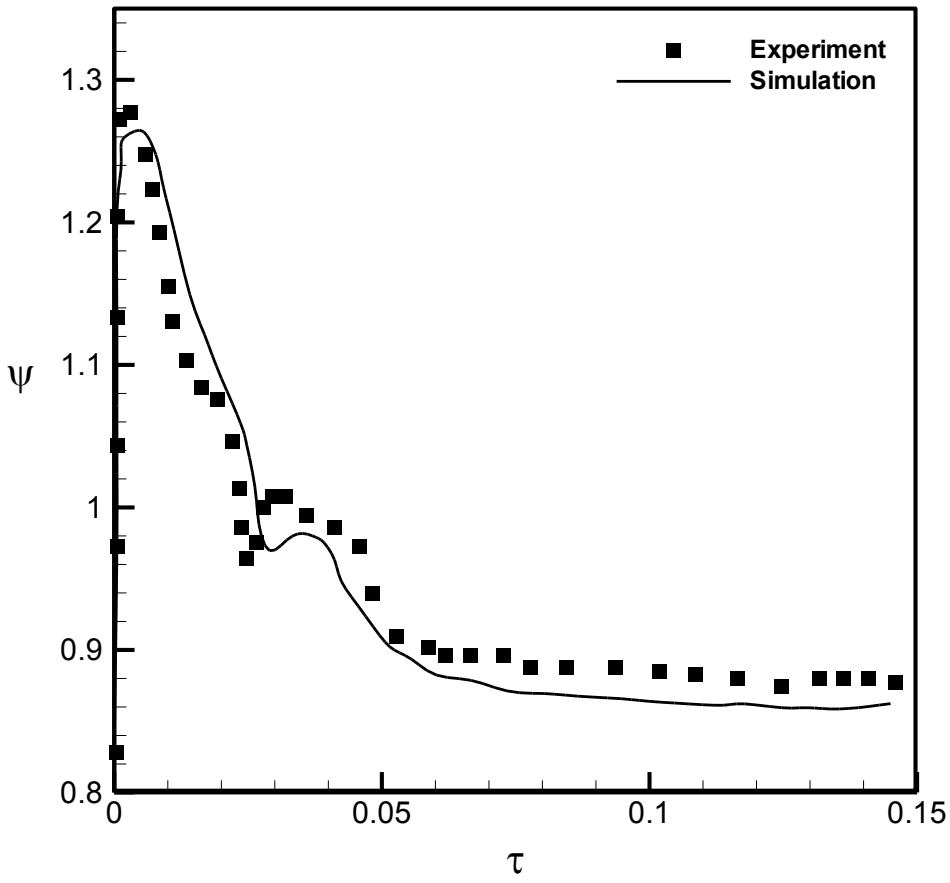

Figure 20: Temporal evolution of dimensionless spreading length for droplet coalescence on a hydrophilic surface (θ_s=73º, *We*=20.48, *Re* =1949, λ = 1.85)[104].

Figure 20 shows the comparison of simulated results with the experiments for the evolution of dimensionless spreading length versus dimensionless time. It can be observed from this Figure and Figure 18 that by increasing the offset ratio, the maximum spreading is slightly decreased. The deviation of the simulation results from experiments magnifies during the recoiling process which can attributed to pinning of the surface during the contact line retraction at the right edge of the merged droplet due to inhomogeneity of surface roughness.

3.1.2 Hydrophobic Surfaces

Binary droplet behavior in response to increased hydrophobicity is studied by using three surfaces that range from nearly critical to hydrophobic, to superhydrophobic. Simulation tests are conducted to observe the coalescence of two droplets on three types of hydrophobic surfaces (1-Teflon, 2-Floropel, 3- Sanded Teflon). Coalescence dynamics can be observed from time resolved images.

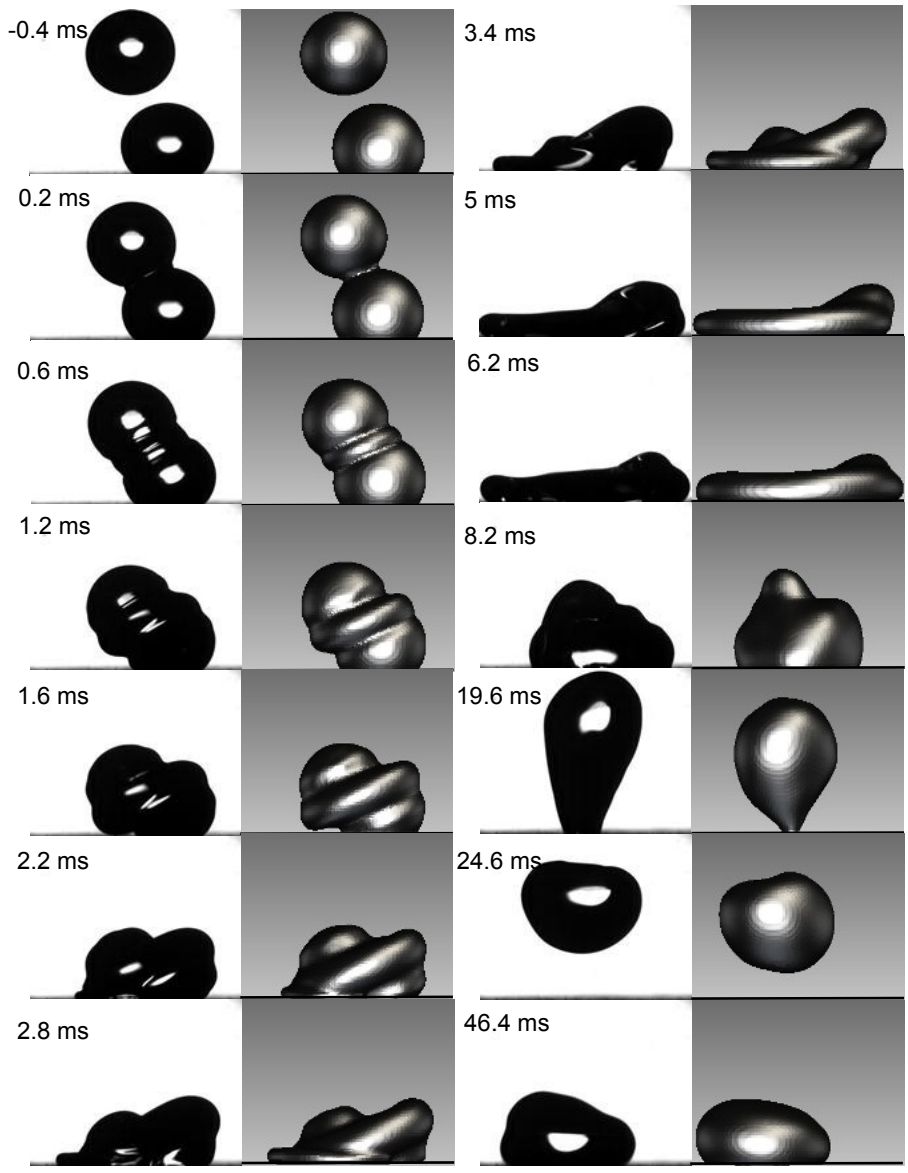

Figure 21: Coalescence of two water droplets (*We*=28, *Re* =2099, λ = 0.4) on a hydrophobic surface (θ_s=135º). The experimental images (left side) compared to simulated images (right side)[104].

Figure 21 shows time evolution images of a near head-on impact and coalescence of the impinging droplet and the sessile droplet on a sanded Teflon surface with a static contact angle of 135° and contact angle hysteresis of 43º. Although this surface is highly hydrophobic, but it cannot be recognized as a superhydrophobic surface, since it has a high contact angle hysteresis. The diameter of each droplet is 2.2 mm, and the impact velocity is 0.954 m/s, resulting in *Re*= 2099 and *We* = 28. It can be clearly observed from this figure that after the second droplet impacts and merges with the first droplet, the inertia of the second droplet drives the merged droplet to deform and spread. As the droplet spreads, the droplet height and spreading velocity decreases, which causes decreases in kinetic and potential energy of the merged drop. After the maximum spreading at around 6.2ms, the surface tension force causes the recoiling phenomenon to minimize the droplet surface area. Developed inertia during the recoiling process lifts the merged drop from the surface at about 20ms. At this point, the drop height starts to rise slightly, at around 15ms, and fall under the influence of gravity. Once the kinetic energy of the detached droplet is converted into potential energy the merged droplet starts to fall and spreads out on the surface. The two edges continue spreading and recoiling until viscous damping overcomes the droplet oscillation.

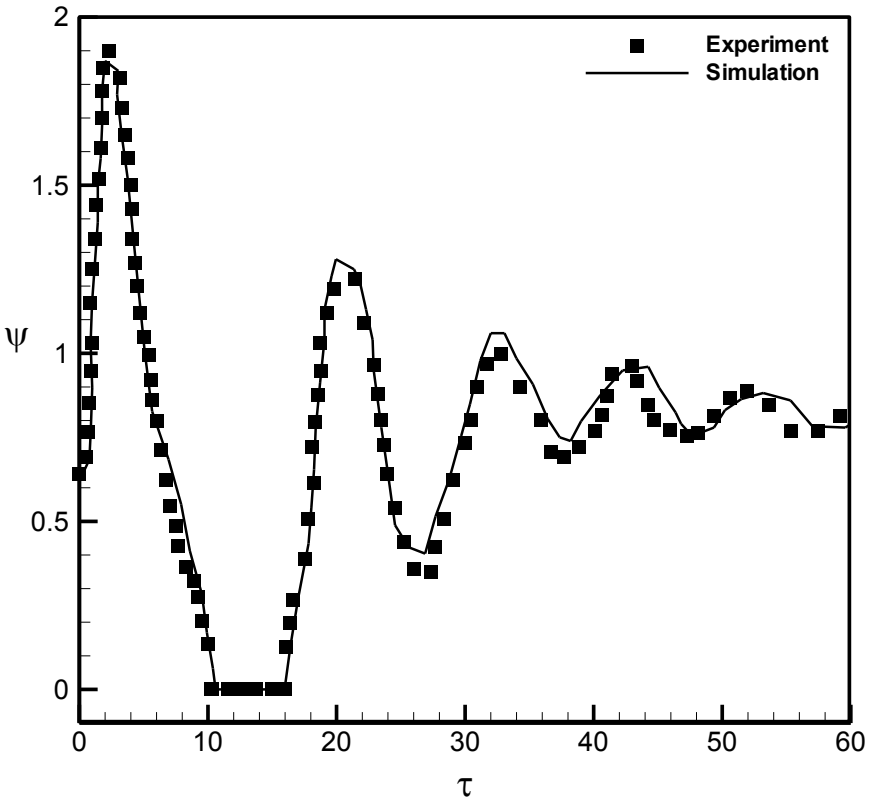

Figure 22: Temporal evolution of dimensionless spreading length for droplet coalescence on a hydrophobic surface (θ_s=135º, *We*=28, *Re* =2099, λ = 0.4)[104].

In Fig. 22, the numerically predicted dimensionless spreading length, ψ, of the merging droplet is shown as a function of the dimensionless time and compared with the experimental results. Both results indicate that after the falling droplet merges with the sessile droplet, the spreading length increases rapidly until it reaches its maximum value. The latter is approximately equal to four times the equilibrium spreading length of the sessile droplet. After this point, surface tension forces acting on the merged droplet reduce the surface area of it until the droplet detaches from the surface. For a similar droplet coalescence condition on a superhydrophobic surface, as described in the next section, the merged droplet may bounce three times before reaching to its equilibrium state. This behavioral difference is attributed to the lower wettability

and higher contact angle hysteresis of sanded Teflon compared to the low hysteresis of the superhydrophobic surface studied in Farhangi et al.[51]

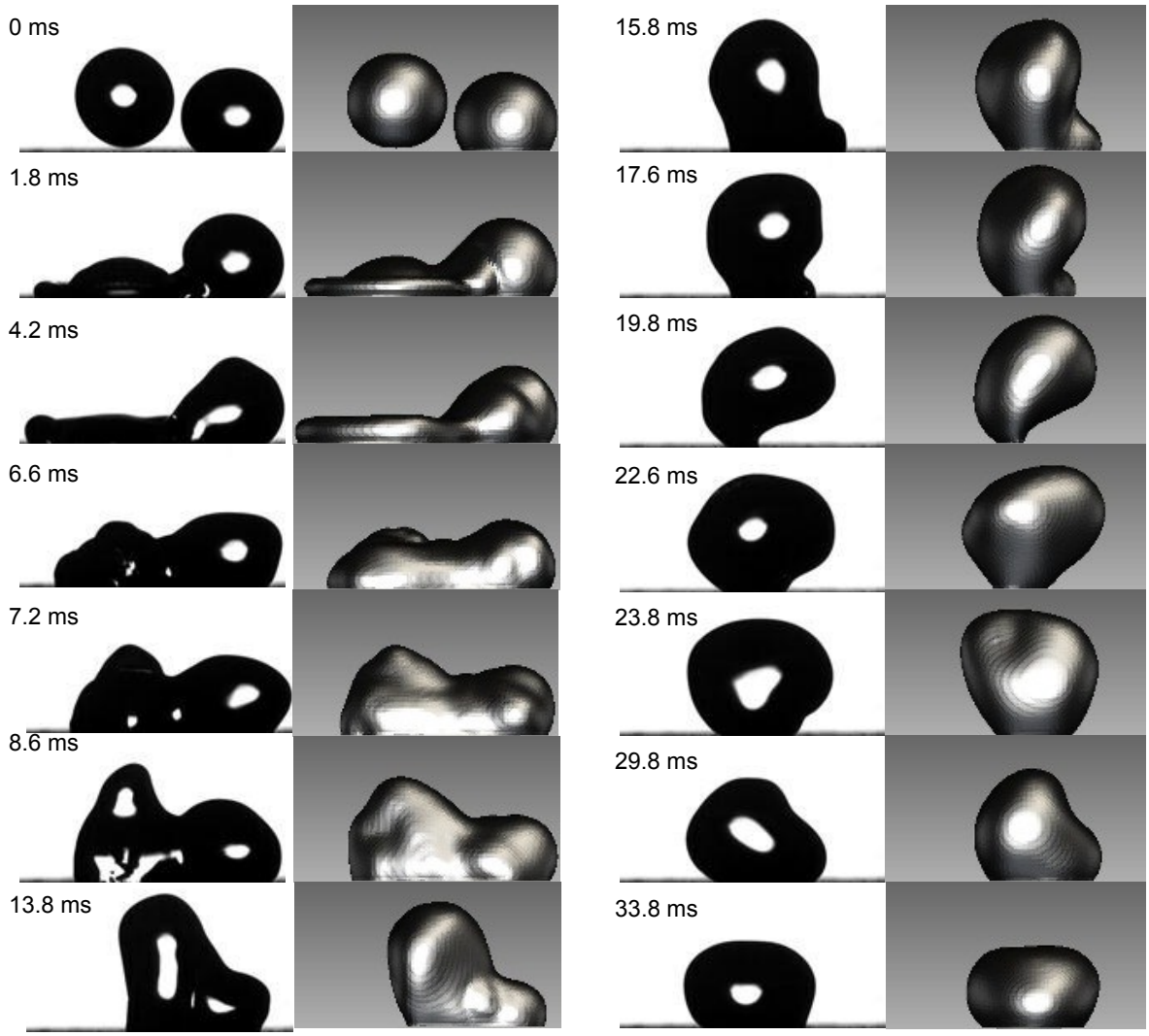

Figure 23: Coalescence of two water droplet on a hydrophobic surface (*We*=28, *Re* =2099, λ = 1.1). The experimental images (left side) compared to simulated images (right side)[104].

Simulated results of the coalescence of two droplets at a large offset are compared with the experimental images in Figure 23. The diameter of each droplet is 2.2 mm, and the impact velocity is 0.954 m/s, giving *Re*= 2099 and *We* = 28 at an offset ratio of 1.1. As shown in Figure 23, droplet first impinges on the dry section of the surface. Then the inertia causes the droplet to spread out and during the spreading the impinging droplet merges with the sessile droplet. In

contrast to the head-on and near head-on impact cases, the merged droplet at large offset cases does not detach from the surface due to the low kinetic energy that was produced during the recoiling process and that cannot overcome the surface energy.

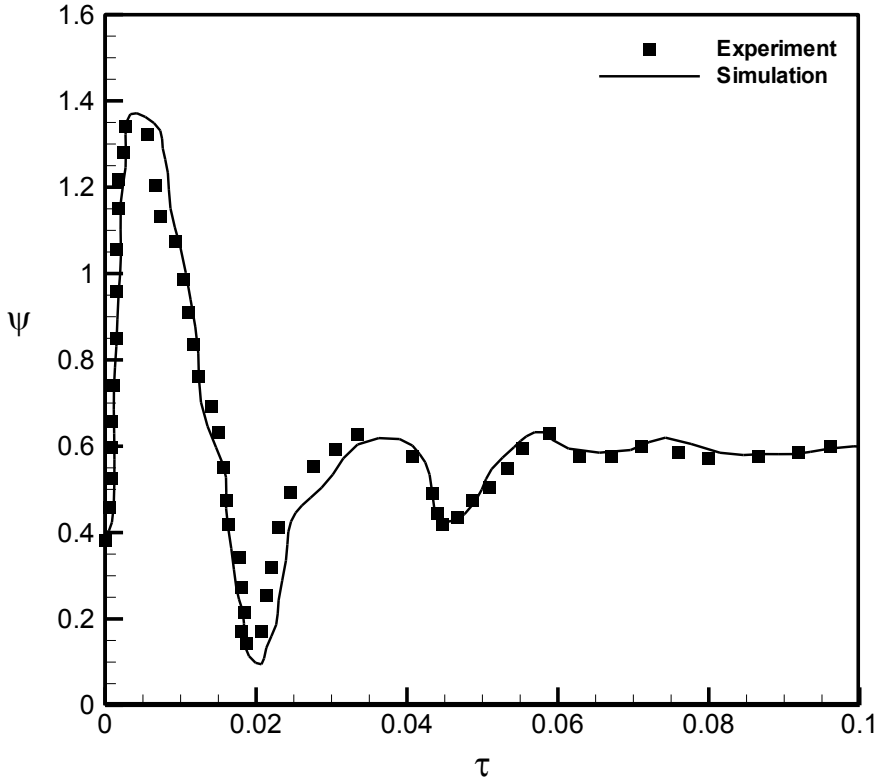

Figure 24: Temporal evolution of dimensionless spreading length for droplet coalescence on a hydrophobic surface (θ_s=135º, *We*=28, *Re* =2099, λ = 1.1)[104].

As spacing increases, the merging process imposes more viscous dissipation. Figure 24 displays the comparison of the simulated results with the experiments for the evolution of dimensionless spreading length versus time. It has been observed that by increasing the offset ratio the kinetic energy that was developed during the recoiling process is lower than the surface energy available. Therefore, the merged droplet does not detach from the surface. For a similar impact condition on a superhydrophobic surface (described in the next section) the merged droplet bounces three times before it rests on the substrate.

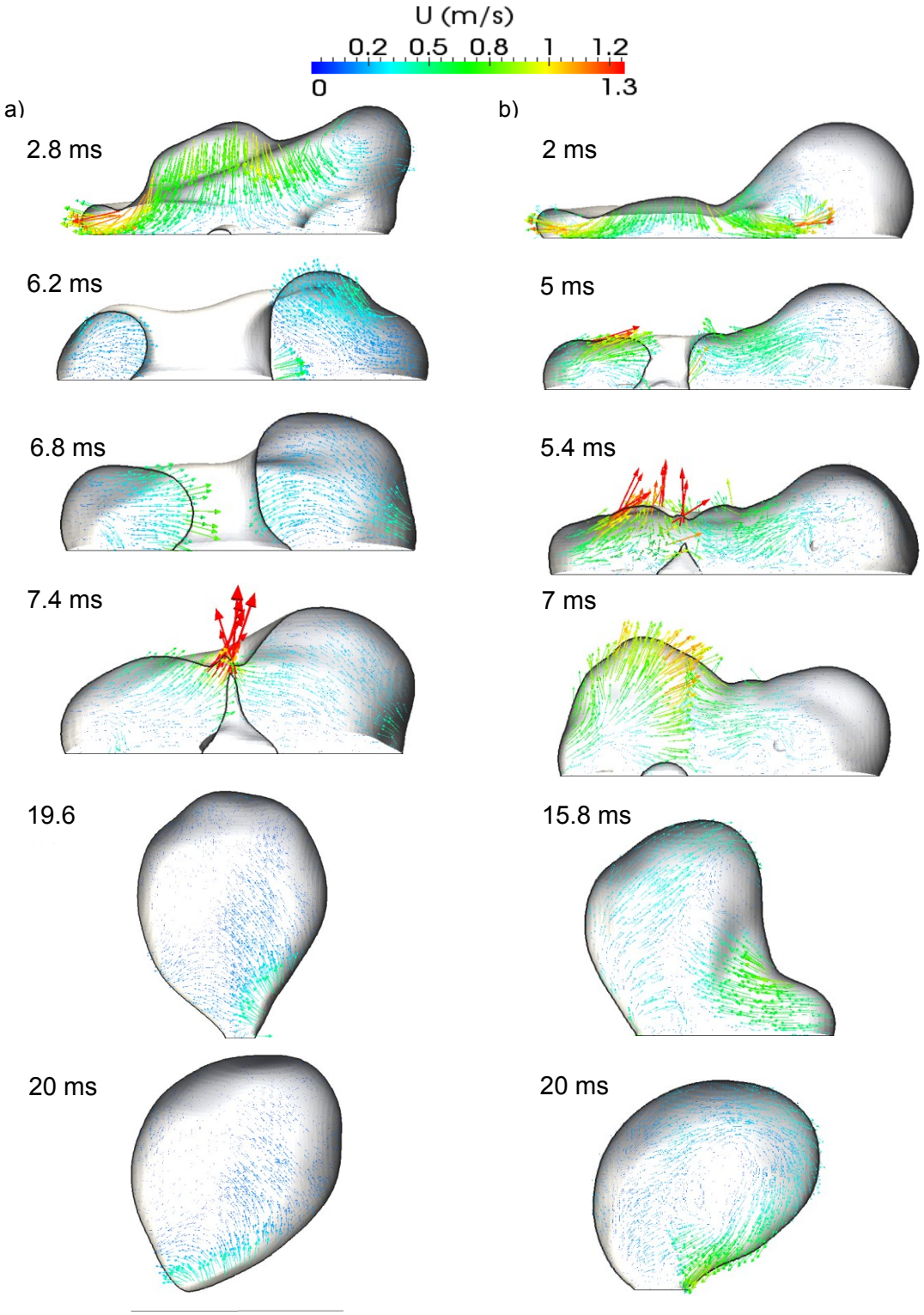

Figure 25: Velocity fields calculated from simulation of the coalescence of two droplets for *We*=28, *Re* =2099, at offset ratios of a) 0.4 and b) 1.1[104].

Figure 25 illustrates the effect of offset on the internal velocity of the droplets. This figure allows understanding the reasons for droplet detachment that usually occurs in near head-on cases, whereas for cases with higher offset ratios, droplet detachment does not occur. It can be seen from both cases, a cavity located at the center of the falling droplet is formed. A comparison of the velocity vectors at the top and the bottom of the cavity indicates that the cavity retracts faster at the top. Consequently, a small part of the air remains trapped inside the cavity during the recoiling process. It can be seen for offset ratio of 0.4 and 1.1 at about 7.4 ms and 5.4 ms respectively, a high speed jet rises (Worthington jet) at the center of the merged droplet, whose velocities are approximately twice the impact velocity of the second droplet.

For the near head-on case, the developed inertia during the recoiling process lifts the merged droplet from the surface at about 20ms. While for the large offset ratio of 1.1, the merged droplet does not detach from the surface. This behavior can be explained by comparing the velocity vectors at the two edges of the merged droplet as shown in Fig. 25 a) and b). In Figure 25a) at around 19 ms, the merged droplet has two dominant velocities, one that is mostly upward and one that is horizontal which is directed towards the impinging droplet (i.e. right to left for this case). While in Figure 25 b) at 15.8ms, for the large offset ratio of 1.1, the largest vectors are located at the right edge of the merged droplet and directed towards the impinging droplet. This causes the top of the droplet to rotate, and consequently displaces its center of gravity. Since the velocity at the right edge of the droplet is not sufficient to overcome the surface energy, the merged droplet falls under the influence of gravity at around 21ms without bouncing off from substrate. In contrast for the smaller offset case, the merged droplet has detached from the surface at around 20 ms.

3.1.3 Superhydrophobic Surfaces

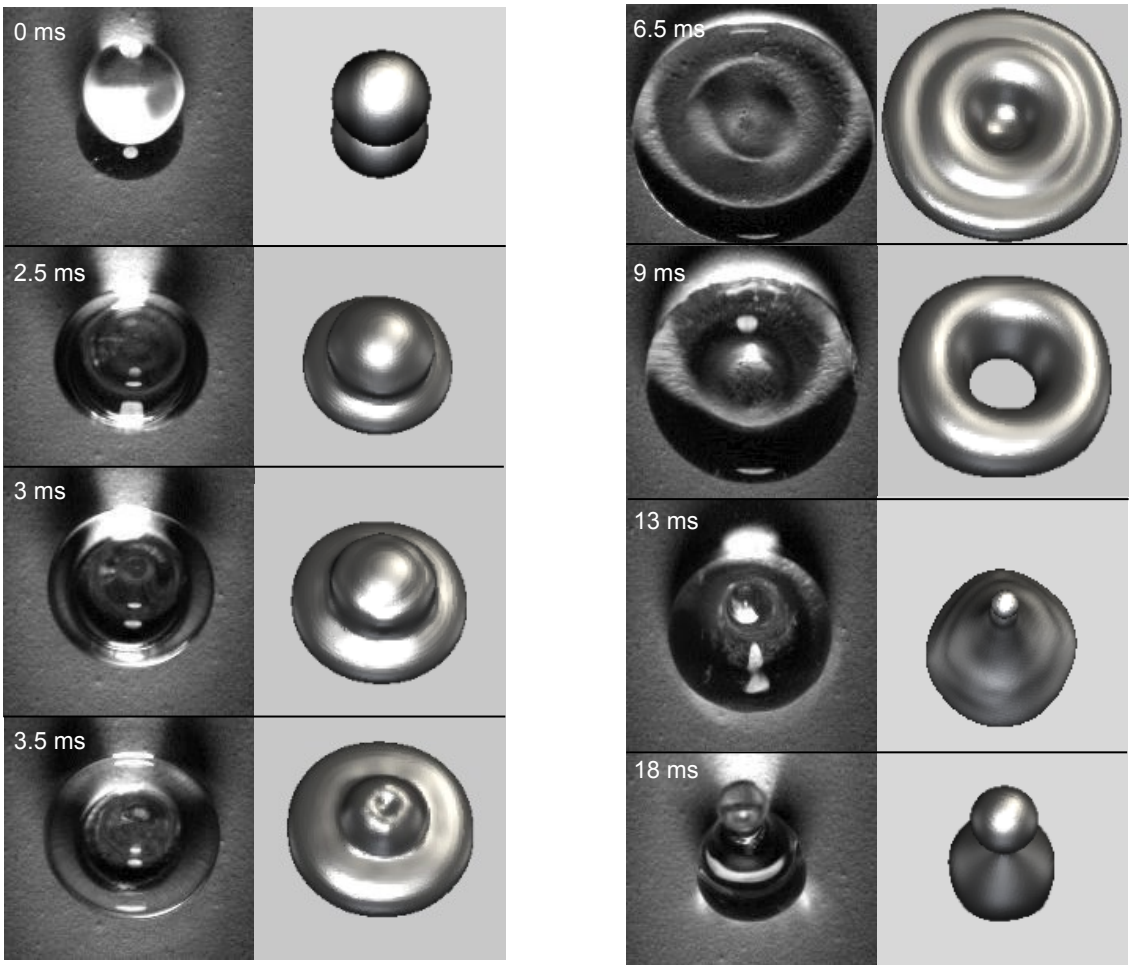

Figure 26: Time evolution of head-on impact and coalescence of two water droplets on a superhydrophobic surface (*We*= 22, *Re* =2020). The experimental images (left side) are compared with simulated images (right side)[51].

Figure 26 shows time evolution images of ahead-on impact and coalescence of the impinging droplet and the sessile droplet. The diameter of each droplet is 2.6 mm, and the impact velocity is 0.774 m/s, resulting *Re*= 2027 and *We* = 19.8. It can be clearly observed from this figure that after the second droplet impacts and merges with the sessile droplet, the fluid spread out horizontally forming a flattened toroidal disk shape at around 9 ms. After the maximum spreading is achieved, surface tension force pulls the two edges back. The motion is radially

inward at around 13 ms after the impact. A jet rises in the center (Worthington jet)[105], caused by the kinetic energy developed during the recoiling process which can lead to a lift off of the whole merged drop.

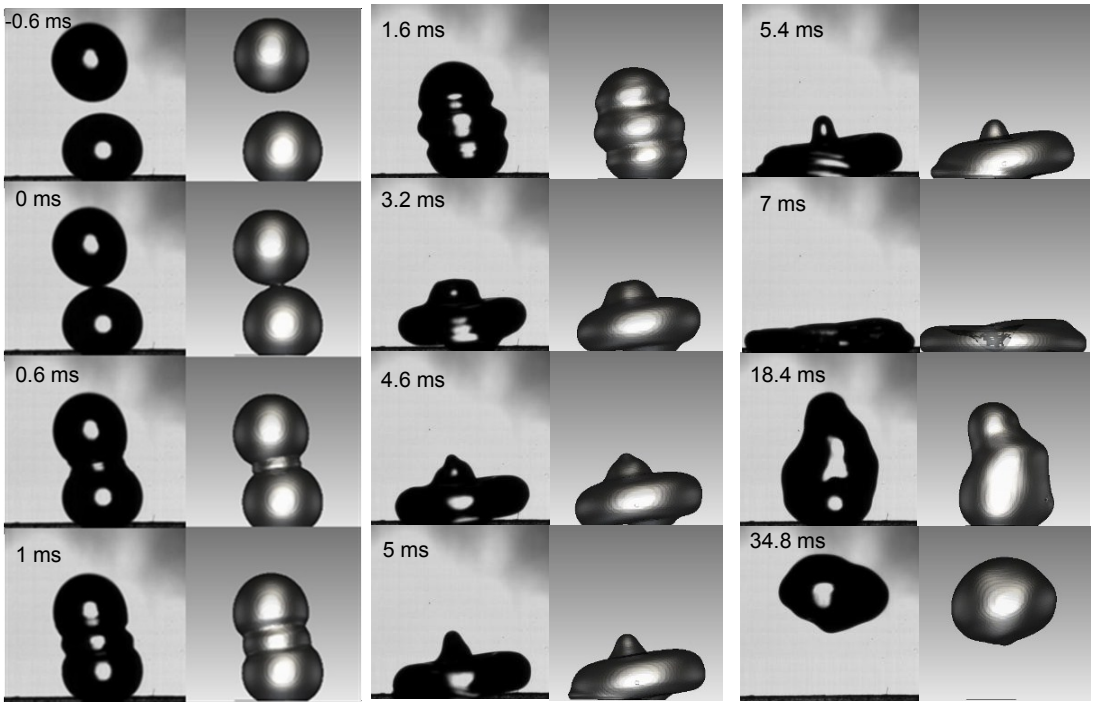

Figure 27: Coalescence of two water droplets on a superhydrophobic surface with a small offset of $\lambda = 0.15$ (We=19.62, Re =2027). The experimental images (left side) compared to calculated images (right side)[51].

Experiments along with numerical simulations were carried out by varying the separation between the sessile and the impacting droplets from the axisymmetric drop-on-drop case up to the point of merging while spreading. The first case presented when studying the effect of offset in a side view of a near head-on collision seen in Figure 27.The diameter of each droplet is 2.6 mm, with Re= 2027 and We =19.62. As shown in Fig. 27 after the impact of the second droplet on the sessile droplet the merged drop spreads out, increasing the surface area of the drop, thus increasing its surface energy. Once the restoring force of surface tension becomes dominant over

the inertial force, at approximately 18ms, the merged droplet recoils. The droplet height rises until it detaches from the surface.

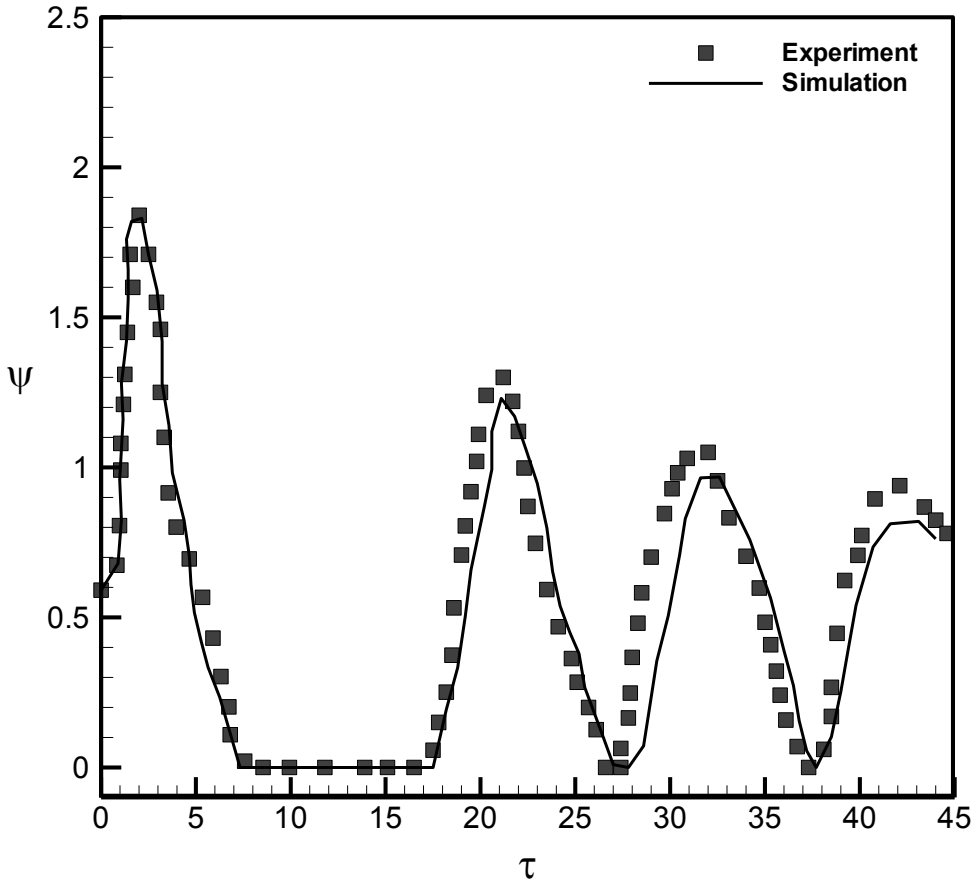

Figure 28: Temporal evolution of dimensionless spread length for droplet coalescence on a superhydrophobic surface (We=19.62, Re =2027, $\lambda = 0.15$)[51].

Figure 28 is served to quantify the spreading and bouncing behavior of a merged droplet by plotting the dimensionless spread length, ψ, versus dimensionless time. Both numerical and experimental results show that after the impinging droplet impacts and merges with the sessile droplet, the spread length increases rapidly until it reaches its maximum value, which is about four times the equilibrium spread length of the sessile droplet. After this point, surface tension forces cause retraction of the contact line until the droplet detaches from the surface. Once the kinetic energy of the detached droplet is converted into potential energy the merged droplet starts

to fall and spreads out on surface. This process continues until the droplet reaches the equilibrium position.

The effect of viscous dissipation on the maximum spreading and bouncing of the droplets can be deduced from Figure 28. A decrease in detached time for successive bounces, which can be attributed to viscous dissipation; thus less mechanical energy in the system was observed. This decreased detached time ultimately translates to the droplet failing to detach from the surface. In addition to the decrease in detached time, the maximum spreading also decreases with successive bounces. These two trends can be simultaneously explained through the analogy of damped harmonic motion where potential energy is transferred from surface energy to gravitational potential energy. As time progresses, energy is dissipated causing the droplet to have less surface energy expressed as the wetting length, and less gravitational energy expressed as a shorter detached time. After multiple bounces the discrepancy between experimental and numerical results begins to increase, likely due to accumulated error from inhomogeneity in the surface. To understand the mechanism of droplet merging and bouncing, the surface and kinetic energy are calculated at various stages.

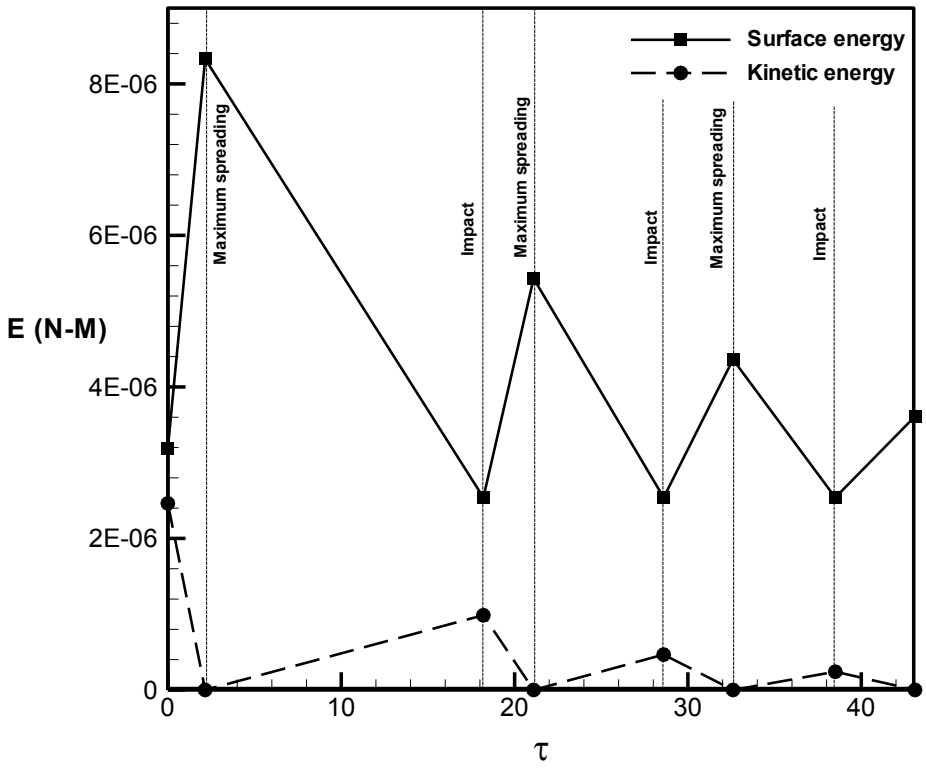

Figure 29: Variation of surface and kinetic energy of the merged droplet during bouncing on superhydrophobic surface (We=19.62, Re =2027, $\lambda = 0.15$)[51].

Patankar[21] described the stable surface free energy, G_s, of a sessile droplet in contact with a textured surface as

$$\frac{G_s}{\sqrt[3]{9\pi}V^{2/3}\gamma} = (1-\cos\theta_e)^{2/3}(2+\cos\theta_e)^{1/3} \tag{22}$$

Before impact, the kinetic energy KE_1, and surface energy $SE_1$of a spherical droplet are given by

$$KE_1 = \left(\frac{1}{2}\rho U_0^2\right)\left(\frac{\pi}{6}D_0^3\right) \tag{23}$$

$$SE_1 = \pi D_0^2\gamma \tag{24}$$

Therefore, the total surface energy of the sessile and the impacting droplet can be calculated by

$$SE_1 = SE_I + G_s \tag{25}$$

After impact, when the merged droplet is at its maximum extension diameter D_{max}, the kinetic energy is zero and the surface energy SE_2 is[36]

$$SE_2 = \frac{\pi}{4} D_{\max}^2 \gamma (1 - \cos\theta_A) \tag{26}$$

The calculated variation of the surface energy and kinetic energy of the merged droplet at the moment of droplet impact and maximum spreading on superhydrophobic surface is shown together in Fig. 29.This figure shows that kinetic and surface energy were interchanging between each other and loss of energy occurs through viscous dissipation.

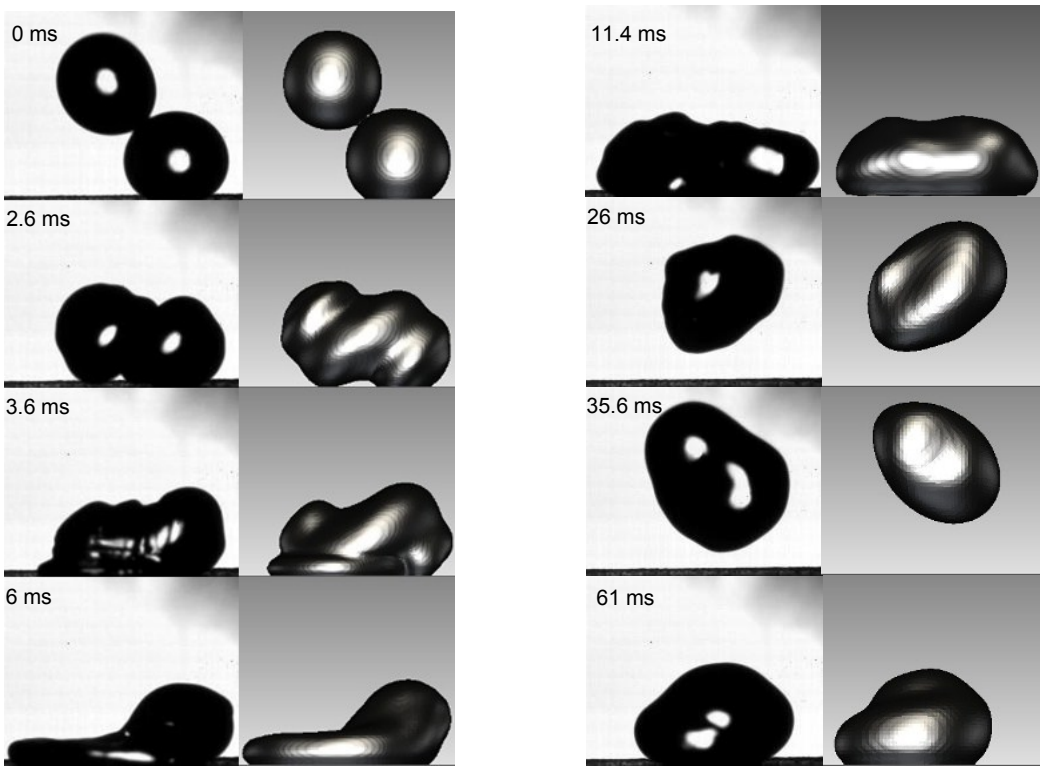

Figure 30: Coalescence of two water droplets on a superhydrophobic surface at a moderate offset of λ = 0.65 (*We*=19.62, *Re* =2027). The experimental images (left side) compared to simulated images (right side)[51].

The evolution of the free surface for a moderate spacing of 0.65 is shown in Figure 30. The diameter of each droplet is 2.55 mm, and the impact velocity is 0.757 m/s, giving *Re*= 2027 and *We* = 19.62. In the figure, the shape evolution of the two droplets during the coalescence phenomena from simulation is shown together with the images of the experimentally observed drop shapes. As seen from Figure 30, the impinging droplet lands partially on the sessile droplet and partially on a dry surface at 2.6ms. After merging with the sessile droplet, the inertia of the second droplet causes the merged drop to deform and spread. After reaching the maximum spread diameter (at 6ms), surface forces acting on the drop reduce the surface area of the merged drop. Developed inertia during the recoiling process lifts the merged drop from the surface at about 26ms. Figure 30 shows the merged droplet rotates in air between 26ms and 35.6ms after bouncing.

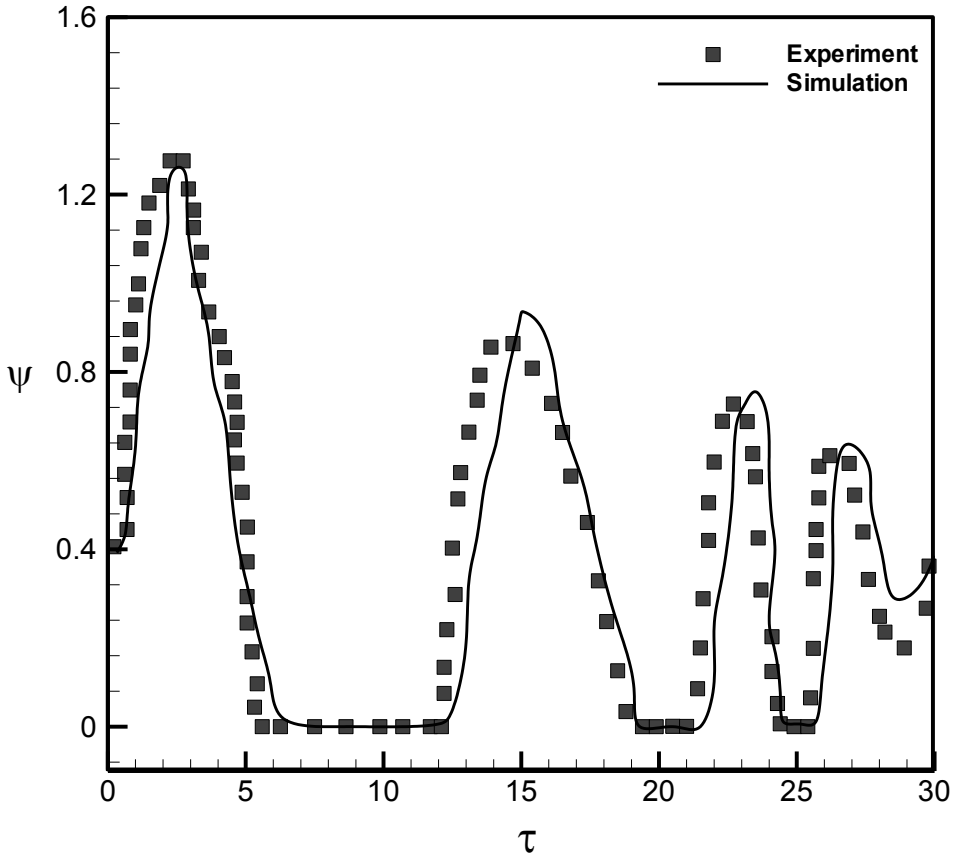

Figure 31: Temporal evolution of dimensionless spread length for droplet coalescence on a superhydrophobic surface at a moderate offset of $\lambda = 0.65$ (We=19.62, Re =2027)[51].

Figure 31 shows the comparison of simulated results with experiments for the evolution of dimensionless spread length versus dimensionless time. It can be observed from the figure that the hanging time for the merged drop after bounce off from surface for the first impact is much longer than the second and third ones, which indicates a large amount of dissipation during the detached time and subsequent impact. The deviation of the simulation results from experiments magnifies after the second impact.

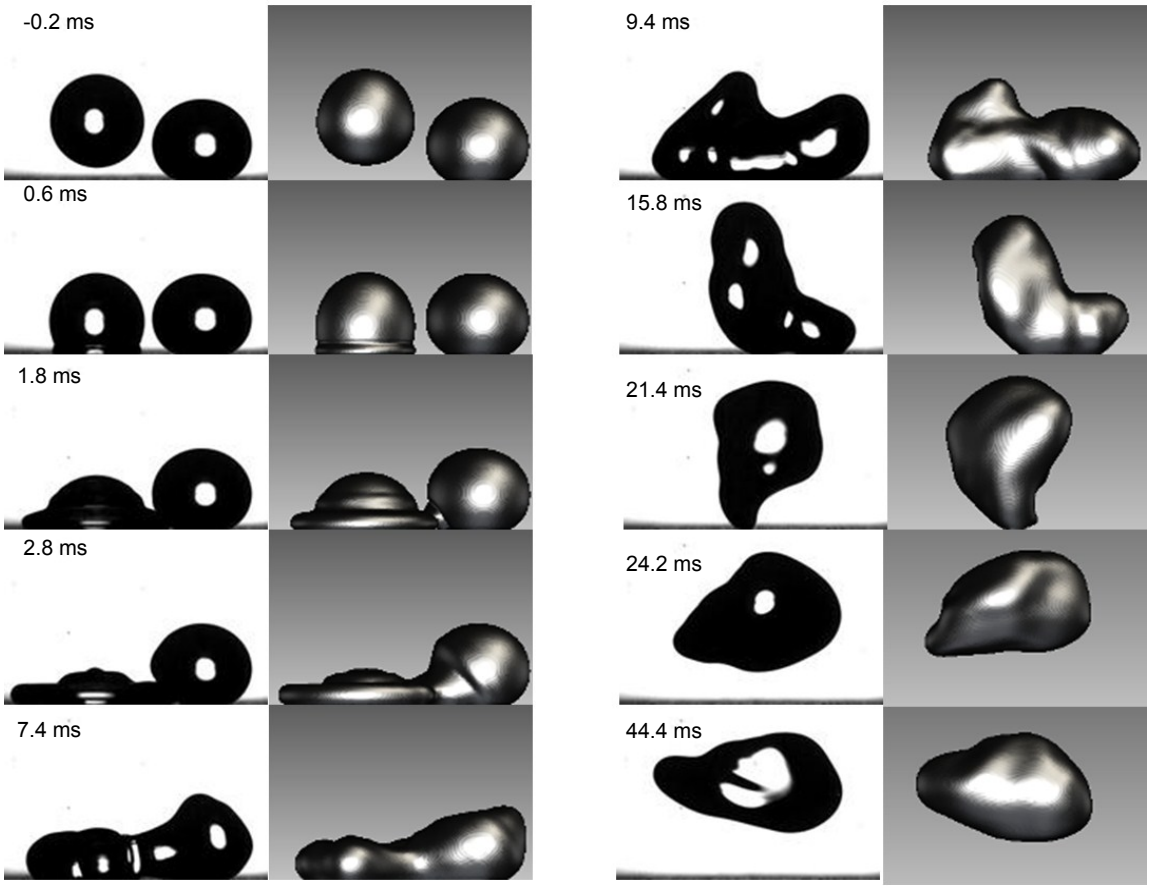

Figure 32: Coalescence of two water droplets on a superhydrophobic surface at a large offset of λ = 1.10 (*We*=21.8, *Re* =1977). The experimental images (left side) compared to the simulated images (right side)[51].

Simulated results of the coalescence of two droplets at a large offset are compared with the experimental images in Figure 32. The diameter of each droplet is 2.6 mm, and the impact velocity is 0.786 m/s, giving *Re*=1977 and *We* = 21.8 at an overlap ratio of 1.1. As shown in Figure 32, droplet impinges on the dry section of the surface. Then the inertia causes the droplet to spread out and during the spreading the impinging droplet merges with the sessile droplet. Afterward the kinetic energy of the merged droplet is converted into surface energy, which will be used for the retraction and rebound of the merged drop. Figure 32 shows that the merged droplet rotates in the air after bouncing-off (between 24.2ms- 44.4ms).

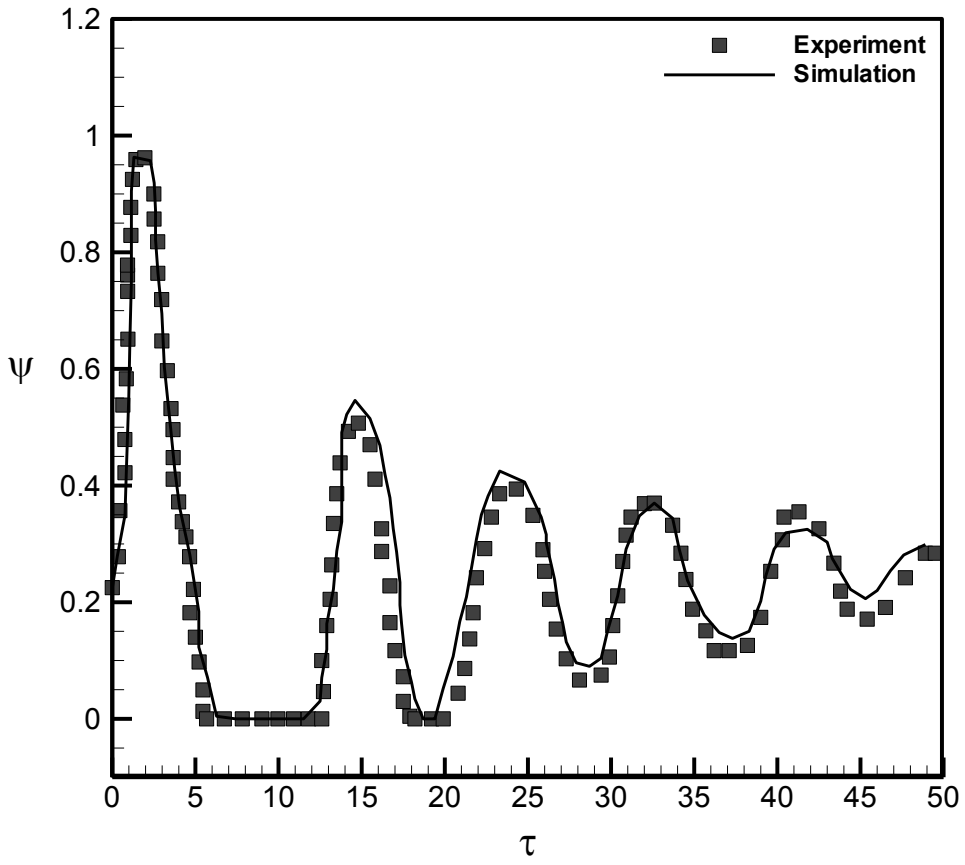

Figure 33: Temporal evolution of dimensionless spread length for droplet coalescence on a superhydrophobic surface (We=21.8, Re =1977, λ = 1.10)[51].

As spacing increases, the merging process imposes more viscous dissipation. Figure 33 displays the comparison of the simulated results with the experiments for the evolution of dimensionless spread length versus time. The maximum spread diameter decreased abruptly with successive bounces as compared to the results of Figure 33, which has moderate overlap ratio. It has been observed that by increasing the overlap ratio the number of detachments of the droplet from surface decreased. This would imply more viscous dissipation while the droplet is detached from the surface. The surface energy released upon coalescence of two drops can be as high as 20% of the original energy.

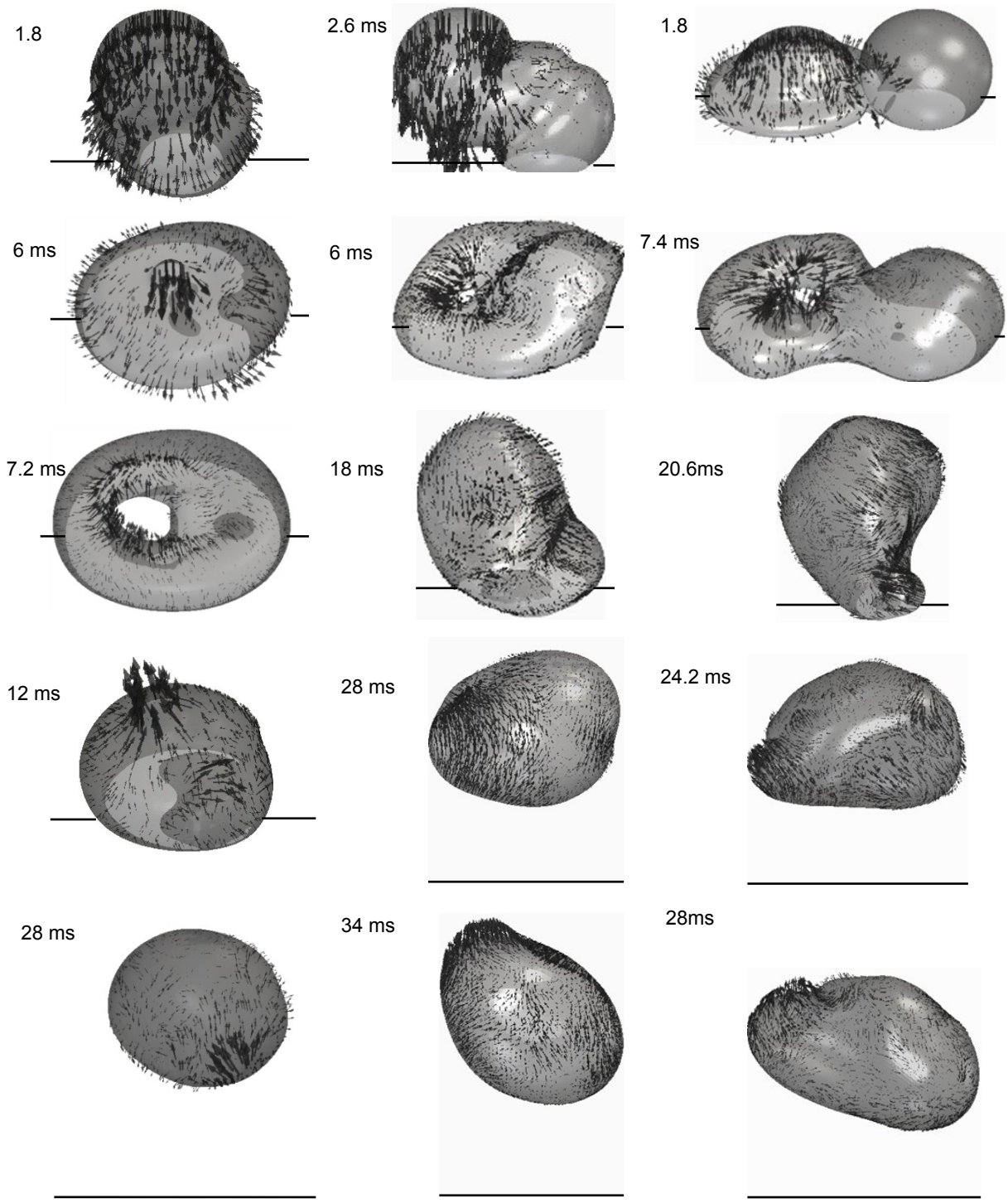

Figure 34: Velocity fields calculated from simulation of the coalescence of two droplets for *We*=19.62, *Re* =2027, at overlap ratios of (a) 0.15 (b) 0.65 (c) 1.1[51].

Figure 34 illustrates the effect of offset on the internal velocity of the droplets in order to understand the rotational behavior of the detached droplet. The largest vector size in each case corresponds to the velocities of $0.6ms^{-1}$, $0.5ms^{-1}$ and$0.5ms^{-1}$, respectively. For the near head-on offset, a cavity at the center of the droplets was formed and the merged droplet took a toroidal shape at 7.2ms. The droplet begins to detach at about 12ms. During detachment, the largest velocities are upward and at the center of the droplet. At a moderate overlap ratio of 0.65, the droplet begins to detach at around 18ms; in contrast to the near head-on case which has its largest velocity at its center and in an upward direction, the moderate overlap ratio has two dominant velocities, one mostly upward and one parallel to the surface and towards the impinging droplet, which causes the rotation of the merged droplet after detachment. At a large overlap ratio of 1.1, more rotation is observed, which is consistent with the greater horizontal velocity of the base of the droplet during detachment. It is important to note that the delay in change of velocity of the sessile droplet increases with increasing offset, this increase in delay is seen when comparing the large offset at 7.4ms to the moderate offset at 6ms; furthermore, no delay is observed for the near head-on scenario. The horizontal velocity component of the base of the droplet increases with increasing offset because the sessile droplet only begins to flow in the later stages of detachment.

The contact time and restitution coefficient are two crucial parameters for droplet-surface interaction. The contact time is the time that the merged droplet is in contact with the surface before detaching and the restitution coefficient, ε, is the ratio of impact velocity to the rebound velocity of the merged droplet. In this section, the effects of impact velocity, droplet sizes and droplet separation on these two parameters are investigated both numerically and experimentally.

Our investigation may help measuring the efficiency of water repellent (superhydrophobic) surfaces, and improving the cooling of hot solids, for which drop rebounds are a severe limit.

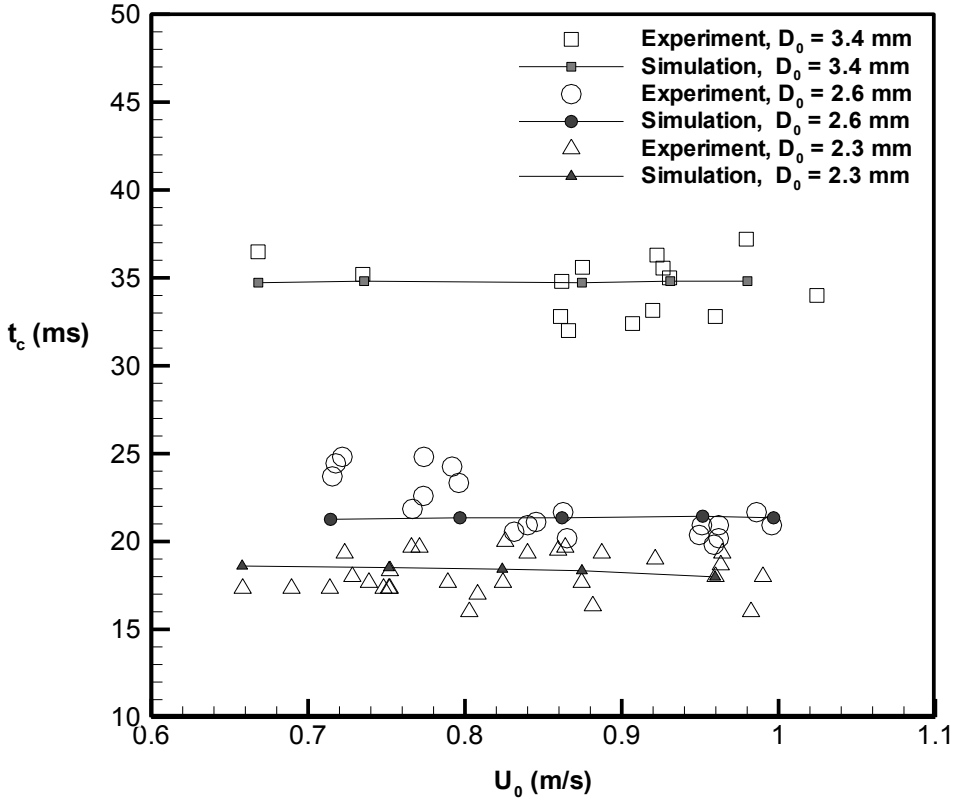

Figure 35: Contact time versus impact velocity for different droplet sizes[51].

The effect of impact velocity and droplet diameter on contact time for head-on collisions is shown in Fig. 35. As seen in this figure, the contact time is found to be independent of the impact velocity in a within range studied; however, it largely depends on droplet diameter. This is similar to a harmonic spring, where the natural frequency of the droplet depends on its size and surface tension and not any initial conditions imposed on it.

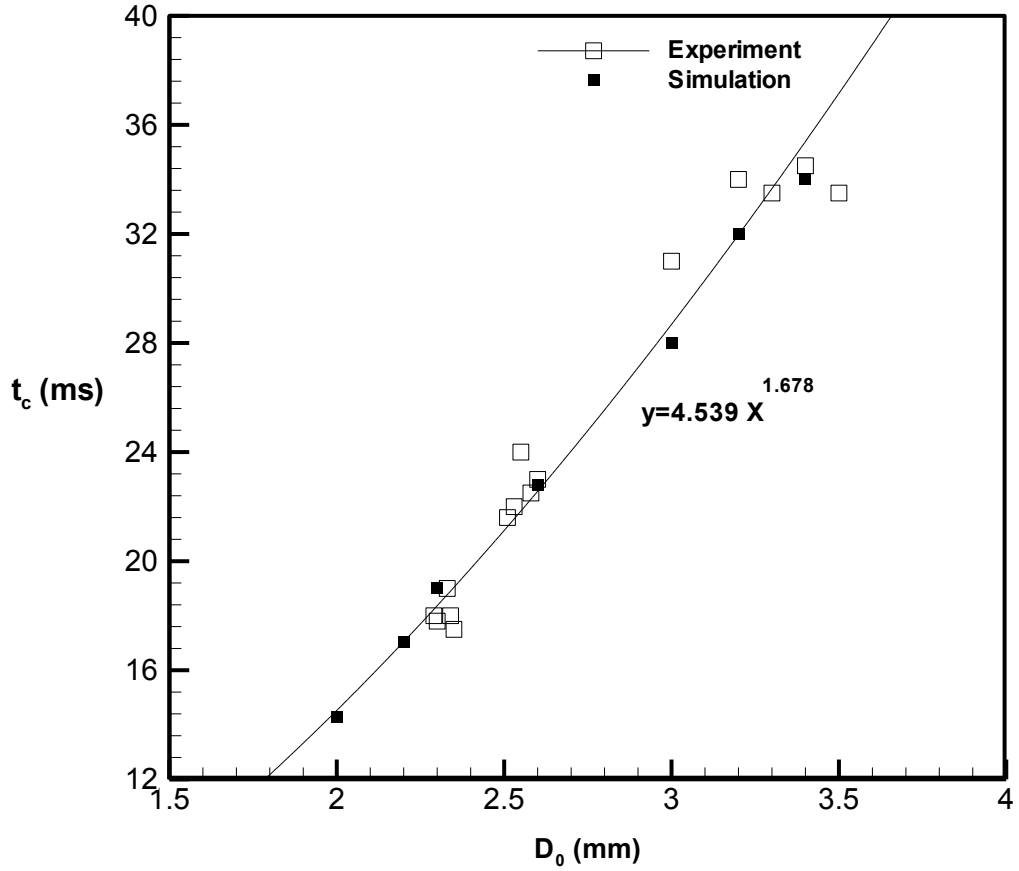

Figure 36: Contact time versus droplet diameter[51].

Figure 36 shows the effect of droplet diameter on the contact time of head-on coalescence of two droplets on the superhydrophobic surface. As it can be observed from this figure, upon taking a power regression to the data, it was determined that the least-squares fit had an exponent of 1.678, which compares well to the work of Richard et al.[34] who developed a model by balancing inertia (of order $\rho R/t_c^2$) with capillarity (γ/R^2), which yields $t_c \sim (\rho R^3/\gamma)^{1/2}$. Uncertainty in the measurement of droplet size is based on the standard deviation of droplets; while the temporal uncertainty is based on the recording rate of the camera. The resulting power law relating the diameter of the drop to its contact time, given by $t_c \propto D_0^{1.5}$.

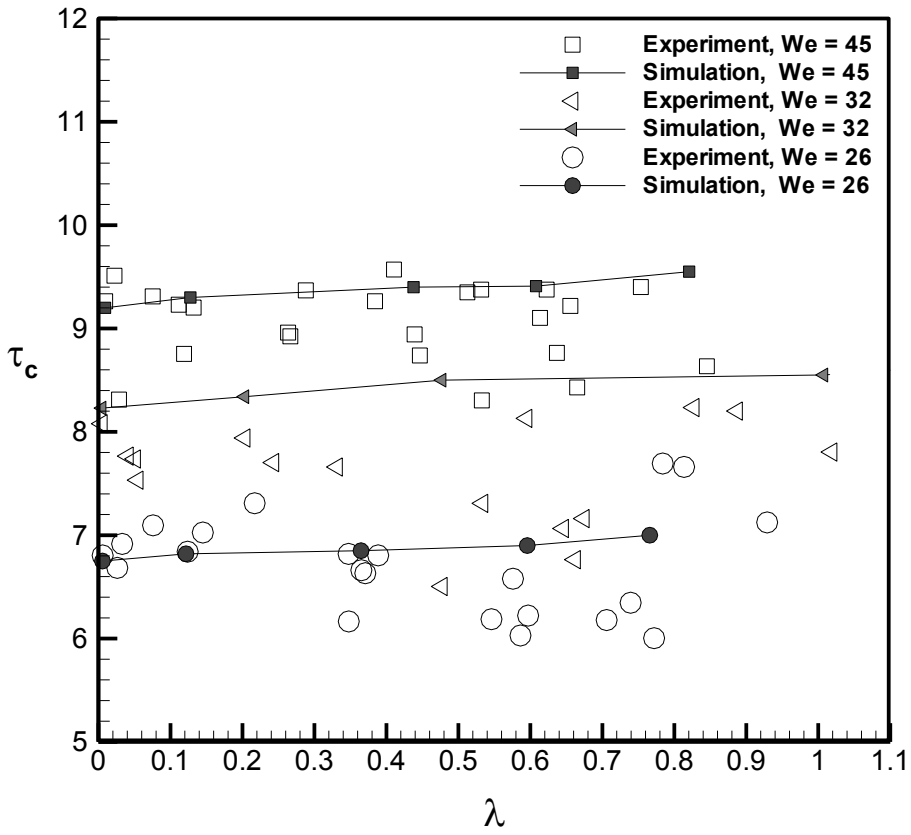

Figure 37: The dimensionless contact time with varied overlaps and impact velocity[51].

The dimensionless contact time of the merged droplets as a function of overlap ratio are displayed for different Weber number in Figure 37. As can be seen from this figure, by increasing the separation between the centers of the droplets, the dimensionless contact time remains almost constant. While increasing the weber number increases the contact time.

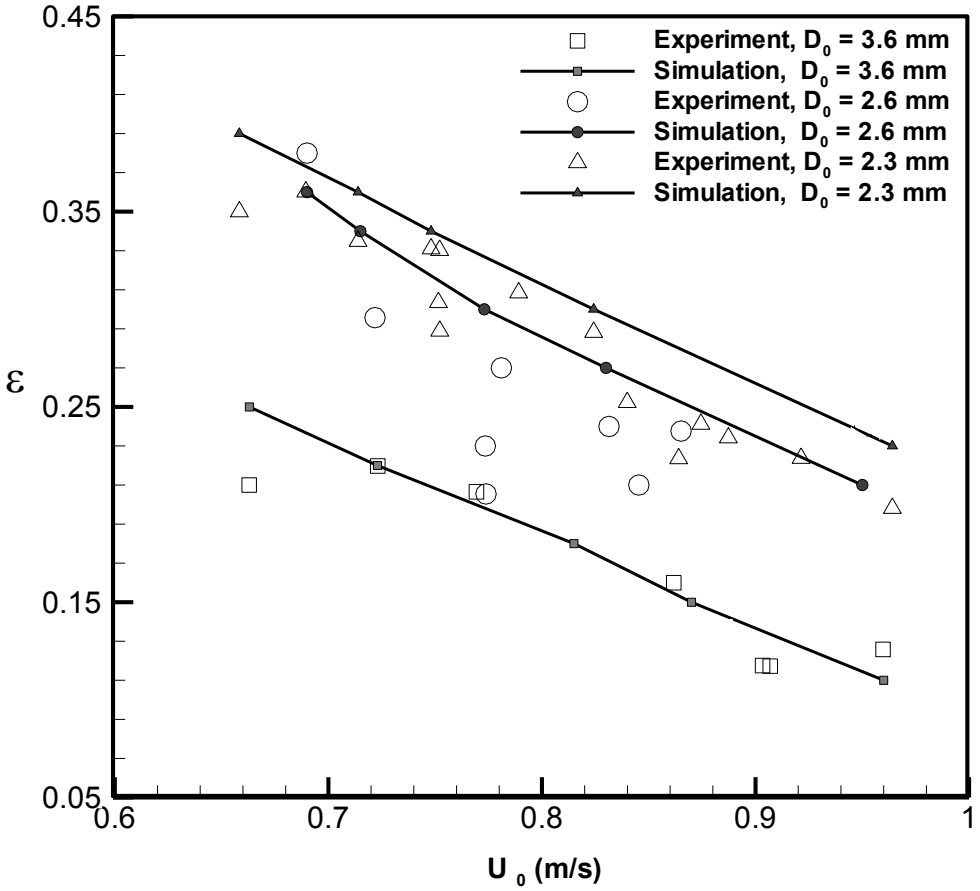

Figure 38: Restitution coefficient ε, for head-on coalescence as a function of impact velocity $U_{0,}$ for different droplet sizes[51].

The restitution coefficient, ε, is the ratio of the impact velocity $U_{0,}$ to the rebound velocity of the droplet. Considering the final droplet volume is twice the impacting droplet volume, the ideal value of the restitution coefficient is 0.5. The restitution coefficient for the studied superhydrophobic surface for head-on impact is plotted as a function of impact velocity for different droplet sizes. As shown in Figure 38, the restitution coefficient decreases for both increasing size and impact velocity due to an increase in energy dissipation. An increase in energy dissipation is due to either an increase in the deformation of the merged droplets, such as droplet elongation, or oscillation of the detached droplet. It was difficult to obtain accurate

experimental results for the coefficient of restitution, since inferring a three dimensional geometry based on the two dimensional profile has some inaccuracies. However, a good qualitative agreement is observed between predictions from the numerical model and measurements from the experiments.

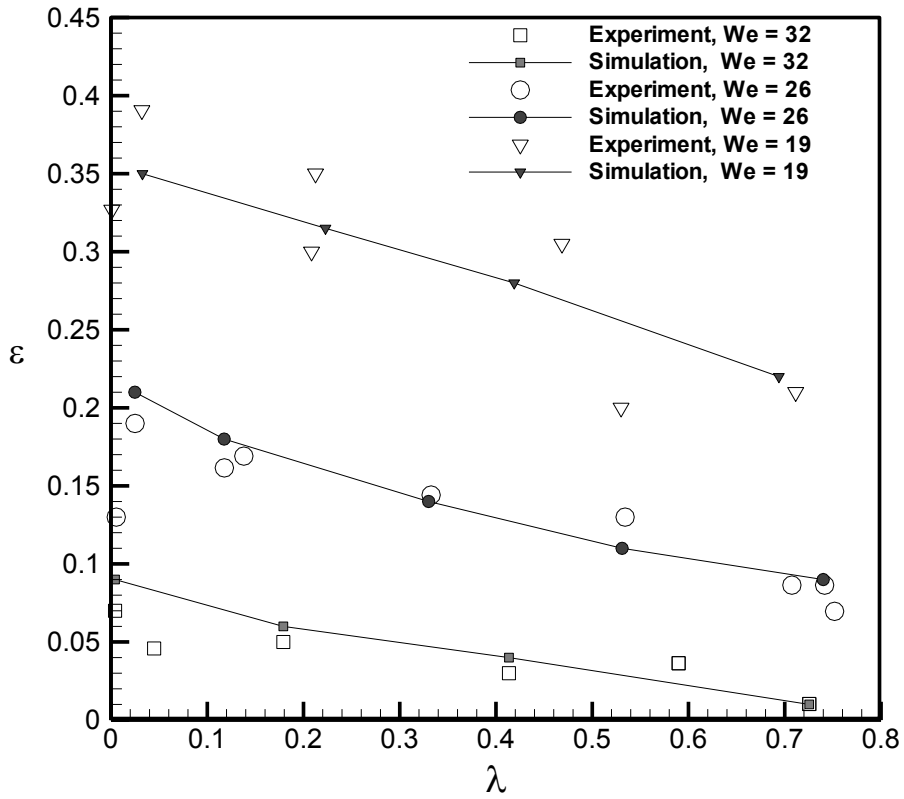

Figure 39: Restitution coefficient ε, as a function of overlap ratio λ for different Weber numbers[51].

Figure 39 illustrates the effect of overlap ratio on the restitution coefficient for the studied superhydrophobic surface for different Weber numbers. As seen from the figure, increasing the overlap ratio decreases the restitution coefficient. Moreover, the figure displays that increasing the weber number decreases the restitution coefficient. This can be attributed to two effects, and increase in dissipation within the droplet and an increase in the rotational momentum at the expense of translation momentum. At larger spacing a larger moment is imposed on the droplet system due to a greater moment arm caused by the spacing.

3.1.4 Comparison of Surface Wettability

It is crucial for most engineering applications that are based on controlled deposition of droplets, to know the maximum spreading lengths. Therefore, it is useful to study the effect of different parameters on the maximum spreading length of coalescing droplets. In this section, the effect of various parameters on the droplet spreading length, such as droplet size, impinging velocity, offset ratio, and surface wettabilities is investigated.

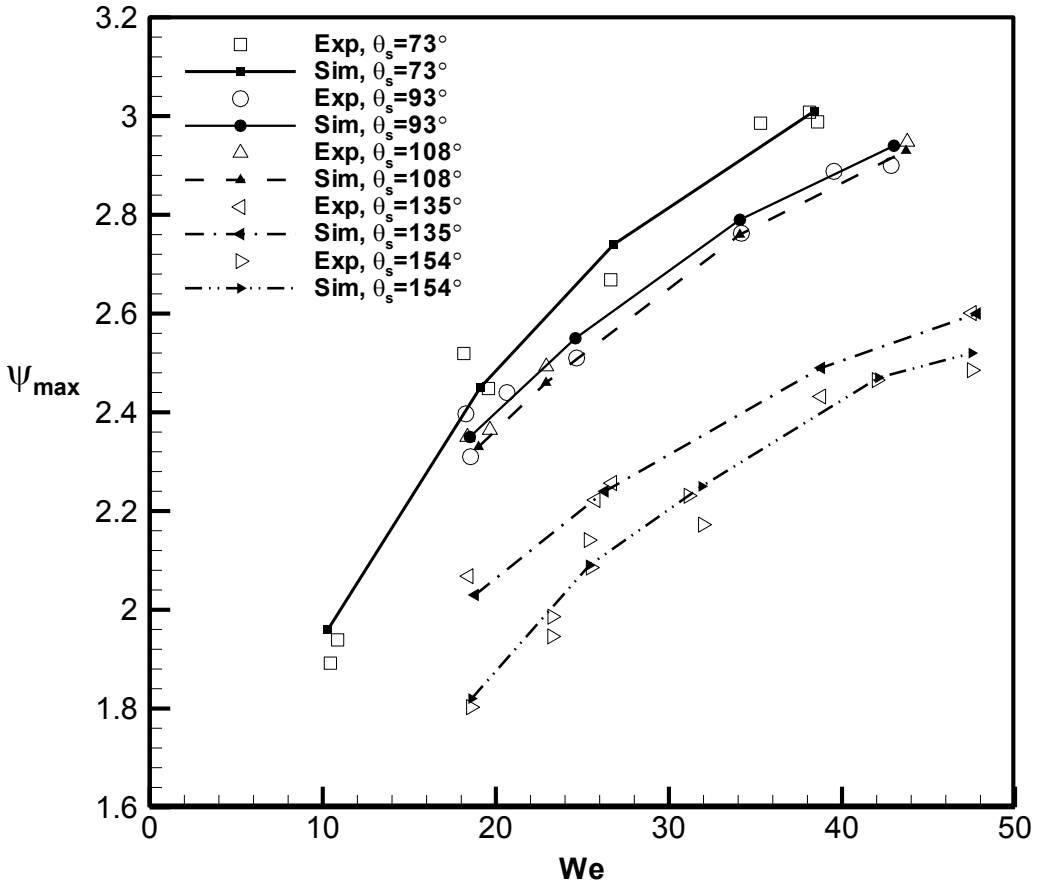

Figure 40: The maximum dimensionless spreading length as a function of Weber number for head-on impact (λ=0)[104].

Figure 40 displays the maximum spreading length ($\psi_{max}=D_{ymax}/D_0+L$) as function of Weber number for various surface wettabilities under the head-on impact condition (i.e. L=0). This figure indicates that the maximum spreading length decreases with increasing hydrophobicity of the surface and increases with increasing Weber number. However, it is worth mentioning that the experiments reported here consider rather low impact velocities, for which the effects of wettability may be more noticeable. The effect of surface wettability on the droplet coalescence at high Weber numbers requires further study and investigations. For a single droplet impact, Pasandideh-Fard et al. [36]showed that the effect of surface wettability on maximum spreading length may eventually become negligible for high Weber numbers. This may be applicable to the coalescence phenomena, particularly at large offsets between droplets at much higher weber numbers.

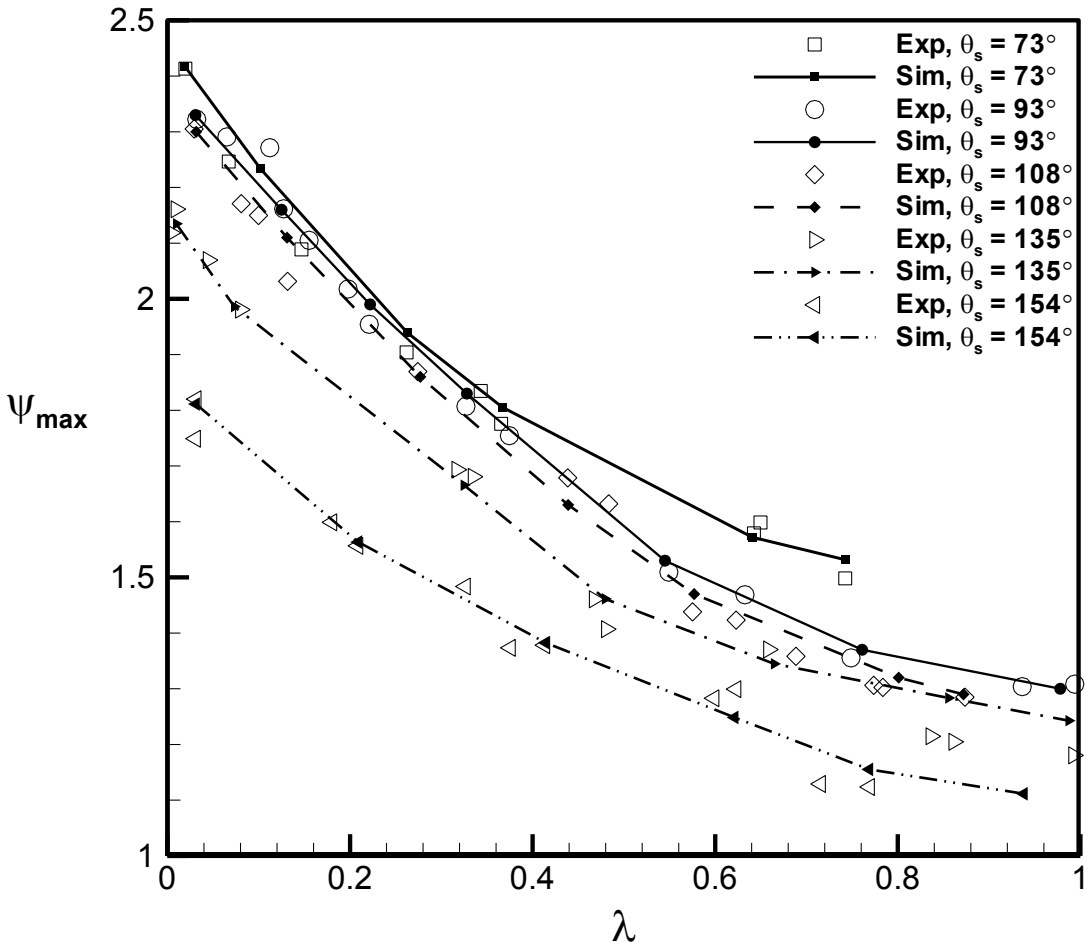

Figure 41: The maximum spreading length as a function of offset ratio for We ≈ 20[104].

Figure 41 shows the effect of offset ratio on maximum spreading length for surface with various wettabilities. As seen from this figure, the maximum spreading length, $\psi_{max,}$ decreases by increasing the offset ratio and surface hydrophobicity. At large offset cases, surface wettability has two effects: it impedes the spreading of the droplet prior to merging and impedes the spreading of the droplets once they merged. In contrast small offsets merge then spread, so wettability only comes into play on the later stage.

A regression analysis is performed to unify the effect of droplet inertia, liquid surface tension, droplet offset and substrate wettability. The maximum spreading length for each droplet

size, impinging velocity, spacing and surface is summarized with one empirical correlation. In order to unify the effect of all five surfaces (from hydrophilic to superhydrophobic) a new weber number is defined as the ratio between droplet inertia and liquid solid interfacial energy, simply put is the ratio between incoming energy and the ability of the surface to store energy. It is defined based on the works of Chibowski,[106]who defined the solid-liquid surface energy based on the contact angle hysteresis. The relation between solid liquid interfacial energy and liquid vapor interfacial energy is shown in equation 27, and the "surface Weber number" is described in equation 28. Performing a least squared fitting of the natural logarithms of ψ_{max}, L/D_0 and We_{sl}, as done in the works of Li et al.[48], yields the expression seen in equation 29. The correlation coefficient is 0.8795, which indicates a coherent trend. In contrast to the work of Li et al. [48] this work did not study different liquids, only the inertia was varied for different offsets and surfaces; therefore, it would be misleading to include either Ohnesorge number or Reynolds number, since those numbers include the effect of viscosity. The resulting regression model is compared graphically to experimental and numerical results in Figure 42. Regression models for each individual surface are included in the Appendix.

$$\frac{\gamma_{sl}}{\gamma_{lv}} = \frac{1+\cos^2\theta_A}{2+\cos\theta_R+\cos\theta_A} - \cos\theta_A \tag{27}$$

$$We_{sl} = \frac{\rho U^2 D}{\gamma_{sl}} \tag{28}$$

$$\psi_{max} = 0.9759\left(1+\frac{L}{D_0}\right)^{-0.7594} We_{sl}^{\,0.2283}\ ,\ R^2 = 0.8795 \tag{29}$$

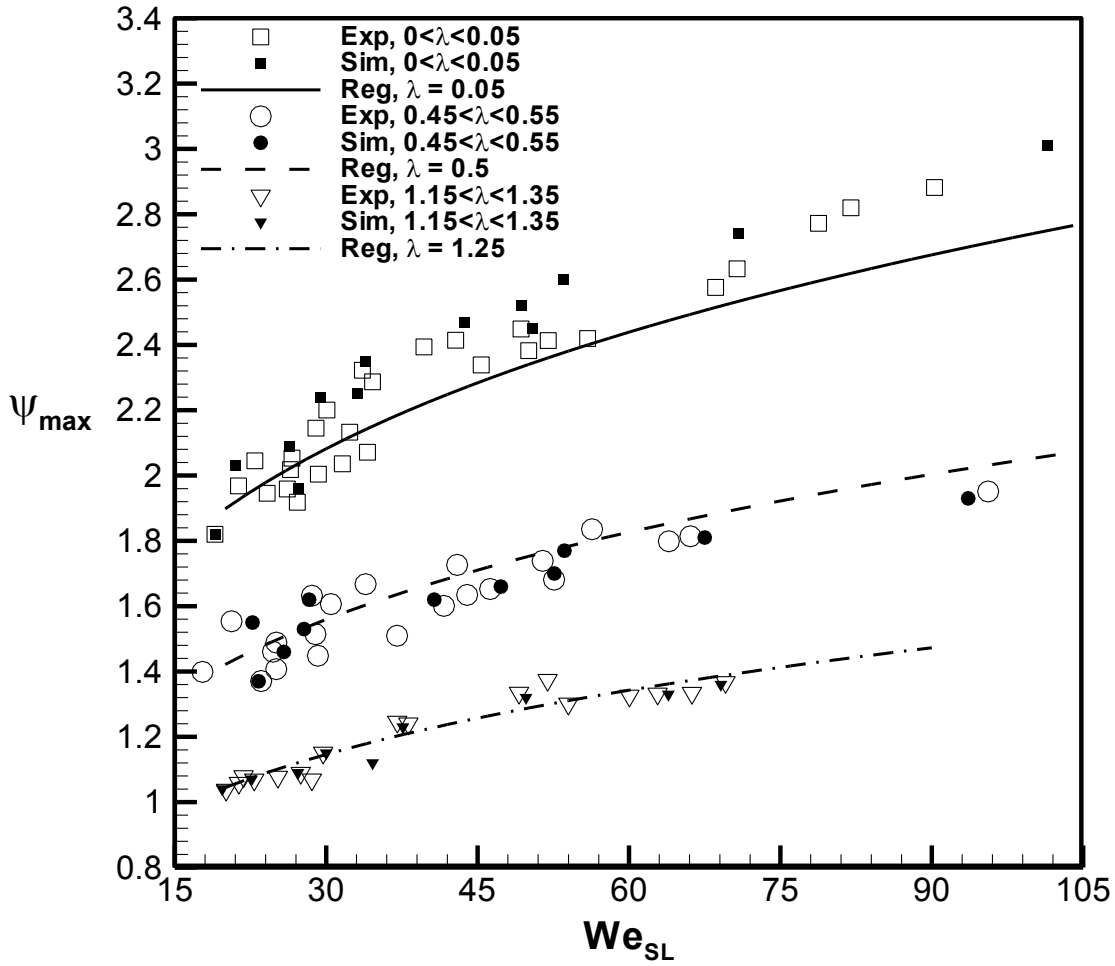

Figure 42: Comparison between experimental, correlation 29, and computed maximum spreading lengths of the merged droplet as function of surface Weber number for different offset ratio[104].

The comparison between the experimental and computed maximum spreading length of merged droplet on various surfaces with different offset ratios is shown together with the results of correlation 29 in Fig. 42. It can be seen that regression model could predict well the maximum spreading length of the merged droplet for different offset ratio.

3.2 Droplet Shedding

As a first step the model was subjected to several tests in order to validate its results. The first case considered was that of shedding tests for a range of drop volumes of water on superhydrophobic, Teflon and PMMA surfaces, which experimental results are available in terms of critical air velocity against drops volume. The results of the numerical model are compared with the measurements of experiments performed by Milne and Amirfazli[7] in Fig. 43. In this test, after the droplet rests on 10 cm downstream from the leading edge of the streamline body, the air velocity was increased relatively uniformly until the moment that droplet starts to move.

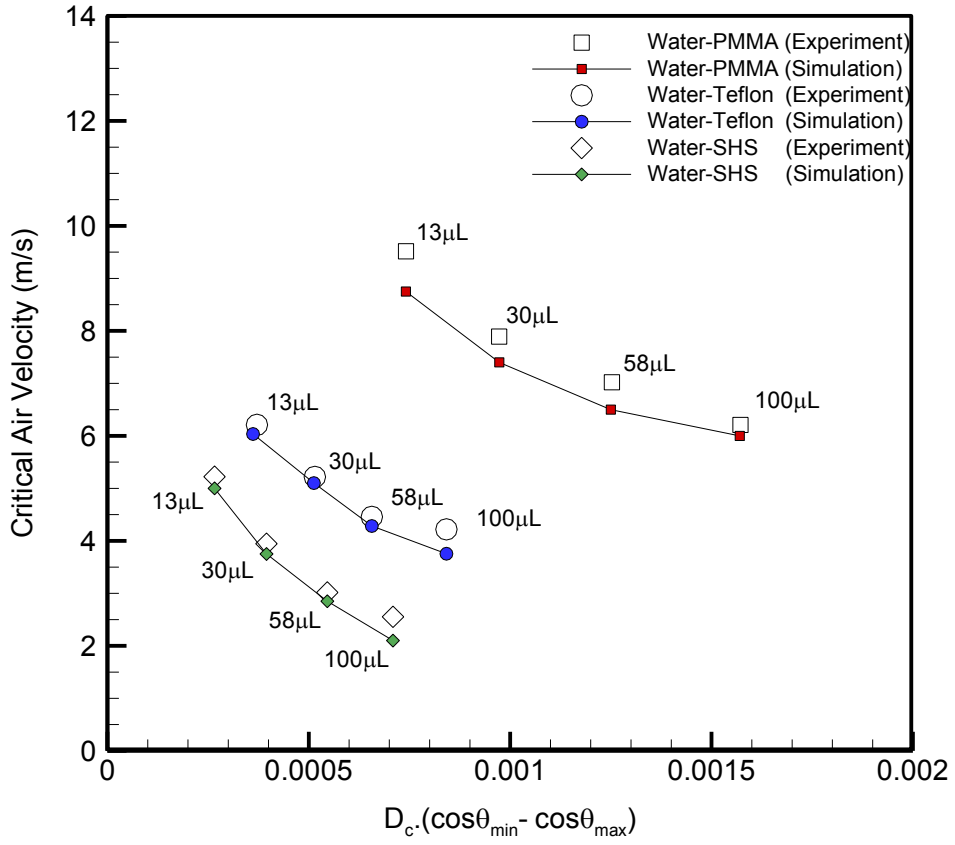

Figure 43: Critical air velocity for incipient motion versus a measue of drop adhesion (D_c $(cos\theta_{min}\text{-}cos\theta_{max})$)

The critical air velocity for incipient motion was defined as the air velocity measured when both the upstream and downstream contact points had moved $210\mu m$ distance downstream. This threshold is introduced by Miline and Amirfazli[7]. Figure 43 shows that the critical air velocity for incipient motion of droplet decreases by increasing the size of droplet. By comparing the three different systems in Fig. 43, it can be seen that for each volume as $D_c\ (cos\theta_{min}\text{-}cos\theta_{max})$ decreases, the critical air velocity for drop shedding is also decreased. The reduction in drop adhesion across the three systems leads to decrease in $D_c\ (cos\theta_{min}\text{-}cos\theta_{max})$. This behavior indicates that systems with greater mobility (lower adhesion) shed drops more easily.

It is worth mentioning that the repellency of the surfaces in the case of drop shedding by air flow is not associated by high contact angle hysteresis ($CAH=\theta_A\text{-}\theta_R$). It can be seen from both numerical and experimental results for water –SHS, which has the high CAH, the critical air velocity for runback is the lowest. This is due to the increased area (increasing drag) and decreased D_c (in principle, decreasing adhesion) of the water drops on the SHS. Therefore, the parameter $D_c\ (cos\theta_{min}\text{-}cos\theta_{max})$ is the best readily accessible measure of ease of shedding. Considering the parameter $D_c\ (cos\theta_{min}\text{-}cos\theta_{max})$ in which the contact length (D_c) is itself a function of contact angle and volume, It can be concluded that the wetting and adhesion characteristics of a system have major roles in the shedding of droplets by shearflow.

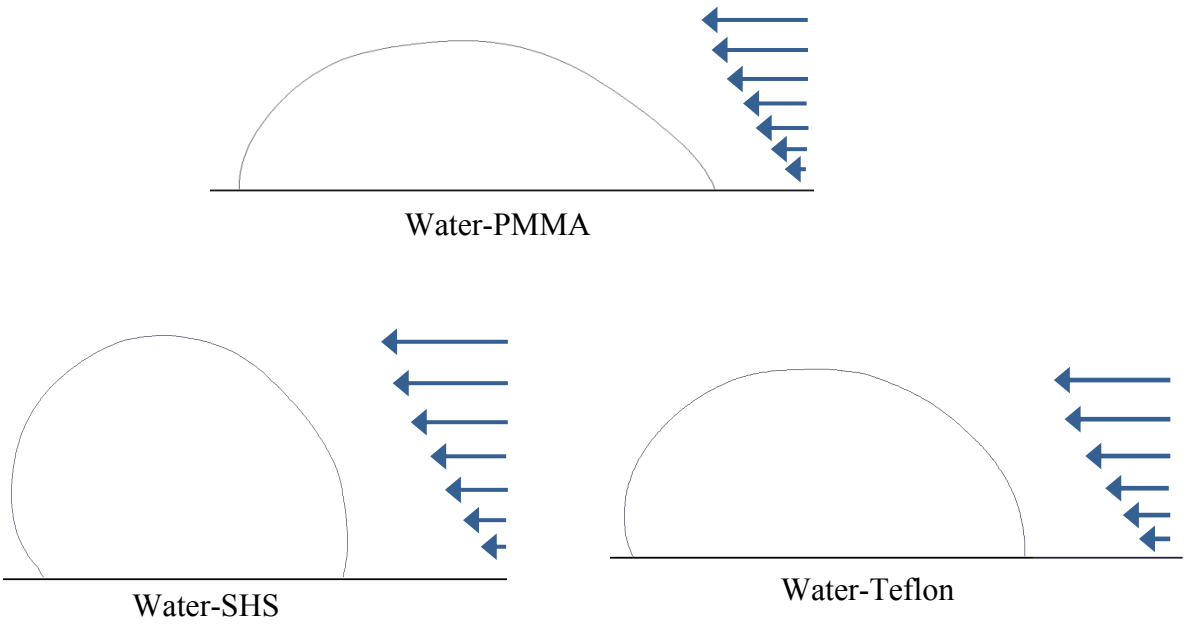

Figure 44: Shapes of the drop cross-section on various surfaces at the symmetry plane for maximum hysteresis.

Figure 44 shows the shapes of cross section of 100μL water droplet on three different surfaces at maximum contact angle hysteresis due to the shear flow. This figure shows clearly the different CAH between three systems and also supports the fact that water droplets on SHS has greater area (increasing drag) and lower D_c (decreasing adhesion) comparing to the same size of droplet on Teflon or PMMA. Consequently, it can shed the droplet easily comparing to the other surfaces.

The comparison of contact line shapes for sessile droplet on PMMA surface at initial state and critical state (incipient motion) are shown in Fig. 45. It can be seen that the contact line shape of droplet on hydrophilic surfaces is no longer circular after the droplet starts to move.

This is contrary to contact line shapes of sessile droplet on superhydrophobic surface which maintains its circular shape at critical state, as shown in Figure 46.

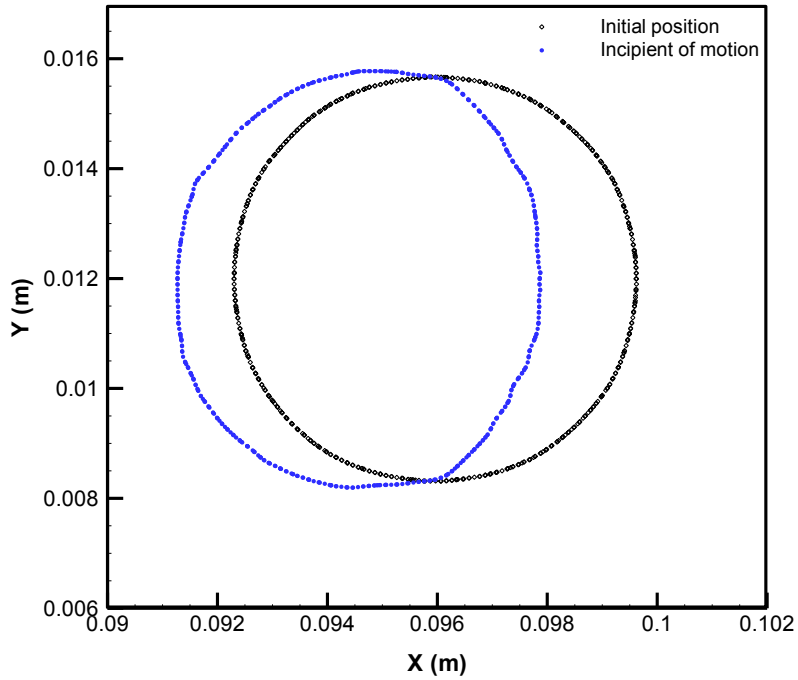

Figure 45: Contact line of sessile droplet on PMMA surface before and after droplet movement.

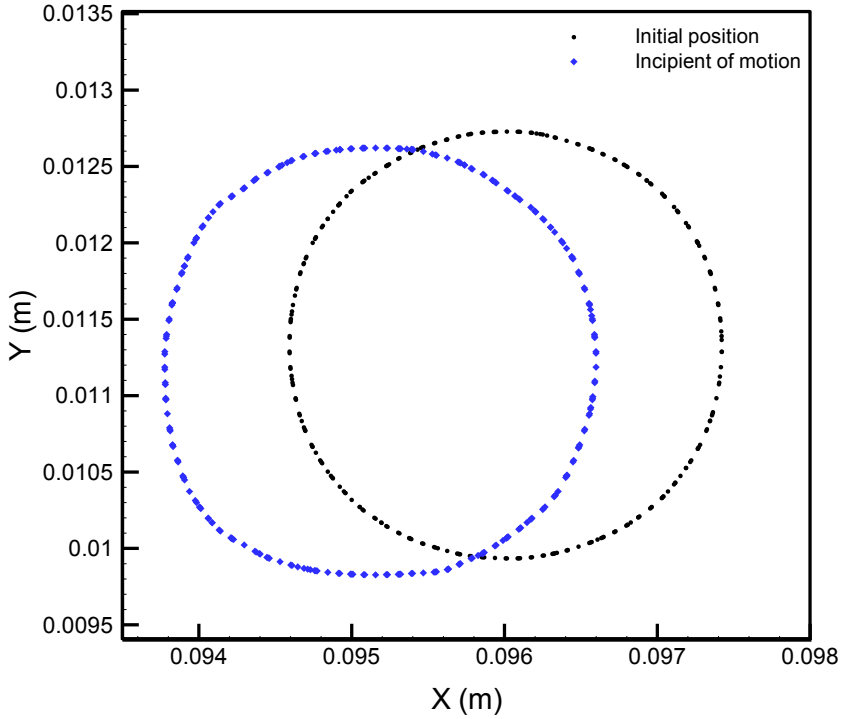

Figure 46: Contact line of a sessile droplet on superhydrophobic surface before and after droplet movement.

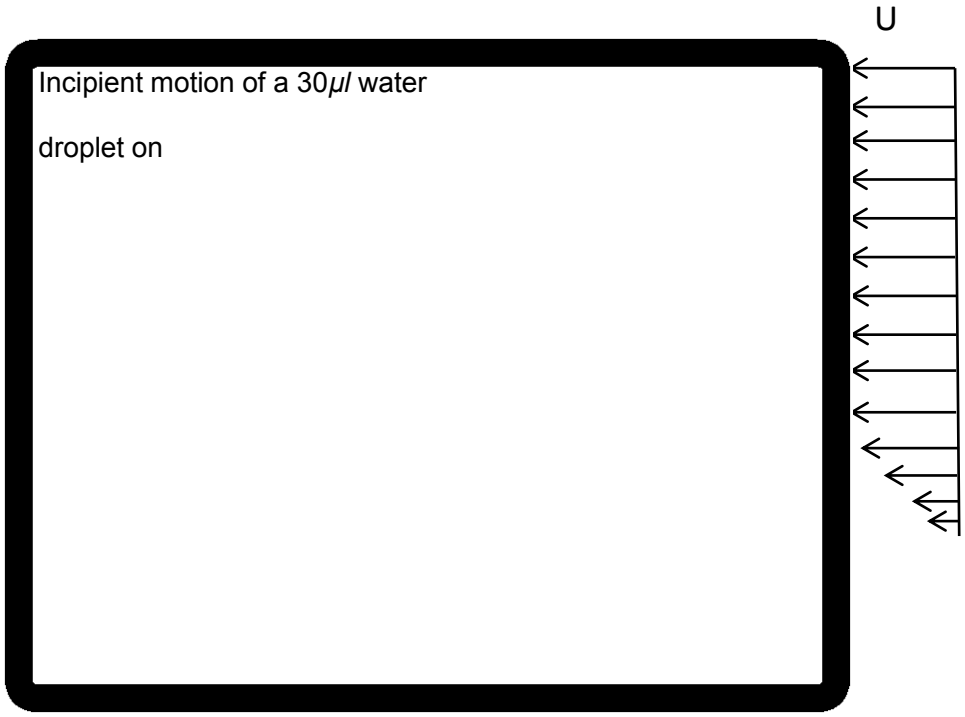

Figure 47: Velocity distribution of airflow around the water droplet on superhydrophobic surface.

Figure 47 shows the velocity distribution of airflow around the water droplet at critical point. It can be seen from this figure that when the sessile droplet is exposed to airflow, the boundary layer separates from the droplet surface forms a free shear layer and is highly unstable. This shear layer will eventually roll into a discrete vortex and detaches from the surface (a phenomenon called vortex shedding), as shown in Figure 48. The vortices which form on the air side around a sessile droplet have a very complicated structure, and have not been elucidated as yet.

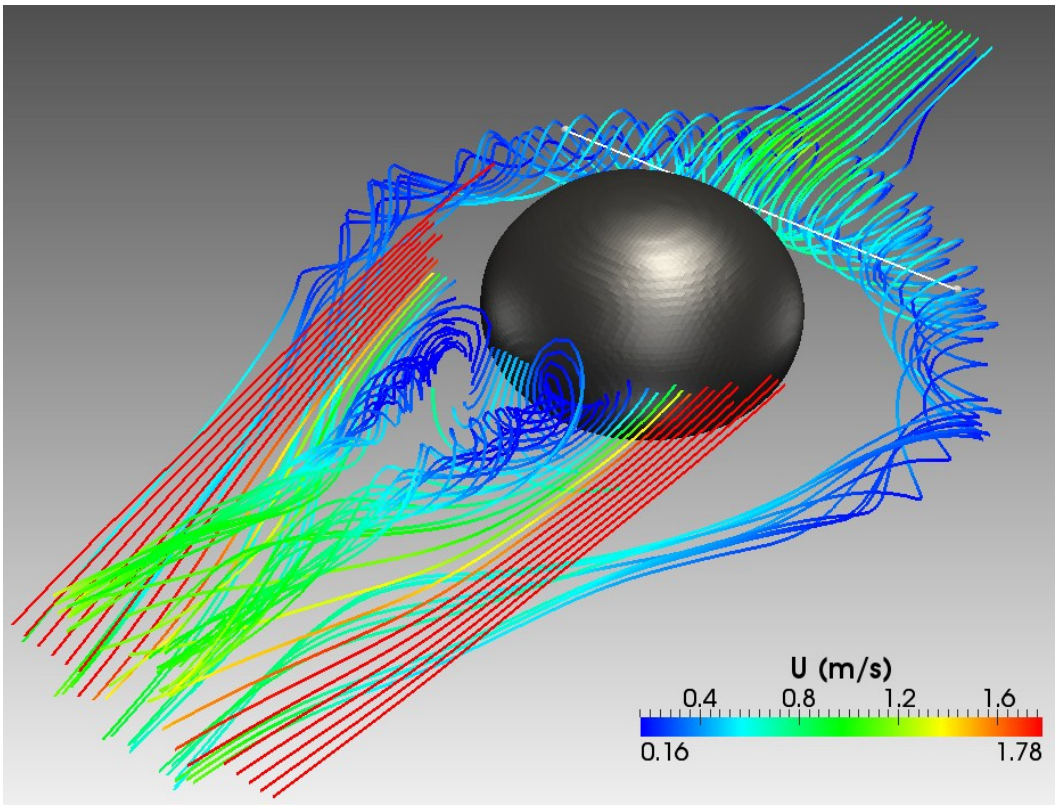

Figure 48. Velocity streamlines around the water droplet on a superhydrophobic surface.

When vortices shed from the sessile droplet, uneven pressure distribution develops between the upstream and downstream surfaces of the droplet, generating an oscillatory aerodynamic loading (drag) on the droplet. This unsteady force can induce significant vibrations on the free surface of droplet, especially if the "resonance" condition is met.

Since the shape of sessile droplet on SHS, Teflon and PMMA surface is similar to blunt body, an integration of the normal pressure distribution in the flow direction on Iso-surface of the droplet can provide information of the aerodynamic forces (drag) acting on the sessile droplet.

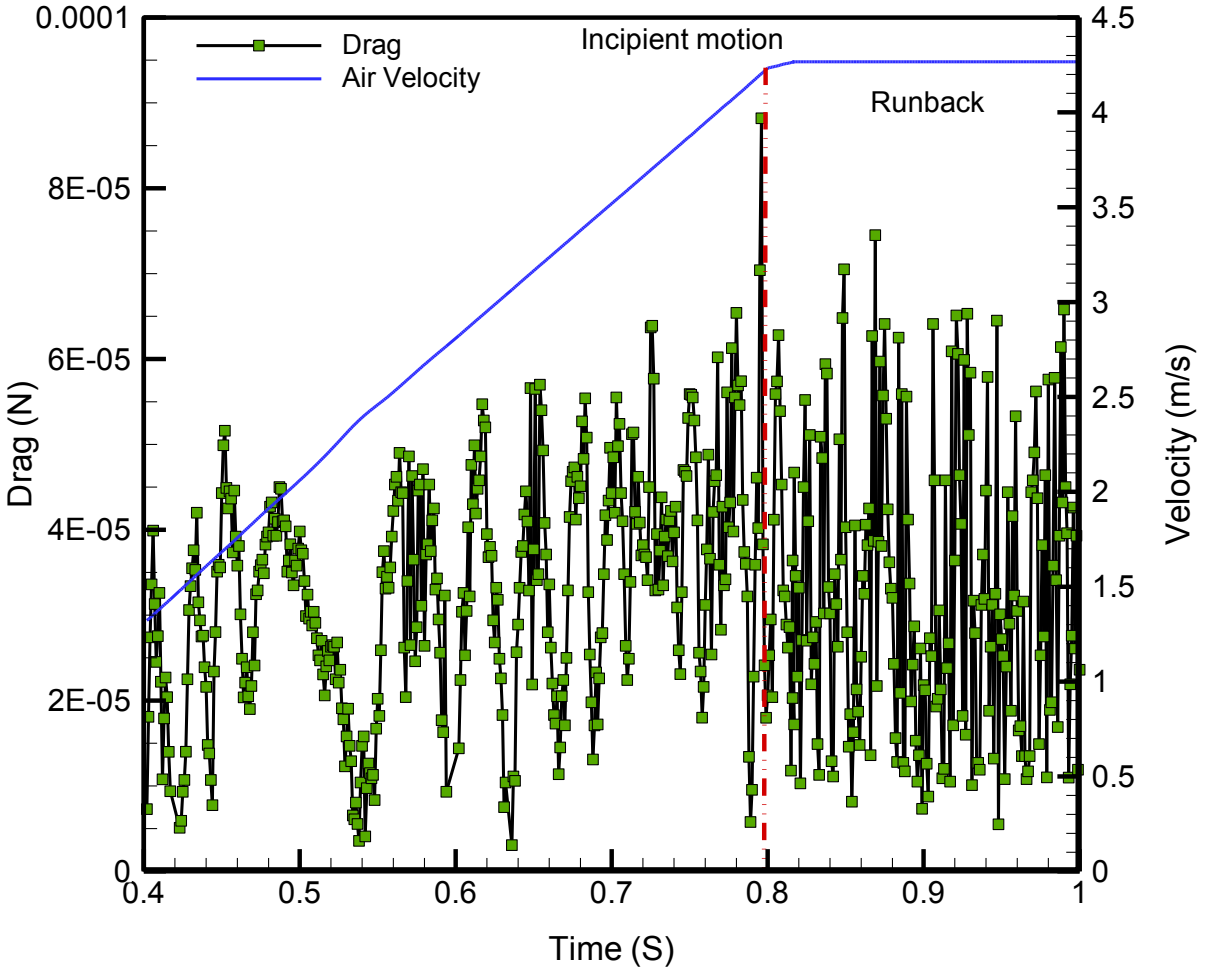

Figure 49: Oscillating drag force on 30 μL water droplet on superhydrophobic surface(θ_s=154º).

Figure 49 presents the temporal evolution of external drag force on a 30 μL water droplet resting on superhydrophobic surface before and after the incipient motion. As it is mentioned before, the air velocity is increased until the point that droplet starts to move. This point is referred to as the point of incipient motion, and after this, the drop is assumed to undergo runback with constant velocity. At the point of incipient motion, the droplet adhesion force to the surface is overcome by the external drag force acting on the droplet. This figure shows the oscillating behavior of drag force on the droplet which mainly stems from the existence of the vortex shedding behind the droplet.

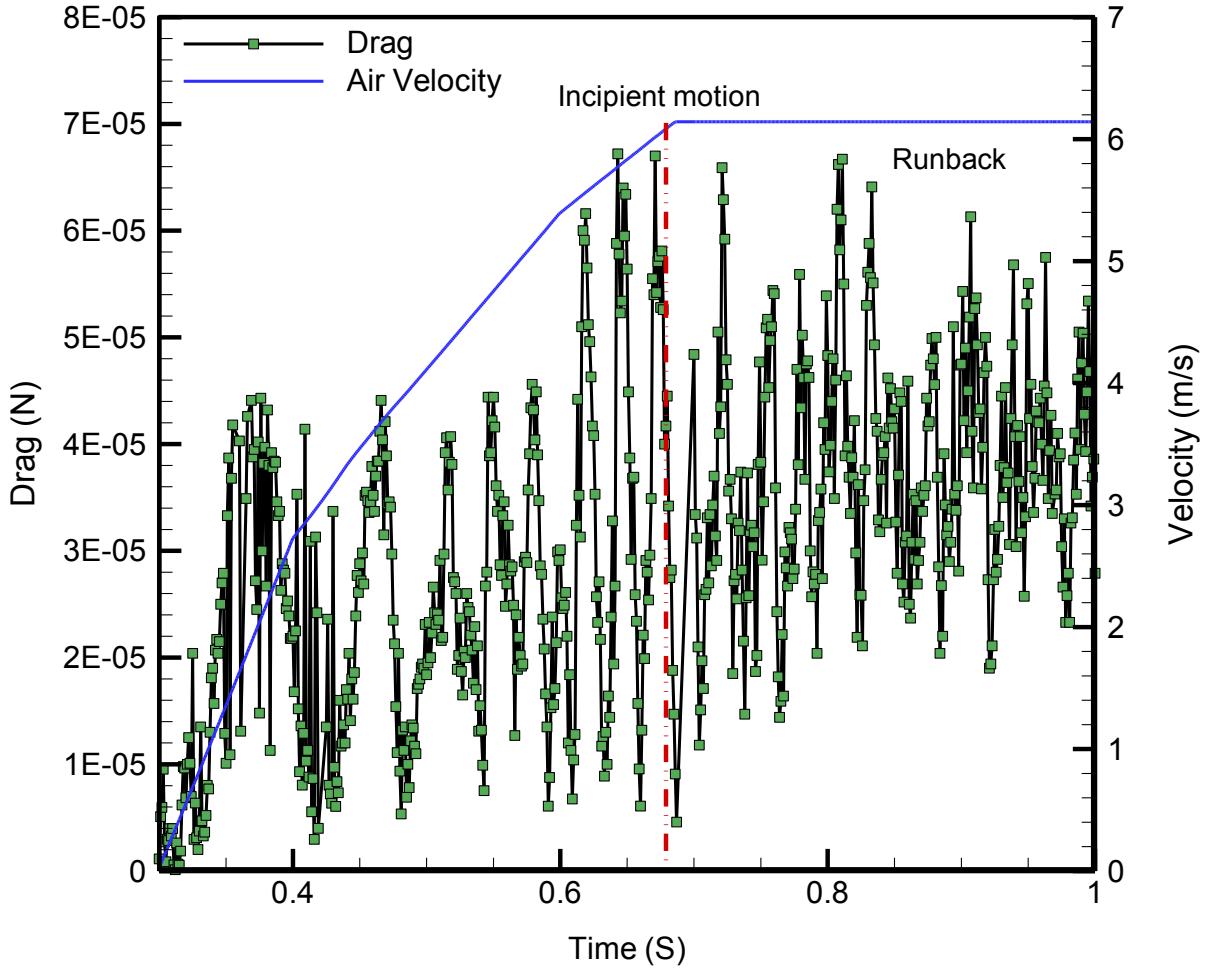

Figure 50: Oscillating drag force on a 30 μL Water droplet on a Teflon surface(θ_s=120º).

Figure 50 shows the time evolution of the drag force on a 30 μL water droplet resting on a Teflon surface while it is exposed to the air velocity. The air velocity is increased until the droplet at around 0.7s starts to move. After that the air velocity is kept constant during the droplet runback.

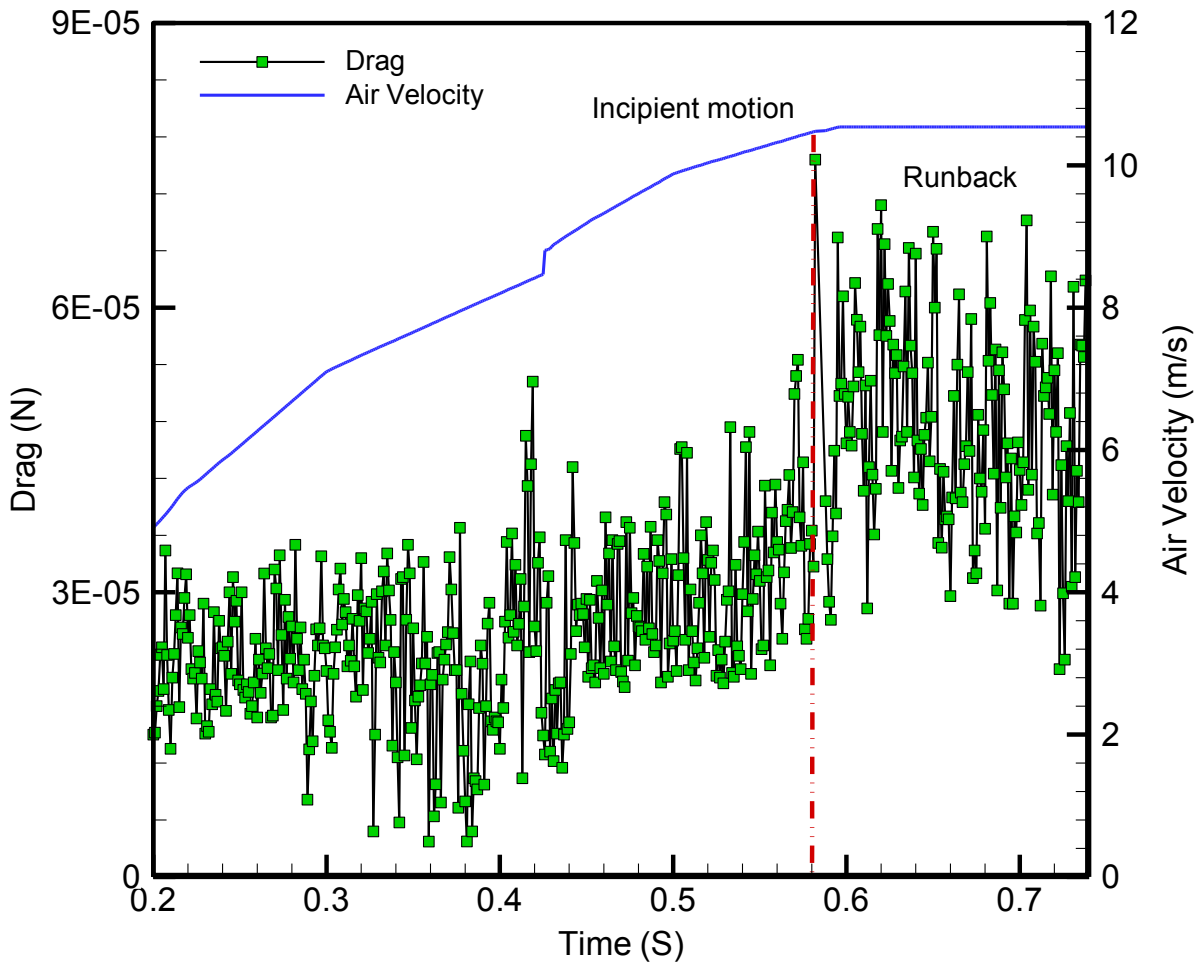

Figure 51: Oscillating drag force on a 30 μL water droplet on a PMMA surface(θ_s=66º).

The effect of vortex shedding due to the shear flow, around the 30 μL water droplet rested on a PMMA surface is shown in Fig. 51. This figure shows less oscillations comparing to the case of droplet on Teflon and superhydrophobic substrates due to the more aerodynamic shapes of droplet on hydrophilic surfaces.

4 Closure

4.1 Conclusions

In this thesis, the dynamic behavior of droplets including the coalescence of a falling droplet with a sessile droplet on solid, and shedding of a sessile droplet exposed to shearing airflow are studied numerically. To validate the numerical model, the results of simulations for maximum spreading diameter of coalescing droplets are compared with experiment. The evolution of surface shape during the coalescence of two droplets on surfaces with various wettabilities are numerically computed and compared with experimental results[51].

- Numerical simulations were carried out varying the separation between the sessile and the impacting droplet from the axisymmetric drop-on-drop case up to the point where the impinging droplet fully impacts a dry surface and coalesces while spreading. It was shown that after the second droplet impacts and merges with the first droplet, the inertia of the second droplet causes the merged drop to deform and spread. After reaching the maximum spreading, surface force causes the droplet to recoil. At this point, the droplet height starts to rise slightly and fall under the influence of gravity. This process continues until the drop comes to its equilibrium state. On surfaces with low wettability, developed inertia during the recoiling process lifts the merged drop from the surface. It was found that for larger distances between the center of sessile and impacting droplet, the merged droplet rotates in the air after bouncing off from the surface.
- The effect of different parameters such as impact velocity, center to center distance, droplet size and surface wettability on maximum spreading length are also studied and compared to the experimental results. It was found that by increasing the hydrophobicity,

and offset ratio the maximum spreading length decreases, while the droplet inertia has a reverse effect on the maximum spreading. It is conceivable that the mobility of the droplet also presented some effect; therefore it would be presumptuous to claim that wettability is the only cause of variance in spreading. Deeply studying the effect of both repellency and mobility on the coalescence process would require an additional study. In the current study four of the five surfaces have a comparable degree of hysteresis; therefore, it is unlikely that this variance in mobility may have obscured the trend of increasing hydrophobicity.

- Based on the evolution of the free surface and the spread diameter of the merging droplets, the use of dynamic contact angle and bounded compression in the numerical works were validated. Since the numerical simulations proved accurate, they were used to obtain internal flow velocity which helped to understand the coalescence dynamics in detail.
- The effect of droplet size and impact velocity on contact time was also investigated and compared well with experimental results. It has been found that the contact time (t_c) is independent of the impact velocity in a wide range of velocities; however, it largely depends on droplet diameter. It was determined that contact time is well-described by the power law $t_c \sim D_0^{1.68}$.
- In addition, the effect of droplet size, impact velocity and overlap ratio on restitution coefficient were investigated. It was found that increasing the impact velocity, droplet size and overlap ratio reduces restitution coefficient due to either the increased deformation of the merged droplets or increased rationality.

- Finally, a correlation is proposed for predicting the maximum spreading length of the merged droplet on various surfaces (from hydrophilic to superhydrophobic) for different impact conditions using both experimental and numerical results.

In the second part of this study, shedding of a sessile droplet exposed to shearing airflow was studied numerically. The numerical results are validated by experiment in terms of critical air velocity.

- The effect of droplet sizes and surface wettability on runback flow was investigated and compared well with experimental results. It was found that wetting parameters such as contact angle and contact angle hysteresis are very influential in determining the minimum required air velocity for drop shedding. Specifically, they affect drop adhesion and drag.
- Adhesion is seen to be an especially strong influencing parameter of shedding, with the lowest adhesion (highest mobility) SHS showing the lowest critical air velocities for shedding of the systems tested.
- Finally, the effect of shedding of vortices from droplet on drag force was investigated. It was determined that when vortices shed from the sessile droplet, uneven pressure distribution develops between the upstream and downstream surfaces of the droplet, generating an oscillatory aerodynamic loading (drag) on the cylinder. This unsteady force can induce significant vibrations on free surface of droplet.

4.2 Recommendations for future work

- In the current model, the effects of heat transfer between surface and droplet on surface mobility are neglected. Therefore, the temperature dependent dynamic contact angle needs to be added to the solver to predict the behavior of coalescing droplet and droplet shedding on cold and hot surfaces.

- The present work focused on water droplet coalescence on surfaces with various wettabilities. Numerical simulation can be extended for liquids with various viscosities to determine the effect of viscosity on maximum droplet spreading.

- The drag coefficient for different droplet sizes on surfaces with various wettabilities can be calculated based on average drag force exerted on droplets after the incipient point. Based on numerical results, a correlation can be proposed to predict the drag coefficient for range of droplet sizes and surface wettability. Such a correlation can be a useful tool for aerospace industry.

- In this study, shedding of a sessile droplet exposed to shearing airflow was studied for range of 2 to 5.5mm droplet sizes. Since the drizzle (drops of 50-500 μm) in clouds are much smaller than freezing rain (drops of 1 mm or larger), numerical simulation can be extended for smaller droplet sizes and wide range of surface wettability to determine behavior of the micron size droplets on surface while exposed to shear flow.

5 Bibliography

(1)A. B. D. Cassie and S. Baxter. "Wettability of porous surfaces," Trans. Faraday Soc **40,** 546-551 (1944).

(2)T. N. Wenzel. J. Phys. Colloid Chem. **53,** 1455 (1949).

(3)B. Bhushan, K. Koch and Y. C. Jung. "Biomimetic Hierarchical Structure for Self-Cleaning," Appl. Phys. Lett. **98,** 093101 (2008).

(4)R. Rioboo, C. Tropea and M. Mareng. "Outcomes from a drop impact on solid surfaces," Atomization Sprays **11,** 155-165 (2001).

(5)Ali Dolatabadi et al. "Ice-phobic evaluation of super-hydrophobic coatings for aircaft icing protection," Montreal : PWC. (2010).

(6)Anonymous "OpenCFD Ltd: OpenFOAM, The Open Source CFD Toolbox, Programmer'sGuide, 2008.".

(7)A. J. B. Milne and A. Amirfazli. "Drop Shedding by Shear Flow for Hydrophilic to Superhydrophobic Surfaces," Langmuir **25,** 14155-14164 (2009).

(8)T. Snyder and S. Korol,. "Modeling the offset solid-ink printing process," IS&T's Recent Progress in Ink Jet Technologies II 175–181 (1999).

(9)D. Soltman and V. Subramanian. "Inkjet-printed line morphologies and temperature control of the coffee ring effect," Langmuir **24,** 2224-2231 (2008).

(10)R. E. Saunders, J. E. Gough, and B. Derby. "Delivery of human fibroblast cells by piezoelectric drop-on-demand inkjet printing." Biomaterials **29,** 193-203 (2008).

(11)M. Kaneda, K. Hyakuta,Y. Takao, H. Ishizuka, and J. Fukai. "Internal Flow in Polymer Solution Droplets Deposited on a Lyophobic Surface during a Receding Process," Langmuir **24,** 9102–9109 (2008).

(12)Y. M. Zhang, Y. Chen, P. Li and A. T. Male. "Weld deposition-based rapid prototyping: a preliminary study," J. Mater. Process Technol. **135,** 347-357 (2003).

(13)M. Fang, S. Chandra and C. B. Park. "Experiments on remelting and solidification of molten metal droplets deposited in vertical columns," J Manuf Sci Eng-Trans ASME **129,** 311-318 (2007).

(14)H. Sirringhaus, T. Kawase, R. H. Friend, et al. "High-resolution inkjet printing of all-polymer transistor circuits," Science **290,** 2123-2126 (2000).

(15)P. C. Duineveld. "The stability of ink-jet printed lines of liquid with zero receding contact angle on a homogeneous substrate," J. Fluid Mech. **477,** 175-200 (2003).

(16)Y. J. Jiang, A. Umemura and C. K. Law. "An experimental investigation on the collision behaviour of hydrocarbon droplets," J. Fluid Mech. 171 (1991).

(17)Young. s.l. "An Essay on the Cohesion of Fluids," Transaction of the Royal Society of London (1805).

(18)K. Smyth, A. Paxon, Hyuk-min Kwon, Tao Deng and K. K. Varanasi. "Dynamic wetting on superhydrophobic surfaces: Droplet impact and wetting hysteresis," Thermal and Thermomechanical Phenomena in Electronic Systems (ITherm), 2010 12th IEEE Intersociety Conference on 1-8 (2010).

(19)Amirfazli, A., Milne and Elliot. "Model and experimental studies for contact angles of surfactant solutions on rough and smooth hydrophobic surfaces," Physical Chemistry (2011).

(20)ierce, E, carmona, F J and Amirfazli, A. s.l. "Understaing of sliding and contact angle results in tilted plate experiments." P : Colloids (2008).

(21)N. A. Patankar. "On the Modeling of Hydrophobic Contact Angles on Rough Surfaces," Langmuir **19,** 1249-1253 (2003).

(22)N. A. Patankar. "Mimicking the Lotus Effect: Influence of Double Roughness Structures and Slender Pillars," Langmuir **20,** 8209-8213 (2004).

(23)E. Puukilainen, T. Rasilainen, M. Suvanto and T. A. Pakkanen. "Superhydrophobic Polyolefin Surfaces: Controlled Micro- and Nanostructures," Langmuir **23,** 7263-7268 (2007).

(24)C. S. Liao, C. F. Wang, H. C. Lin, H. Y. Chou and F. C. Chang. "Fabrication of Patterned Superhydrophobic Polybenzoxazine Hybrid Surfaces," Langmuir **6,** 3359-3362 (2009).

(25)Manish K. Tiwari, Ilker S. Bayer, Gregory M. Jursich, Thomas M. Schutzius and Constantine M. Megaridis. "Highly Liquid-Repellent, Large-Area, Nanostructured

Poly(vinylidene fluoride)/Poly(ethyl 2-cyanoacrylate) Composite Coatings: Particle Filler Effects," ACS Appl. Mater. Interfaces **2,** 1114-1119 (2010).

(26)C. Gu and T. Y. Zhang. "Electrochemical synthesis of silver polyhedrons and dendritic films with superhydrophobic surfaces," Langmuir **24,** 12010-12016 (2008).

(27)S. Herminghaus. "Roughness-induced non-wetting," Europhys. Lett. **52,** 165 (2000).

(28)H. J. Li, X. B. Wang, Y. L. Song, et al. "Super-"amphiphobic" aligned carbon nanotube films," Angewandte Chemie **40,** 1743-1746 (2001).

(29)S. H. Lu, M. H. N. Tun, Z. J. Mei, G. H. Chia, X. Lim and C. H. Sow. "Improved Hydrophobicity of Carbon Nanotube Arrays with Micropatterning," Langmuir **25,** 12806-12811 (2009).

(30)R. Rioboo, C. Bauthier, J. Conti, M. Voue and J. De Coninck. "Experimental investigation of splash and crown formation during single drop impact on wetted surfaces," Exp. Fluids **35,** 648-652 (2003).

(31)S. Chandra and C. T. Avedisian. "On the Collision of a Droplet with a Solid Surface," Proc. R. Soc. Lond. A. **432,** 13-41 (1991).

(32)I. V. Roisman, B. Prunet-Foch, C. Tropea and M. Vignes-Adler. "Multiple Drop Impact on to a Dry Solid Substrate," J. Colloid Interface Sci. **256,** 396-410 (2002).

(33)D. Richard and D. Quere. "Bouncing water drops," Europhys. Lett. **50,** 769-775 (2000).

(34)D. Richard, C. Clanet and D. Quere. "Surface phenomena: Contact time of a bouncing drop," Nature **417,** 811 (2002).

(35)L. Lafuma and D. Quere. "Superhydrophobic states," Nature Mater 457 (2003).

(36)M. Passandideh-Fard, Y. M. Qiao, S. Chandra and J. Mostaghimi. "Capillary effects during droplet impact on a solid surface," Phys. Fluids **8,** 650-659 (1996).

(37)Roisman, Ilia, Rioboo, Romain and Tropea, Cameron. s.l. "Normal impact of a liquid drop on a dry surface: model for spreading and receding," The Royal Society (2002).

(38)Ukiwe, Chijoke and Kwok, Daniel Y. s.l. "On The Maximum Spreading Diameter of Impacting Droplets on Well-Prepared Solid Surfaces," Langmuir (2005).

(39)J. Fukai, Z. Zhao, D. Poulikakos, C. M. Megaridis, and O. Miyatake. "Modeling of the deformation of a liquid droplet impinging upon a flat surface," Phys. Fluids A **5,** 2588 (1993).

(40)J. Fukai, Y. Shiiba, T. Yamamoto, O. Miyatake, D. Poulikakos, C. M. Megaridis, and Z. Zhao. "Wetting effects on the spreading of a liquid droplet colliding with a flat surface: Experiment and modeling " Phys. Fluids **7,** 236 (1995).

(41)T. Bennett and D. Poulikakos. "Splat-quench solidification: Estimating the maximum spreading of a droplet impacting a solid surface," J. Mat. Sci. **28,** 963 (1993).

(42)M. Rein. "Phenomena of liquid drop impact on solid and liquid surfaces," Fluid Dyn. Res. **12,** 61-93 (1993).

(43)A.L. Yarin. "DROP IMPACT DYNAMICS: Splashing, Spreading, Receding, Bouncing…," Annual Review of Fluid Mechanics **38,** 159 -192 (2006).

(44)Mehdi-Nejad, V., Mostaghimi, J., Chandra, S. " Air bubble entrapment under an impacting droplet," Physics of Fluids **15,** 173-183 (2003).

(45)M. Reyssat, A. Pepin, F. Marty and Y. Chen. "Bouncing transition on microtextured materials." Europhys. Lett. **74,** 306-312 (2006).

(46)L. Chen, Z. Xiao, P. C. H. Chan, Y. K. Lee and Z. Li. "A comparative study of droplet impact dynamics on a dual-scaled superhydrophobic surface and lotus leaf," Appl. Surf. Sci. **257,** 8857-8863 (2011).

(47)J. Stringer and B. Derby. "Limits to feature size and resolution in ink jet printing," J. Eur. Ceram. Soc (2009).

(48)R. Li, N. Ashgriz, S. Chandra, J. Andrews and S. Drappel. "Coalescence of two droplets impacting a solid surface," Exp. Fluids **48,** 1025-1035 (2010).

(49)R. Li, N. Ashgriz, S. Chandra, J. Andrews and J. Williams. "Drawback During Deposition of Overlapping Molten Wax Droplets," J. Manuf. Sci. Eng. **130,** 041011.1-041011.10 (2008).

(50)Dhiman, Rajeev and Chandra, Sanjeev. "Freezing-induced splashing during impact of molten metal droplets with high Weber numbers," International Journal of Heat and Mass Transfer **48,** (2005).

(51)M. M. Farhangi, P. J. Graham, N. R. Choudhury and A. Dolatabadi. "Induced Detachment of Coalescing Droplets on Superhydrophobic Surfaces," Langmuir **25,** 1290–1303 (2012).

(52)J. B. Boreyko and C. H. Chen . "Self-Propelled Dropwise Condensate on Superhydrophobic Surfaces," Phys. Rev. Lett. **103,** 184501-184501 (2009).

(53)C. Dietz, K. Rykaczewski, A. G. Fedorov and Y. Joshi. "Visualization of droplet departure on a superhydrophobic surface and implication to heat transfer enhancement during dropwise condensation," Appl. Phys. Lett. **97,** 033104 (2010).

(54)F. Gao and A. A. Sonin. "Precise deposition of molten microdrops: the physics of digital microfabrication," Proc. R. Soc. Lond. Ser. A **44,** 533-554-554 (1994).

(55)M. Sellier and E. Trelluyer,. "Modeling the coalescence of sessile droplets," Biomicrofluidics **3,** 022412 (2009).

(56)N. Kapur and P. H. Gaskell. "Morphology and dynamics of droplet coalescence on a surface," Phys. Rev. E 75 056315.

(57)A. Menchaca-Rocha, A. Martínez-Dávalos, R. Núñez, S. Popinet and S. Zaleski. "Coalescence of liquid drops by surface tension." Phys. Rev. E. **63,** 046309 (2001).

(58)S. T. Thoroddsen, K. Takehara and T. G. Etoh. "The coalescence speed of a pendant and a sessile drop." J.Fluid Mech. **527,** 85-114 (2005).

(59)J. B. Keller, P. Milewski and J. M. Vanden-Broeck. "Merging and wetting driven by surface tension," Euro. J. Mech. B - Fluids **19,** 491-502 (2000).

(60)H. N. Oguz and A. Prosperetti. "Bubble entrainment by the impact of drops on liquid surfaces." J. Fluid Mech. **219,** 143-179 (1990).

(61)W. D. Ristenpart, P. M. McCalla, R. V. Roy and H. A. Stone. "Coalescence of Spreading Droplets on a Wettable Substrate," Phys. Rev. Lett. **97,** 064501 (2006).

(62)C. Andrieu, D. A. Beysens, V. S. Nikolayev and Y. Pomeau. "Coalescence of sessile drops," J. Fluid Mech. **453,** 427-438 (2002).

(63)L. Duchemin, J. Eggers and C. Josserand. "Inviscid coalescence of drops," J. Fluid Mech. **487,** 167-178 (2003).

(64)J. Eggers, J. R. Lister and H. A. Stone. "Coalescence of liquid drops," J. Fluid Mech. **401,** 293-310 (1999).

(65)Z. Wang, C. Lopez, A. Hirsa and N. Koratkar. "Impact dynamics and rebound of water droplets on superhydrophobic carbon nanotube arrays," Appl. Phys. Lett. **91,** 023105 (2007).

(66)A. L. Biance, F. Chevy, C. Clanet, G. Lagubeau and D. Quere. "On the elasticity of an inertial liquid shock," J. Fluid Mech. **554,** 47-66 (2006).

(67)J. Kim and E. K. Longmire. "Investigation of binary drop rebound and coalescence in liquids using dual-field PIV technique," Exp. Fluids **47,** 263-278 (2009).

(68)C. Ortiz-Duenas, J. Kim and E. K. Longmire. "Investigation of liquid–liquid drop coalescence using tomographic PIV," Exp. Fluids **49,** 111-129 (2010).

(69)M. A. Nilsson and J. P. Rothstein. "The effect of contact angle hysteresis on droplet coalescence and mixing," J Colloid Interface Sci. 646-54 (2011).

(70)E. B. White and Schmucker. "A Runback Criterion for Water Drops in a Turbulent Accelerated Boundary Layer," J. A. J. Fluids Eng. **130,** 061302–1 (2009).

(71)Thoreau, V., Malki, B., Berthome, G., Boulange-Petermann, L. & Joud, J. C. "Physico-chemical and dynamic study of oil-drop removal from bare and coated stainless steelsurfaces," J. Adhesion Sci. Technol **20,** 1819–1831 (2006).

(72)Lee S, Bragg M, B. "Experimental investigation of simulated large-droplet ice shapes on airfoil aerodynamics," Journal of Aircraft **36,** (199).

(73)J. Bico and Basseli. " Windswept Droplets (oral presentation)." APS-Division of Fluids Dynamics Meeting **22,** (2005).

(74)Mahe´, M., Vignes-Adler, M., Rousseau, A., Jacquin, C. G., and Adler, P. M.,. "Adhesion of Droplets on a Solid Wall and Detachment by a Shear Flow," J. Colloid Interface Sci. **126,** 314-328 (1988).

(75)Ostrovsky, M. V., and Nestaas, E. "Theory of oil detachment from a solid surface," J. Colloids Surf. **26,** 351-372 (1987).

(76)Dussan, E. B. and Chow, R. T. "On the ability of drops or bubbles to stick to non-horizontal surfaces of solids," J. Fluid Mech. **137,** 1-29 (1984).

(77)Xiaofan Li, and C. Pozrikidis. "Shear flow over a liquid drop adhering to a solid surface," Journal of Fluid Mechanics **307,** 167-197 (1996).

(78)Basu, S., Nandkumar, K., Masliyah, J.H.,. "A model for detachment of a partially wetting drop from solid surface by shear flow," Journal of Colloid and Interface Science **190,** 253-257 (1997).

(79)Dimitrakopoulos, P., Higdon, J.J.L.,. " Displacement of fluid droplets from solid surfaces in low-Reynolds-number shear flows," Journal of Fluid Mechanics **336,** 351-378 (1997).

(80)G. Minor. "Experimental Study of Water Droplet Flows in a Model PEM Fuel Cell Gas Microchannel," M.A.Sc. Thesis, University of Victoria, (2007).

(81)A. Z. Weber and J. Newman. "Transport in Polymer-Electrolyte Membranes. III. Model Validation in a Simple Fuel-Cell Model," J. Electrochem. Soc. **151,** 326 (2004).

(82)Zhu, X., P. C. Sui, and N. Djilali,"Dynamic behaviour of liquid water emerging from a GDL pore into a PEMFC gas flow channel," J. Power Sources **172,** 287-295 (2007).

(83)F. Y. Zhang, X. G. Yang and C. Y. Wang. "Liquid Water Removal from a Polymer Electrolyte Fuel Cell," J. Electrochem. Soc **153,** 225-232 (2006).

(84)K. S. Chen, M. A. Hickner and D. R. Noble. "Simplified models for predicting the onset of liquid water droplet instability at the gas diffusion layer/gas flow channel interface ," Int. J. Energy. Res. **29,** 1113-1132 (2005).

(85)E. C. Kumbur, K. V. Sharp and M. M. Mench. "Liquid droplet behavior and instability in a polymer electrolyte fuel cell flow channel," J. Power Sources **161,** 333-345 (2006).

(86)Ding, H.,Spelt,P.D.M.,. "Onset of motion of a three-dimensional droplet on a wall in shear flow at moderate Reynolds numbers," J.Fluid Mech. **599,** 341-362 (2008).

(87)Ding, H.,Gilani,M.N.H.,Spelt,P.D.M. "Sliding, pinch-off and detachment of a droplet on a wall in shear flow," J.Fluid Mech. **644,** 217-244 (2010).

(88)P. Graham. "Droplet Coalescence on Surfaces of Various Wettabilities," Master Thesis, Dept. Mechanical Eng. Concordia Univesity, Montreal, Canada (2012).

(89)Rider, W.J., Kothe, D.B. "Reconstructing volume tracking," Journal of Computational Physics **141,** 112-152 (1998).

(90)Afkhami, S., Bussmann, M. "Height functions for applying contact angles to 2D VOF simulations," International Journal for Numerical Methods in Fluids **57,** 453–472 (2008).

(91)F. H. Welch Harlow J.E. "Numerical calculation of time-dependent viscous incompressible flow of fluid with free surface," Physics of Fluids **8,** 2182–2189 (1965).

(92)M. Bussmann, J. Mostaghimi and S. Chandra. "On a three-dimensional volume tracking model of droplet impact." Phys. Fluids **11,** 1406-1417 (1999).

(93)Hirt, C.W., Nichols, B.D. "Volume of fluid (VOF) method for the dynamics of free boundaries," Journal of Computational Physics **39,** 201–225 (1981).

(94) "OpenCFD Ltd., http://www.opencfd.co.uk/.

(95)H. Rusche. "Computational fluid dynamics of dispersed two-phase flows at high phase fractions." Dpt. of Mech. Eng., Imperial College, London (2002.).

(96)R. I. Issa, B. Ahmadi-Befrui, K. R. Beshay and A. D. Gosman. "Solution of the implicitly discretised reacting flow equations by operator-splitting," J. Comput. Phys. **93,** 388-410 (1991).

(97)H. Jasak. "Error analysis and estimation for the finite volume method with applications to fluid flows," PhD Thesis, Imperial College of Science, Technology and Medicine, London, (1996).

(98)M. Bracke, F. De Voeght and P. Joos. "The Kinetics of wetting: the dynamic contact angle." Prog. Colloid Polym. Sci. **79,** 142–149 (1989).

(99)R. G. Cox. "The dynamics of the spreading of liquids on a solid surface. Part 2. Surfactants," J.Fluid Mech. **168,** 169-194 (1986).

(100)T. S Jiang, O. H. Soo-Gun and J. C. Slattery. "Correlation for dynamic contact angle," J.Colloid Interface Sci. **69,** 74-77 (1979).

(101)S. F. Kistler . "Hydrodynamics of wetting," 311-429 (1993).

(102)A. Theodorakakos and G. Bergeles. "Simulation of sharp gas-liquid interface using VOF method and adaptive grid local refinement around the interface. ," Int. J. Numer. Meth. Fluids **45,** 421-439 (2004).

(103) www.Ansys.com

(104)P. Graham and Farhangi, M., Dolatabadi, A. "Dynamics Of Droplet Coalescence In Response To Increasing Hydrophobicity," Phys. Fluids (2012).

(105)S. Gekle and J. M. Gordillo. "Generation and breakup of Worthington jets after cavity collapse. Part 1. Jet formation," J. Fluid Mech. **663,** 293-330 (2010).

(106)E. Chibowski. "Surface free energy of a solid from contact angle hysteresis ," Adv. Colloid Interface Sci. **103,** 149-172 (2003).